ACTIVE BLIND-THRUST FAULTING AND STRIKE-SLIP FAULT-BEND FOLDING IN CALIFORNIA

by
JOHN H. SHAW

A DISSERTATION
PRESENTED TO THE FACULTY
OF PRINCETON UNIVERSITY
IN CANDIDACY FOR THE DEGREE
OF DOCTOR OF PHILOSOPHY

RECOMMENDED FOR ACCEPTANCE BY THE
DEPARTMENT OF GEOLOGICAL AND GEOPHYSICAL SCIENCES

OCTOBER 1993

PREFACE

This dissertation describes active geologic structures in California and presents new methods of earthquake hazards assessment and structural analysis for petroleum exploration. Chapter 1 is a general introduction to active blind-thrust faulting in coastal southern California and to our methods of earthquake hazards assessment. The paper is co-authored by Prof. John Suppe (Princeton University) and is to be published in modified form in the 1993 Phase II Report of the Southern California Earthquake Center. Chapters 2 and 3 contain more detailed structural analyses that identify active blind-thrust faults in the Santa Barbara Channel and Los Angeles basin, determine long-term fault slip rates, and estimate potential earthquake magnitudes and recurrence intervals. Both papers are co-authored by Prof. Suppe, who developed much of the fundamental theory of folding and faulting applied in these works. Chapter 2 has been submitted to the Geological Society of America Bulletin. Chapter 4 presents a new method of structural trend analysis by axial surface mapping and is co-authored by Stephen C. Hook (Texaco) and John Suppe. Dr. Hook initially developed the Tunic example from Pennsylvania and was instrumental in attaining seismic reflection data from other areas. Chapter 5 describes folding and faulting along the San Andreas fault in the epicentral zone of the 1989 (M_S = 7.1) Loma Prieta earthquake. The paper is co-authored by Richard E. Bischke and John Suppe, who both provided insight into the three-dimensional structural modeling and regional geology. Dr. Bischke also developed and applied a new method of analyzing well log data to investigate recent activity along the Zayante fault, which lies adjacent to the San Andreas fault in the epicentral region.

CHAPTER 4

STRUCTURAL TREND ANALYSIS BY AXIAL SURFACE MAPPING

JOHN H. SHAW & JOHN SUPPE
Department of Geological and Geophysical Sciences, Guyot Hall, Princeton University, Princeton, New Jersey USA 08544-1003

STEPHEN C. HOOK
Texaco EPTD, 3901 Briarpark, Houston, Texas, USA 77042

submitted for publication to the
American Association of Petroleum Geologists Bulletin

ABSTRACT

We present a new method of structural trend analysis in which axial surfaces (fold hinges) are mapped through grids of seismic reflection profiles and balanced forward models. Axial surface maps: 1) define fold trends, lateral terminations, and closure in structure; 2) constrain underlying fault geometry and slip; and 3) highlight and connect regions that can be interpreted by a series of balanced models or cross sections. Maps of folds in southern California and northeastern Pennsylvania are compared with forward model solutions and used to construct balanced three-dimensional structural interpretations using fault-bend fold theory. Axial surface maps generated from balanced fault-bend fold models define theoretical relationships between map patterns and structural geometry and fault slip. Kink-band widths between paired axial surfaces in map view are related to underlying fault slip. Lateral variations in fault slip, which can be identified on axial surface maps, cause fold plunge and provide lateral closure. Lateral changes in subsurface fault geometry, which include lateral and oblique ramps, are also reflected by terminations, bends, or offsets of axial surface in map-view. Based on these relationships between folding and faulting, we develop map-view interpretations and balanced cross sections across structures that are consistent with the geology along trend.

INTRODUCTION

The construction of area-balanced geologic cross sections is a proven method for developing reasonable structural interpretations of folded and faulted terrains (Dahlstrom, 1969; Woodward et al., 1985). A cross section typically provides information only along the chosen plane of section. In many cases, however, three-dimensional analysis is vital to constrain subsurface structural geometry and fault slip. Lateral changes in fold and fault trends often play important roles in forming structural traps for hydrocarbons and in assessing the hazards posed by active

seismogenic faults. Here we present the straightforward technique of *Axial Surface Mapping* for analyzing three-dimensional structural geometry in map view. This technique: 1) defines fold trends and lateral changes in structure; 2) constrains underlying fault geometry and slip; and 3) highlights and connects regions that can be interpreted by a series of balanced models or geologic cross sections. In the same way that area-balanced cross sections yield reasonable interpretations along a single plane, map view analysis leads to interpretations that are consistent with the geology along trend.

We describe the axial surface mapping technique using balanced two-dimensional forward models that are combined to approximate the three-dimensional geometry of many map scale folds (termed the "pseudo-three-dimensional approach" by Wilkerson et al., 1991). These models highlight specific relationships between axial surface map patterns and structural geometry and fault slip. The axial surface map patterns derived from forward models are then used to interpret maps constructed through seismic reflection grids from northeastern Pennsylvania and southern California.

In practice we find that axial surface maps should be constructed through data as a first step in developing a complete subsurface interpretation. Mapping axial surfaces helps the interpreter quickly review the available data, yet can require only the identification of axial surfaces as a starting point. This allows the interpreter to examine and map the data while avoiding assumptions that may significantly prejudice the final structural solution. Map patterns derived from data are then compared with those from forward models developed here or by the interpreter using a balanced forward modeling strategy (Mount et al., 1990). A final subsurface interpretation is derived iteratively by developing a series of two- and three-dimensional models that approach the observed map pattern.

AXIAL SURFACE MAPPING

Map scale folds often form in the upper crust by movement of rock over bends in underlying faults (Rich, 1934; Suppe, 1983). Purely rigid-block translation over non-planar faults would generate unreasonable overlaps or voids between fault blocks that cannot be supported at depth. Fault-bend folding of the hangingwall, however, accommodates fault slip without producing overlaps or voids (Figure 1). Fault-bend folds are commonly imaged in seismic reflection profiles as kink-bands bounded by parallel synclinal and anticlinal axial surfaces (Figure 2).

Fault-bend folds (Suppe, 1983) grow by kink-band migration with deformation of the over-riding block localized along *active axial surfaces* that are pinned to the footwall at fault bends (Figure 3). *Inactive axial surfaces* also form at fault bends at the initiation of faulting but are rigidly translated away from the active axial surfaces during progressive fault slip. Kink-band widths between sets of active and inactive axial surfaces are directly related to fault dip-slip. Therefore, axial surface maps constructed through grids of seismic reflection profiles or cross sections provide direct information on fold geometry and fault slip.

Axial surfaces can be mapped by projection from sections to a horizontal datum. We present two different projection methods: the *Parallel Projection Method* (*PPM*) and the *Vertical Projection Method* (*VPM*) (Figure 4). The parallel projection method is a strictly geometric method that can record fold limb widths and fault slip; whereas, the vertical projection method is a geometric and geologic method that records the spatial position of the fold at a mapped horizon.

In *PPM* axial surfaces are projected along their traces in section to the datum (Figure 4A). These projections are easily made and can provide direct information on fold limb widths and fault slip. In simple fault-bend folds (those in which ramps connect decollements), overlying limb (kink-band) width on the horizontal datum (Lm) is equal to both limb length (Lc) and fault slip in cross section (Figure 5). In

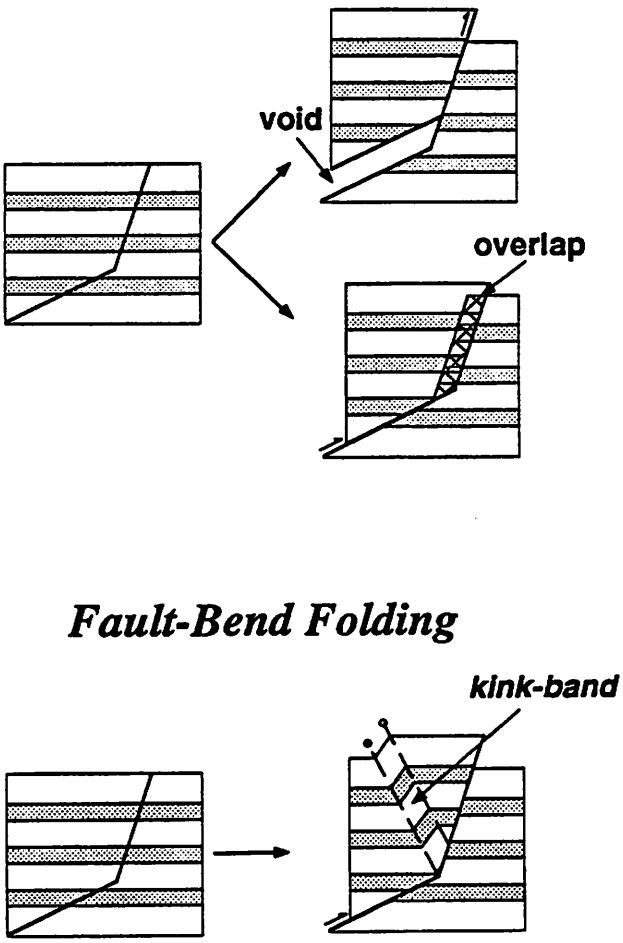

Figure 1: Purely rigid-block translation over a non-planar fault generates an unreasonable overlap or void between fault blocks. However, folding of the hangingwall block localized along axial surfaces related to fault bends accommodates fault slip without generating an overlap or void.

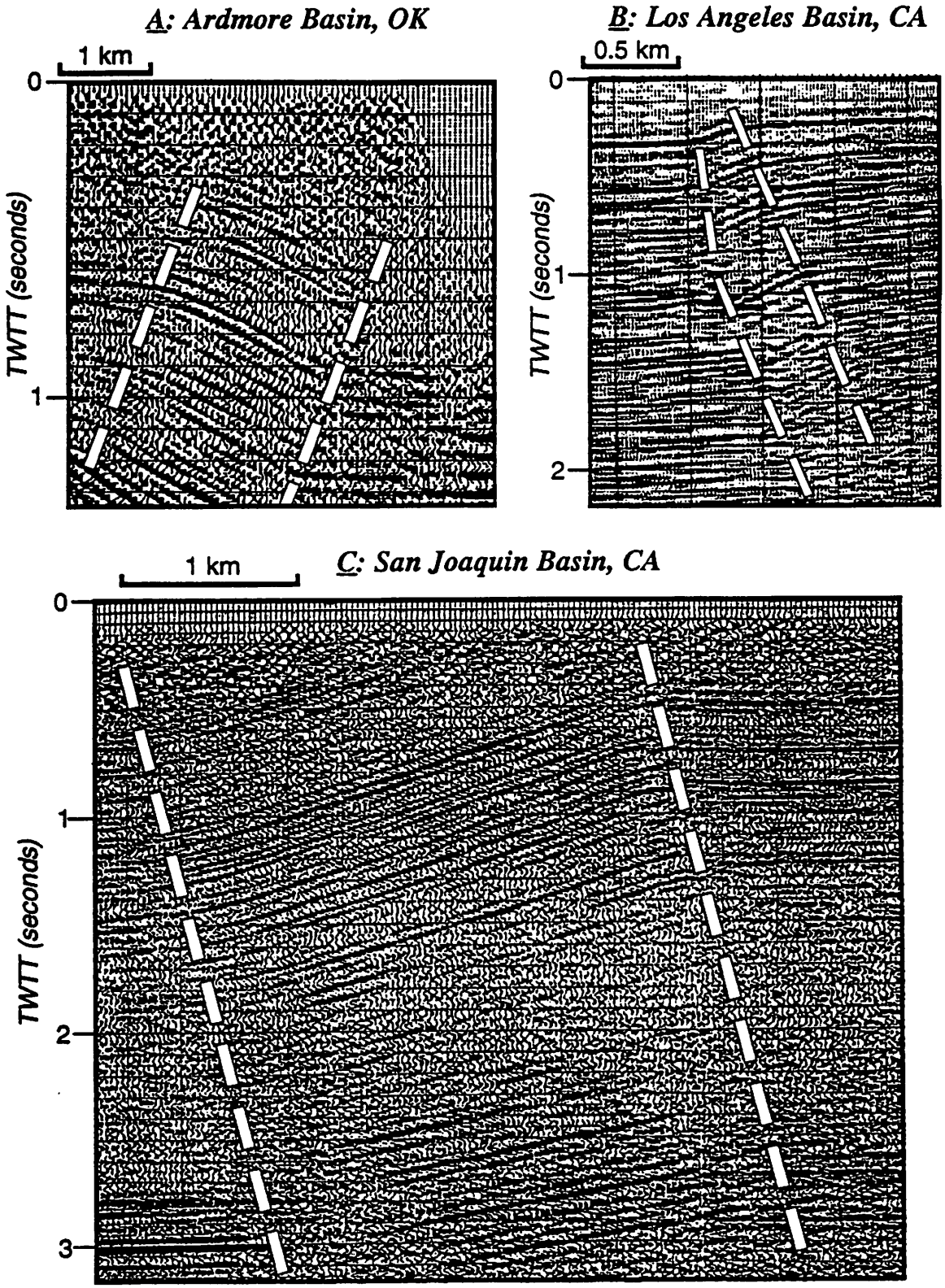

Figure 2: Kink-bands bounded by parallel axial surfaces imaged in seismic reflection profiles from the Ardmore, Los Angeles, and San Joaquin basins. The kink-band in the Los Angeles basin (B) narrows upward into syntectonic section (Suppe et al., 1992). (Seismic profiles provided by Halliburton Geophysical Services, Inc. (A); Texaco USA and Nippon Western Co., Ltd. (B); and Western Geophysical (C).)

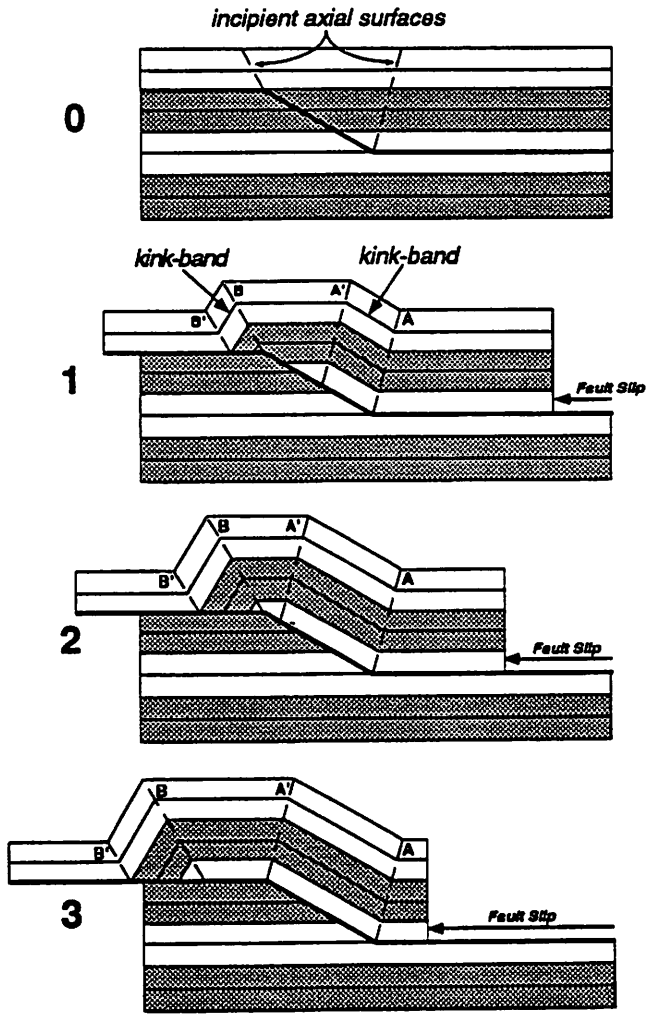

Figure 3: Kinematic development of a fault-bend fold after Suppe (1983). **0**: An incipient thrust fault and axial surfaces in undeformed strata. **1**: Fault slip causes folding of the hangingwall block along active axial surfaces A and B that are pinned to the two fault bends. Inactive axial surfaces A' and B' form at fault bends and are passively translated away from active axial surfaces by slip. Kink-band width A-A' or B-B' measured along bedding equals slip on the underlying fault segment. The difference in kink-band width between back and front limbs reflects slip consumed in folding. **2**: Progressive fault slip widens both kink-bands. Models 1 and 2 are in the *crestal uplift stage* because the fold crest elevates with increasing fault slip. **3**: When the axial surface A' reaches the upper fault bend, material from the back limb is refolded onto the crest and the front limb kink-band B-B' is translated along the upper detachment. In model 3, A and A' are active axial surfaces; B and B' are inactive axial surfaces. Model 3 is in the *crestal broadening stage* because the fold crest widens without producing additional structural relief with increasing fault slip.

Projection of Axial Surfaces for Map Construction

A: Parallel Projection Method (PPM)

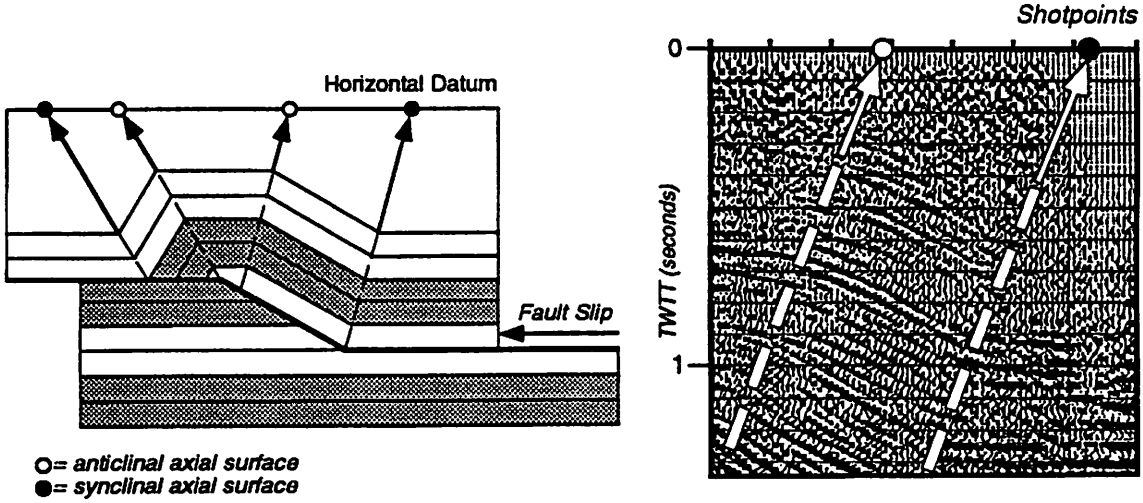

B: Vertical Projection Method (VPM)

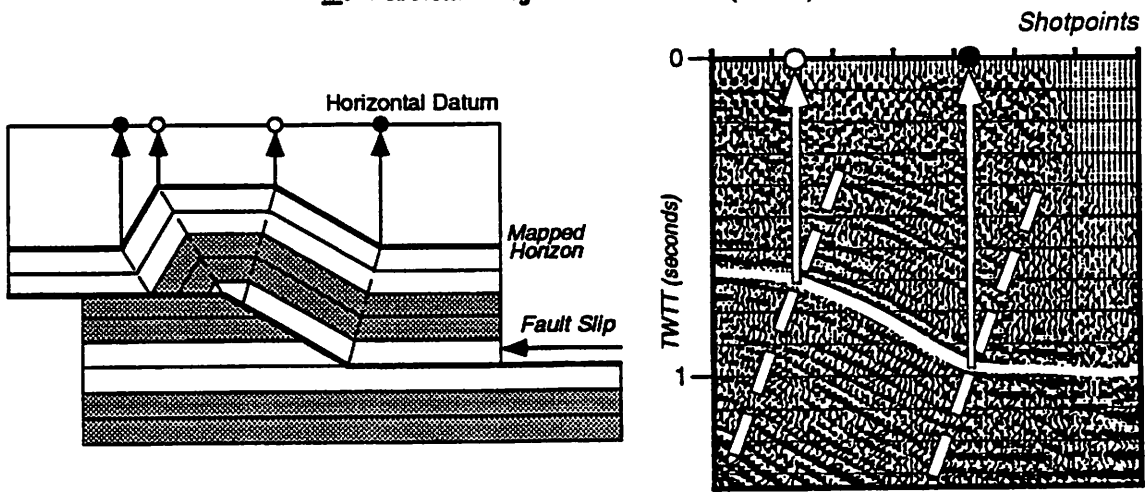

Figure 4: Two methods of axial surface projection are illustrated above fault-bend fold models and kink-bands imaged in seismic reflection profiles. **A:** In the Parallel Projection Method (PPM) axial surfaces are projected along their traces in cross section or profile to the datum. Parallel projection is strictly a geometric method that preserves kink-band widths that are related to fault slip magnitudes, but distorts the horizontal (map-view) position of the fold. **B:** In the Vertical Projection Method (VPM) the intersections between axial surfaces and the mapped horizon are projected vertically to the horizontal datum. Vertical Projection is a geometric and geologic method that records the horizontal position of the fold at the mapped horizon, but distorts kink-band widths. (Seismic profile provided by Halliburton Geophysical Services, Inc.)

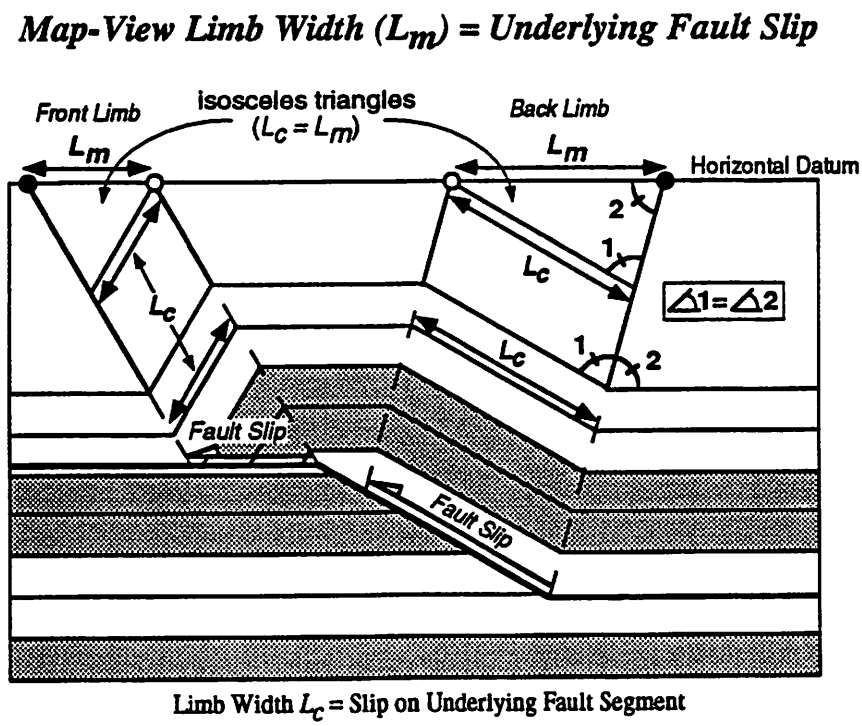

Figure 5: The parallel projection method (Fig. 4A) generates kink-band widths in map view (L_m) that are equal to fold limb widths (L_c) in sections where axial surfaces bisect fold limbs and kink-bands are bounded by horizontal strata. For folds above simple ramps between decollements, these limb widths usually equal dip-slip on the underlying fault segment. For more complex folds, L_m equals the horizontal component of motion and can be related to slip magnitude.

more complex folds, map view width equals the horizontal component of motion and can often be related to slip magnitude. The parallel projection method can preserve limb (or kink-band) widths, but distorts the horizontal (map-view) position of the fold.

In *VPM* the intersections between axial surfaces and a mapped horizon are projected vertically to the horizontal datum (Figure 4B). When mapping from seismic reflection profiles, this method requires the correlation of a horizon throughout the survey. The vertical projection method preserves the horizontal and vertical (depth or *TWTT*) positions of the structure at the mapped horizon. Therefore, *VPM* maps can be used to construct structure contour maps of the correlated horizon that can be compared with existing maps to test structural interpretations.

In both methods, the intersections between the projected axial surfaces and the datum are plotted on the map plane using anticlinal and synclinal fold symbols (Figure 4). Axial surface maps are then generated by linearly connecting the projected points of the same axial surfaces through the profile grid. Axial surface maps from data can then be compared with maps derived from theoretical models to infer subsurface fold and fault geometries and fault slip. Theoretical maps are made from a series of two-dimensional forward models that are constructed using the quantitative relationships of fault-bend fold theory (Suppe, 1983).

In Figure 6 axial surface maps are constructed above a series of fault-bend fold models that have constant subsurface fault geometry (a 30° dipping ramp connecting decollements) and constant fault slip. These two-dimensional models are cross sections through a balanced three-dimensional fault-bend fold (Figure 7) and could represent, for descriptive purposes, seismic reflection profiles across the fold trend. The patterns of axial surfaces in map view reflect the structural geometry and constant slip on the underlying causative fault. An axial surface map derived by parallel projection (*PPM*) from the same cross sections (Figure 6A) contains

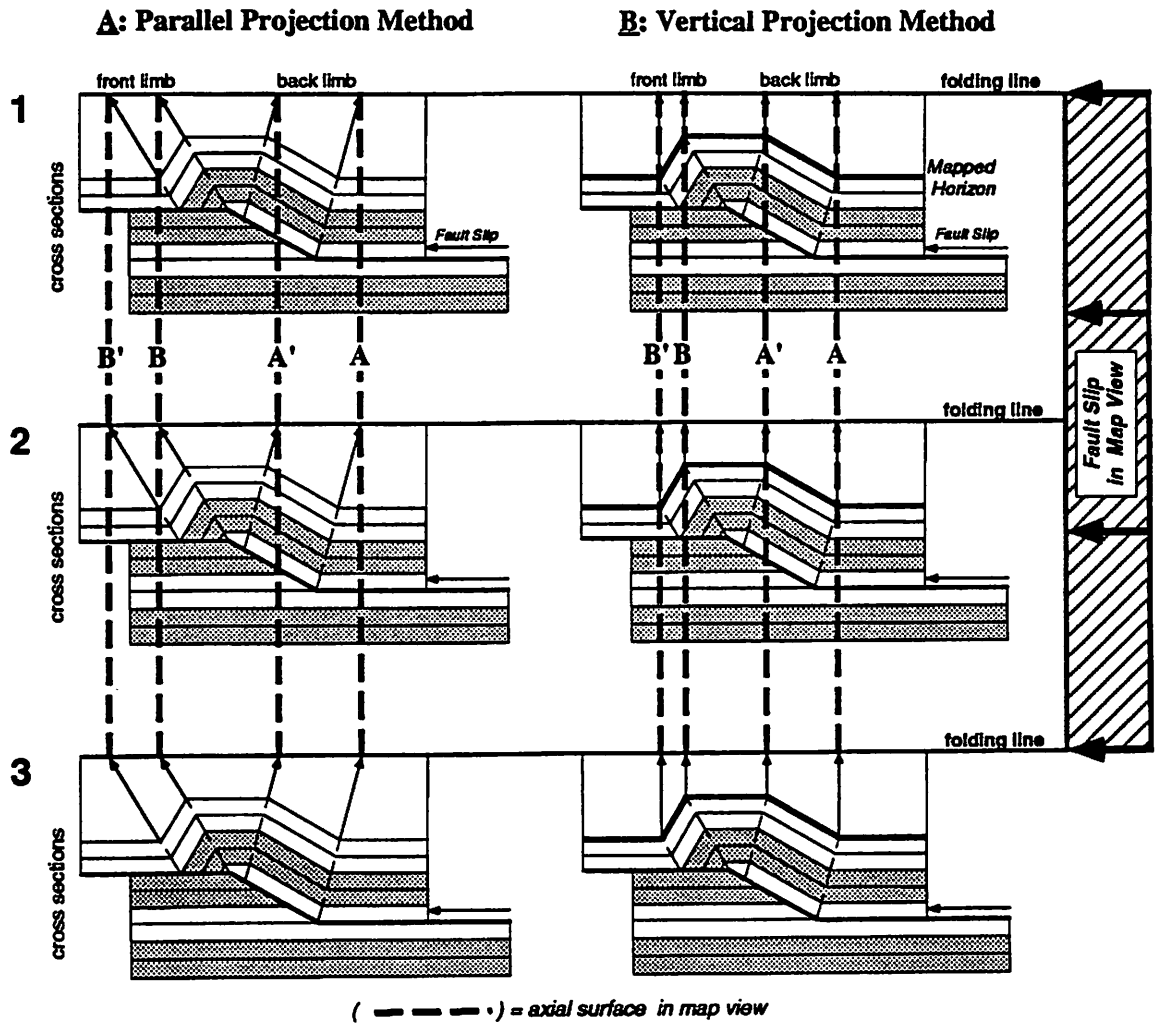

Figure 6: Axial surface maps of a fault-bend fold with constant slip and constant fault geometry along strike. The maps are generated from model cross-sections that lie vertically beneath folding lines over a balanced, three-dimensional fault-bend fold (see Figure 7). Slip on the lower detachment is represented in map view at right and remains constant along strike. A: Axial surfaces mapped by the parallel projection method are straight and parallel to one another reflecting constant slip and constant fault geometry. Map-view kink-band width A-A' equals dip-slip on the underlying fault ramp; B-B' equals slip on the upper decollement. B: Axial surfaces mapped by the vertical projection method are also straight and parallel to one another and preserve the map-view positions of fold hinges at the mapped horizon.

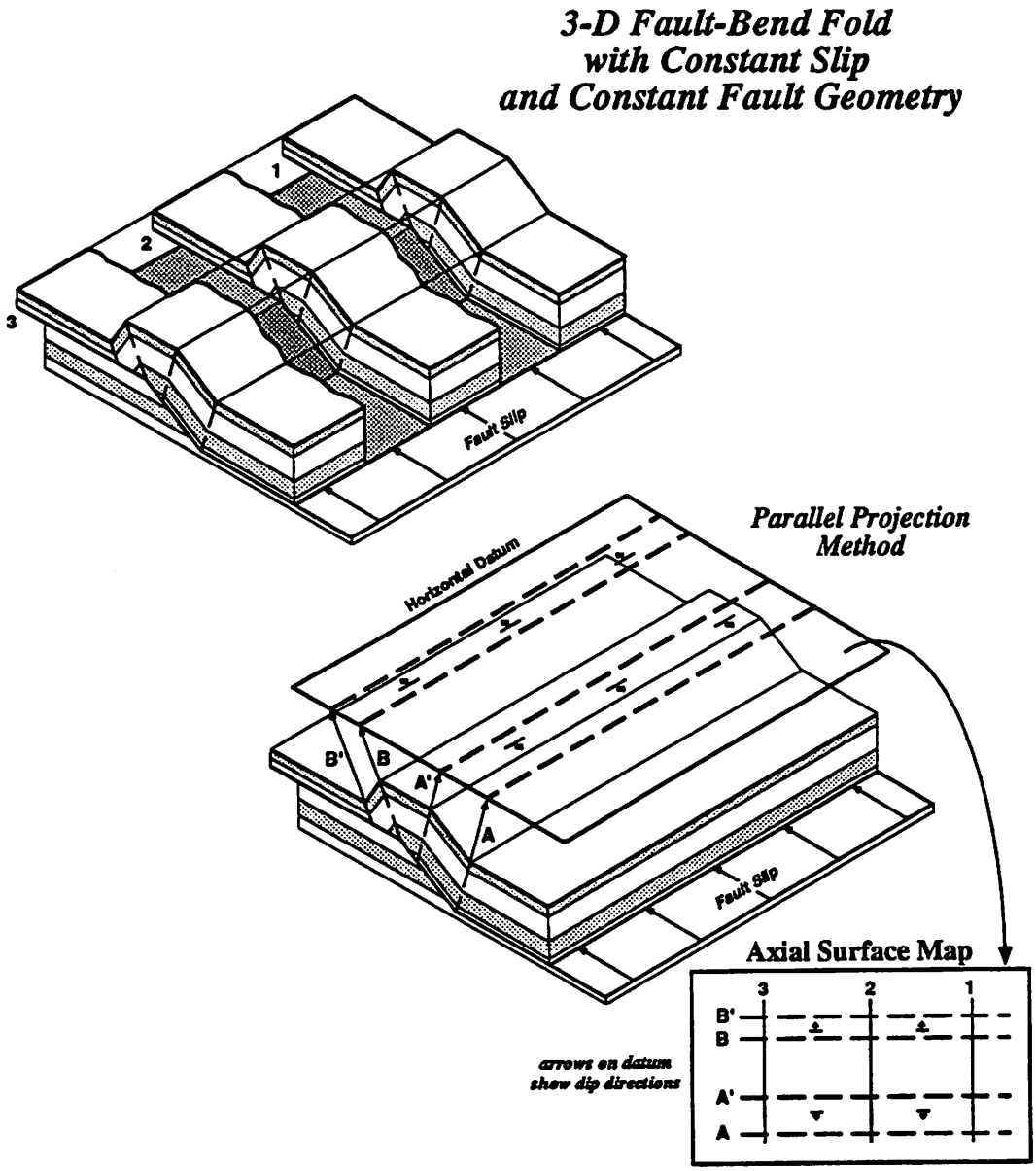

Figure 7: Perspective views of a three-dimensional fault-bend fold with constant slip and constant fault geometry along strike. The cross sections (1, 2, 3) correspond to the two-dimensional models depicted in Figure 6. Axial surfaces mapped by the parallel projection method (shown in map-view at lower right) are straight and parallel to one another reflecting constant slip and constant fault geometry along the underlying thrust. The tectonic transport direction is revealed by the wider back limb kink-band A-A' and narrower front limb kink-band B-B' in map-view.

straight, parallel axial surfaces and constant kink-band widths. Each kink-band width in map view equals the slip magnitude on the underlying fault segment (Figure 5). The back limb width (A-A') equals slip on the underlying fault ramp. The front limb width (B-B') is narrower than the back limb width (A-A') in map view, however, indicating that slip is consumed in folding (Suppe, 1983).

Similarly, an axial surface map of the same models constructed using vertical projection (*VPM*) also contains straight, parallel axial surfaces and constant though narrower limb widths (Figure 6B). Using *VPM*, the horizontal position of the structure at the mapped horizon is preserved; however, the kink-band widths in map view do not equal fold limb widths or fault slip. Both *VPM* and *PPM* map patterns contain narrower front and wider back limbs that indicate fold vergence and the tectonic transport direction. Generally, kink-band and crestal widths are narrower in *VPM* maps than *PPM* maps.

Example 1: Pitas Point, Santa Barbara Channel, California

The Pitas Point fold trend is a producing gas field in the eastern Santa Barbara Channel of southern California. This east-west trending fold consists of a flat crest separating north and south dipping limbs that are approximately 1.7 km wide (Figure 8). Axial surfaces that separate these dip-domains are imaged along the trend in numerous north-south trending seismic reflection profiles. These axial surfaces are mapped in Figure 9 through the seismic grid using the parallel projection method (*PPM*).

Over the portion of the fold trend mapped in Figure 9, the axial surfaces are generally straight and parallel to one another. Therefore, kink-band widths of both fold limbs are roughly constant along strike. This map pattern is similar to that of the fault-bend fold model in Figure 6, in which both fault geometry and slip are constant along strike. In addition, the depth-corrected dips of the fold limbs in cross section

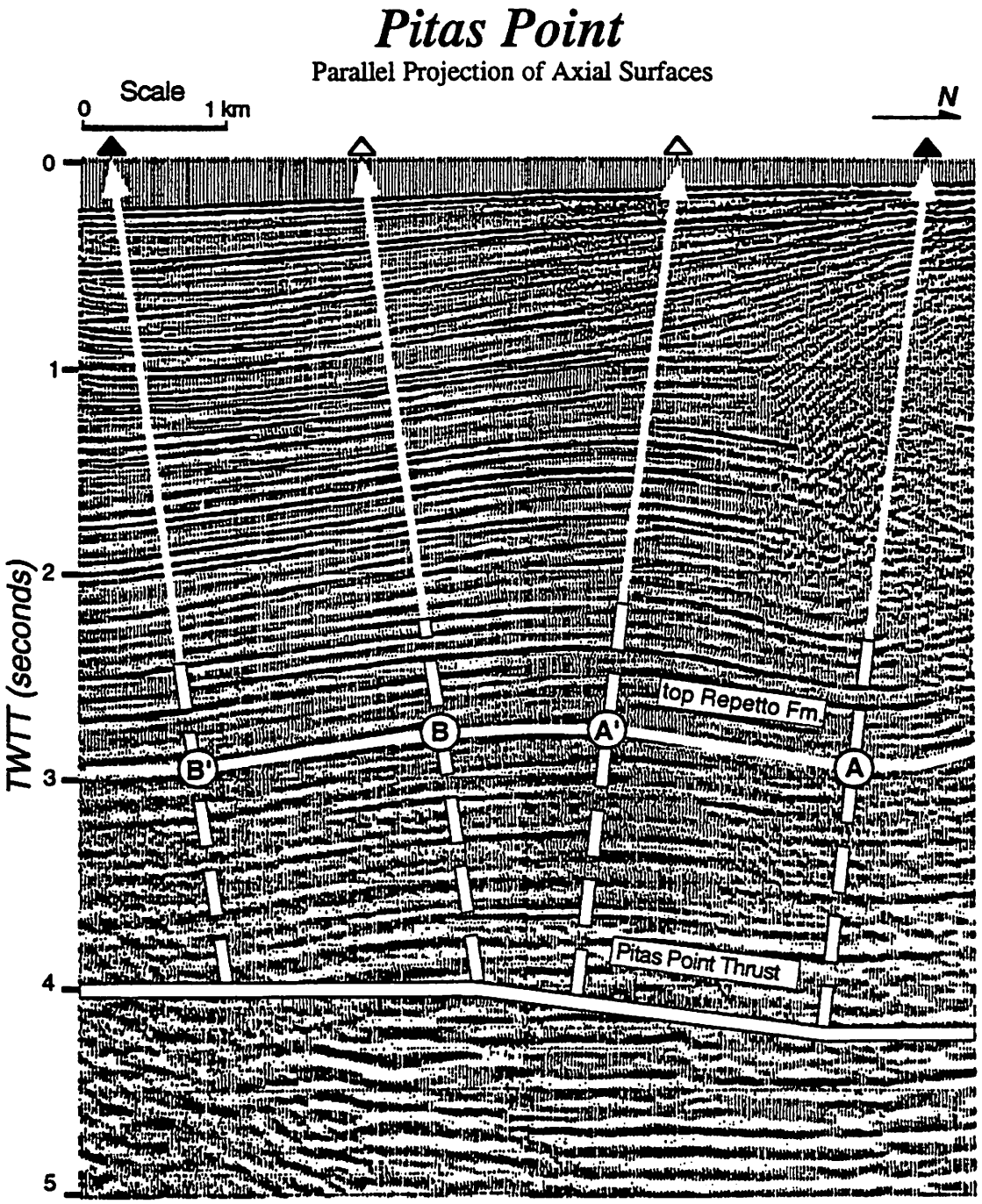

Figure 8: A migrated seismic reflection profile of the Pitas Point anticline in the northeastern Santa Barbara Channel, California (see Figure 20). Axial surfaces that separate dip-domains of reflectors are projected to the seismic datum by the parallel projection method. Note that axial surfaces do not need to extend to the surface to be mapped. The triangles along the datum mark control points used in Figure 9. (The top Pliocene Repetto Formation is mapped by the vertical projection method in Figure 18). Seismic datum (0.00 sec) = sea level. (Seismic profile provided by Occidental Petroleum and Texaco USA).

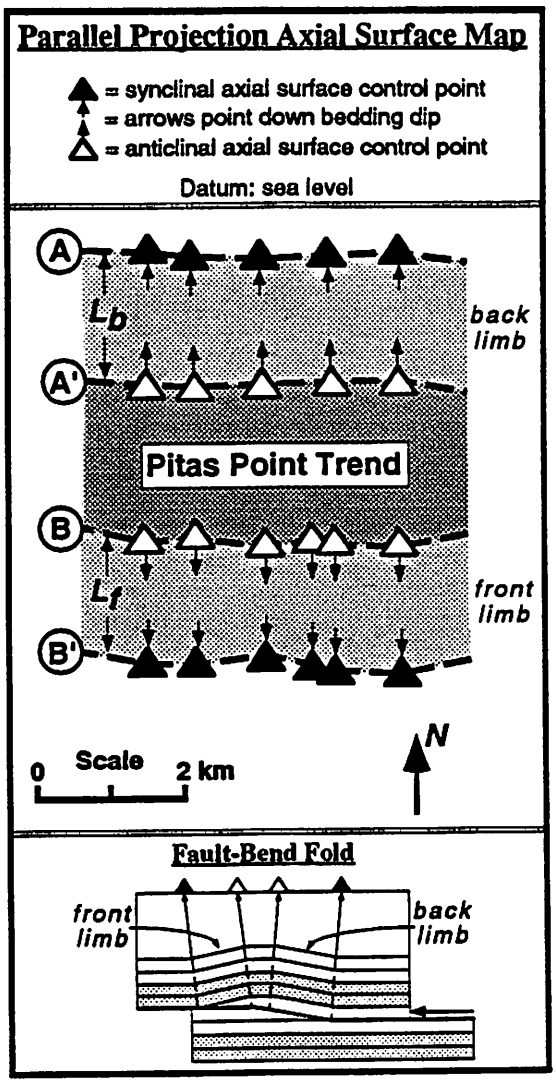

Figure 9: A parallel projection axial surface map of a portion of the Pitas Point trend, California. Axial surfaces are generally parallel and trend east-west. This map pattern suggests that both the slip and geometry of the underlying Pitas Point thrust are constant through the mapped area and that the tectonic transport direction is to the south (see Figures 6 and 7).

(≈12° south limb, ≈11° north limb; Figure 8), are also consistent with fault-bend fold theory (Suppe, 1983) for a ramp dipping 11°N between decollements (Figure 8). Therefore, the fold shapes in the seismic profiles and in axial surface map view are consistent with a fault-bend fold interpretation in which an underlying thrust ramps from a decollement. The map pattern is similar to that of the forward models in Figures 6 and 7, indicating that slip and subsurface fault geometry are constant along strike on Pitas Point thrust (Figure 8). Dip-slip on the thrust is ≈ 1.7 km, equal to the map view kink-band widths (Figure 9).

Lateral Variations in Slip: Plunging Fault-Bend Folds

In the previous example, the parallel axial surfaces in map view indicated that slip on the underlying fault is constant across the mapped region. Lateral changes in slip magnitude along faults, however, produce changes in the overlying fold shape and cause fold plunge (Medwedeff, 1985, 1992; Wilkerson et al., 1991). As faults laterally terminate and/or slip decreases along strike, overlying folds commonly plunge toward the fold termination and this is reflected in the axial surface map pattern (Figure 10). Fold limb (kink-band) widths in cross section become narrower as slip on the causative fault decreases. These narrowing kink-band widths are reflected in map view by non-parallel axial surfaces that converge at zero slip.

In Figure 11 axial surface maps are generated above a series of two-dimensional models through a plunging fault-bend fold. Fault geometry is again held constant; however, slip magnitude linearly decreases to zero along strike. Cross section 0 lies in a position where slip on the underlying fault is zero; hence, it portrays only undeformed strata. Cross sections 1 and 2 are fault-bend folds with progressively more fault slip that is reflected in wider back and front kink-bands. As slip magnitude increases from 1 to 2, fold limb widths and structural relief of the fold crest both increase. At model 2, the back limb inactive axial surface A' reaches the top of the

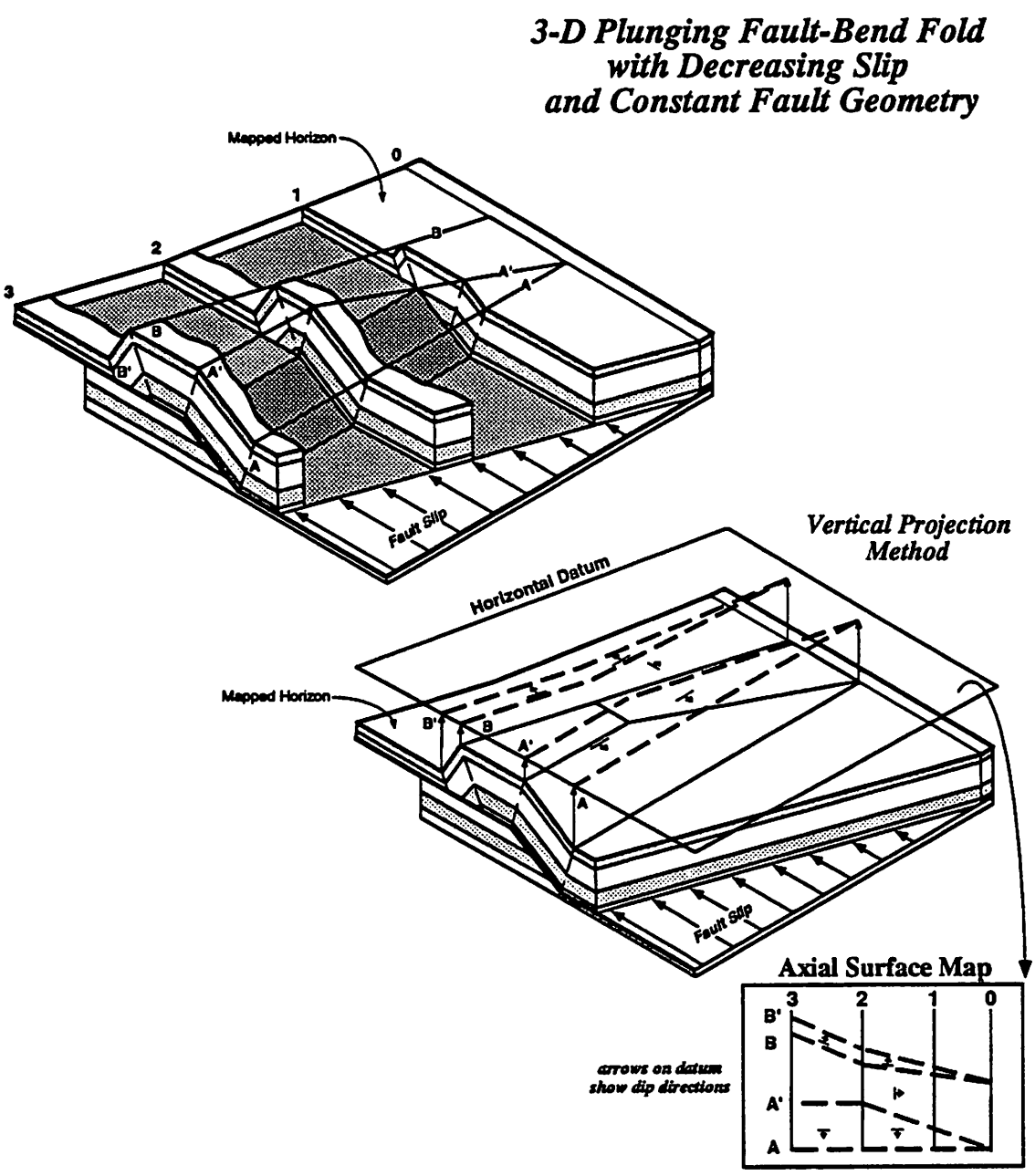

Figure 10: Perspective and map views of a plunging fault-bend fold with decreasing slip and constant fault geometry along strike. Slip on the underlying fault is greatest at model *3* and decreases linearly along strike to zero at model *0*. Decreasing slip causes plunge of the overlying fault-bend fold and is reflected by converging axial surface pairs A-A' and B-B' on the horizontal datum (shown in map-view at lower right). Cross sections *0*, *1*, *2*, and *3* correspond to two-dimensional models depicted in Figure 11. Axial surfaces are mapped by the vertical projection method.

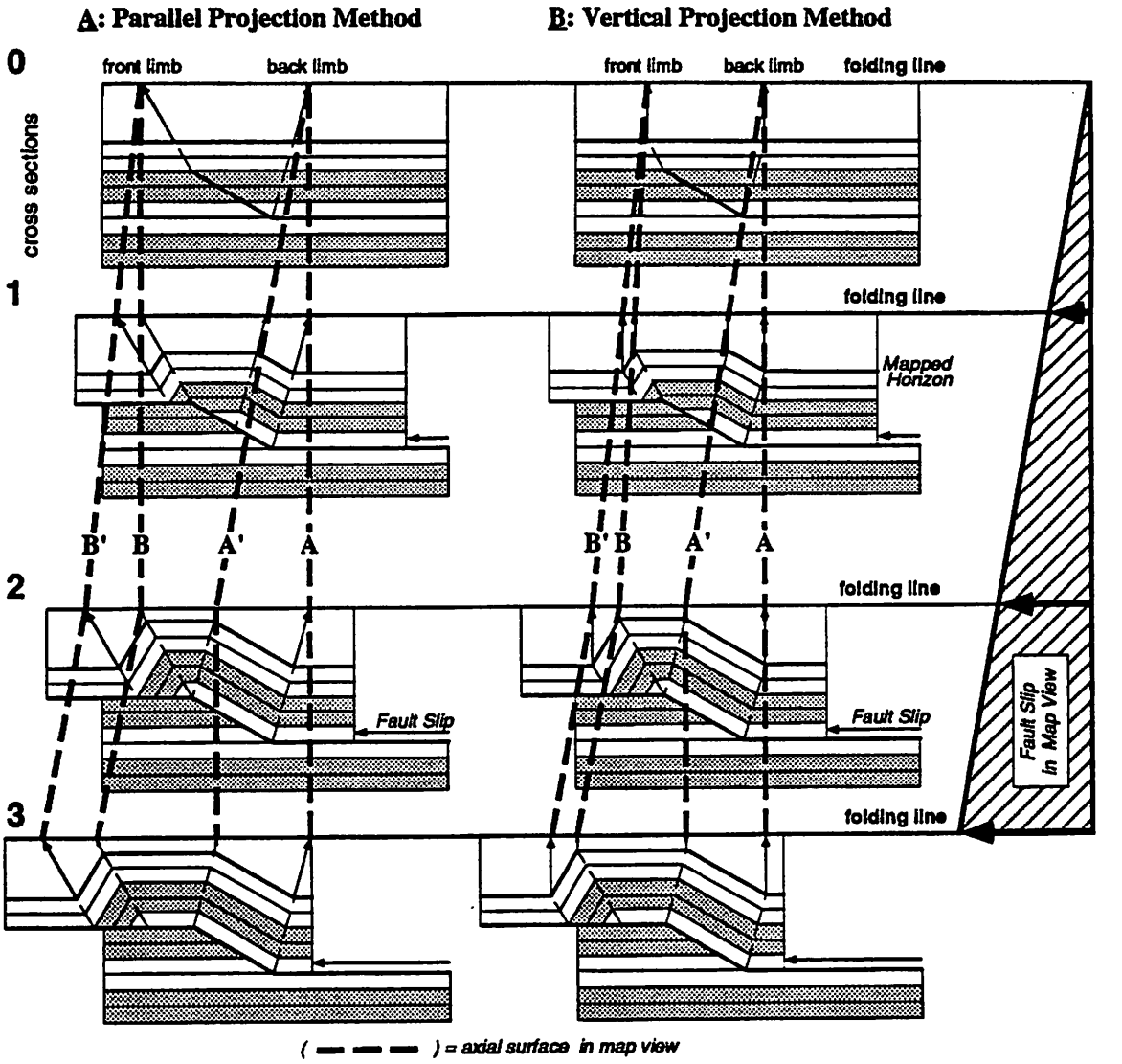

Figure 11: Axial surface maps of a plunging fault-bend fold with decreasing slip and constant fault geometry along strike. The maps are generated from model cross-sections that lie vertically beneath folding lines over a balanced three-dimensional fault-bend fold (see Figure 10). Slip on the lower detachment, represented in map view at right, is greatest at model 3 and decreases linearly to zero at model 0. A: Paired axial surfaces A-A' and B-B' are mapped by the parallel projection method and converge from models 2 to 0 reflecting a decrease in slip on the underlying fault. The change in fold kinematics across model 2 is reflected in the map pattern by translation of the front limb kink-band B-B' along the upper detachment between models 2 and 3. B: Axial surfaces mapped by the vertical projection method show a similar but narrower pattern and preserve the map-view positions of fold hinges at the mapped horizon.

fault ramp. Additional slip (model 3) widens the fold crest without increasing fold limb width and structural relief (Suppe, 1983). Models 1 and 2 are said to be in the *crestal uplift stage* because the fold crest elevates with increasing slip; model 3 is said to be in the *crestal broadening stage* because the fold crest widens with increasing slip.

An axial surface map generated by *PPM* from these models (Figure 11A) shows two pairs of converging anticlinal and synclinal axial surfaces. The back limb active axial surface A remains straight in map view because it is pinned to the underlying fault ramp. Between cross sections 1 and 2, the back limb inactive axial surface A' is also straight, but is not parallel to A and converges with it where slip magnitude is zero (cross section 0). Because the parallel projection method is used, the changing width of the back limb kink-band A-A' is equivalent to the slip magnitude on the underlying fault ramp. Similarly, the front limb active axial surface B, which is pinned to upper fault bend, is straight between cross sections 0 and 2 and parallel to axial surface A. The front limb inactive axial surface B' also converges with the active axial surface B where slip magnitude equals zero. The narrower width of the front limb kink-band in cross section and map view reflects slip consumed in folding.

At cross section 2 (Figure 11), the inactive axial surface A' of model 1 reaches the higher fault bend and becomes fixed to the bend with increasing slip (model 3, Figure 11). Material from the back limb is refolded through A' onto the crest of the structure. Therefore, axial surface A' is "active" between models 2 and 3. More fault slip now increases the width of the crest but does not increase fold limb width. The front limb active axial surface B is released from the higher fault bend and no longer actively folds strata between cross sections 2 and 3 (Figure 11). The front limb width (B-B') reaches a maximum at model 2 and is only translated along the upper detachment with increasing slip between models 2 and 3 (Figure 11).

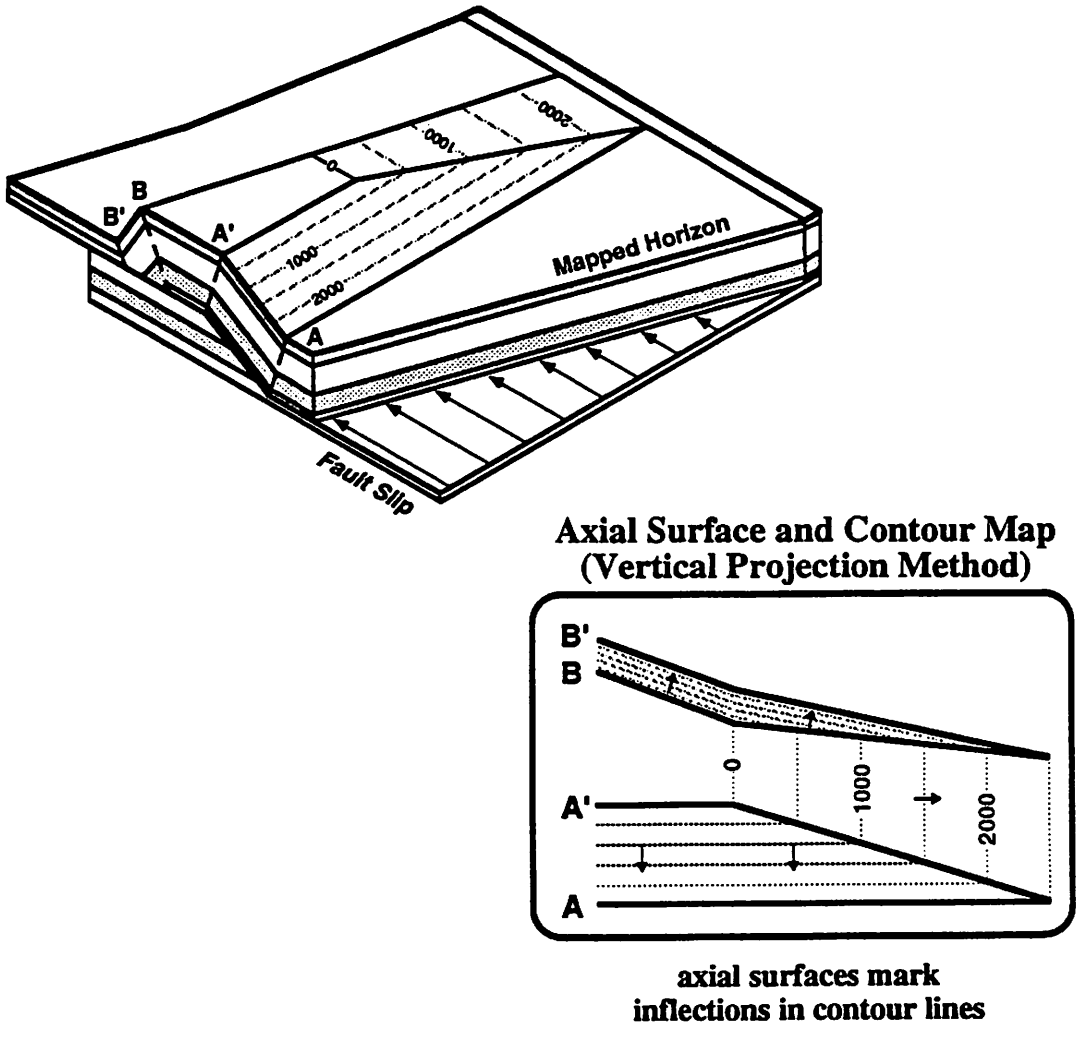

Figure 12: (*Top*) A perspective view of a plunging fault-bend fold with contoured elevations of the mapped horizon below the fold crest. (*Bottom*) Axial surfaces mapped by the vertical projection method define dip domains and inflection points of contour lines.

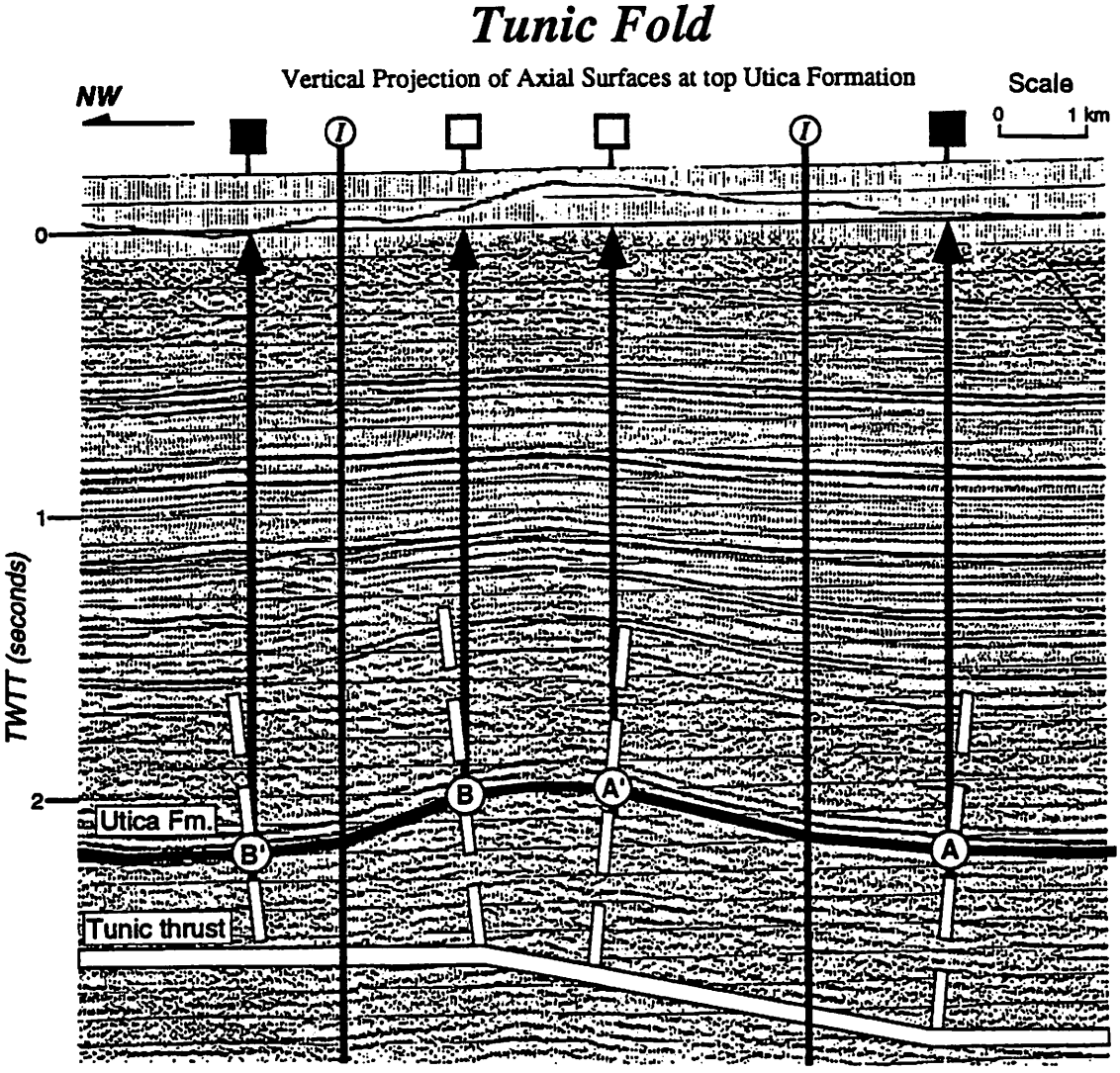

Figure 13: A migrated seismic reflection profile of the Tunic anticline in Sullivan County, Pennsylvania. Axial surfaces that separate dip-domains of reflectors are projected to the seismic datum by the vertical projection method from the top of the Ordovician Utica Formation. The squares along the datum mark control points used in Figure 14. The symbol (I) marks bends in the map-view trace of the seismic profile that result in inflections of the fold limbs due to the imaging of apparent dips from out of the plane energy. Seismic datum (0.0 sec) = 1500 ft. (Seismic profile provided by Texaco USA).

fold. At Pitas Point the back synclinal axial surface is straight in map view and the other three axial surfaces are parallel to it (Figure 8). At Tunic only the southeast, synclinal axial surface is a continuous straight line in map view. The other three axial surfaces are not parallel to the southeast syncline and have distinct bends in them at line 2.

The synclinal axial surface of the southeast fold limb (A, Figures 13, 14) is straight in map view and trends E-NE. The paired anticlinal surface A' diverges from A between profiles 1 and 2, is at its maximum distance from A at profile 2, then converges toward A between profiles 2 and 3. Therefore, the kink-band width of the southeastern fold limb is greatest in the center of the trend and decreases in both directions along strike. The map pattern of the northeast limb appears similar, although it is not completely constrained in profile 1. The anticlinal axial surface of the northern limb (B, Figure 14), bends slightly at line 2 and is sub-parallel to the synclinal axial surface of the southern fold limb A. The kink-band width of the northern limb (B-B') is narrower than the southern limb (A-A') although both widen toward line 2 (Figure 14). Also note that the crest of the fold is narrowest and the structural elevation (in TWTT) is greatest along profile 2, consistent with the pattern of a fault-bend fold (Figures 11, 12).

The map pattern of the Tunic structure (Figure 14) is consistent with the map pattern of a doubly plunging fault-bend fold model in which slip decreases from profile 2 in both directions along strike on the underlying causative fault (Figure 15). Doubly plunging fault-bend fold models can be constructed by keeping fault geometry constant and simply decreasing slip magnitude from some maximum in both directions along strike. Both *PPM* and *VPM* (Figure 15) axial surface maps show kink-bands widths that decrease toward zero slip on the fault.

The map patterns in Figure 15 differ with respect to the maximum amount of fault slip relative to the fault-ramp width and the projection method. In plunging fault-bend

Tunic Fold, Sullivan County, Pennsylvania

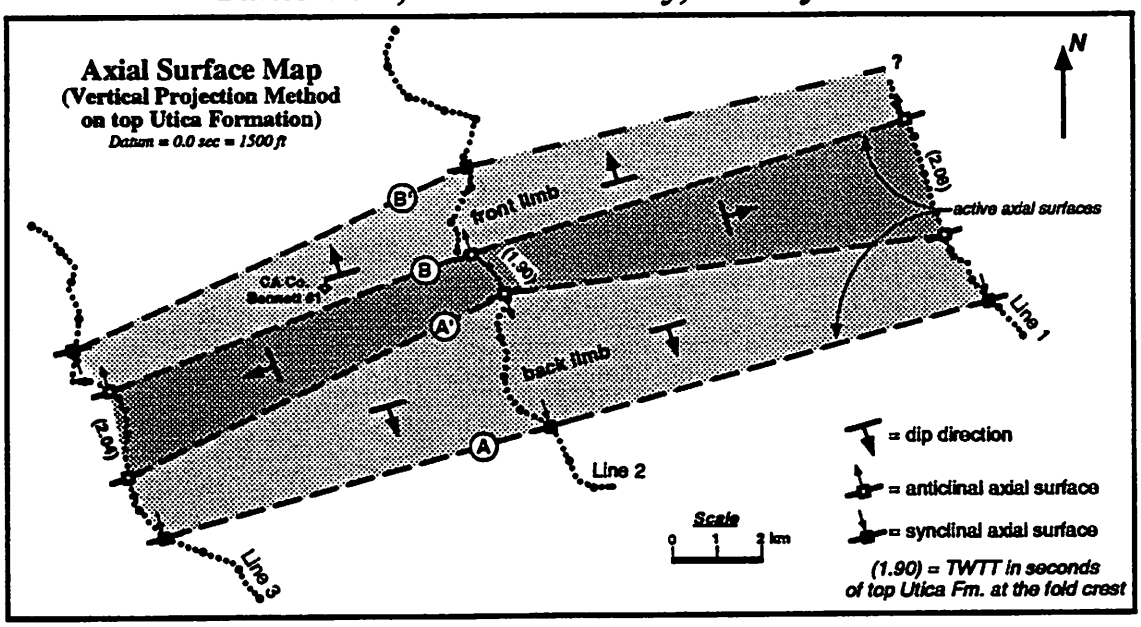

Figure 14: A vertical projection axial surface map of the Tunic fold at the top Ordovician Utica Formation. Both back limb A-A' and front limb B-B' kink-bands have maximum widths along line 2 that decrease in both directions along strike as paired axial surfaces converge. The Tunic map pattern suggests that slip on the underlying causative thrust decreases laterally in both directions from line 2 causing the fold to plunge in both directions along strike (compare with Figure 15B-1). The tectonic transport direction is to the northwest. Note that the maximum structural elevation and the narrowest crest occur along line 2.

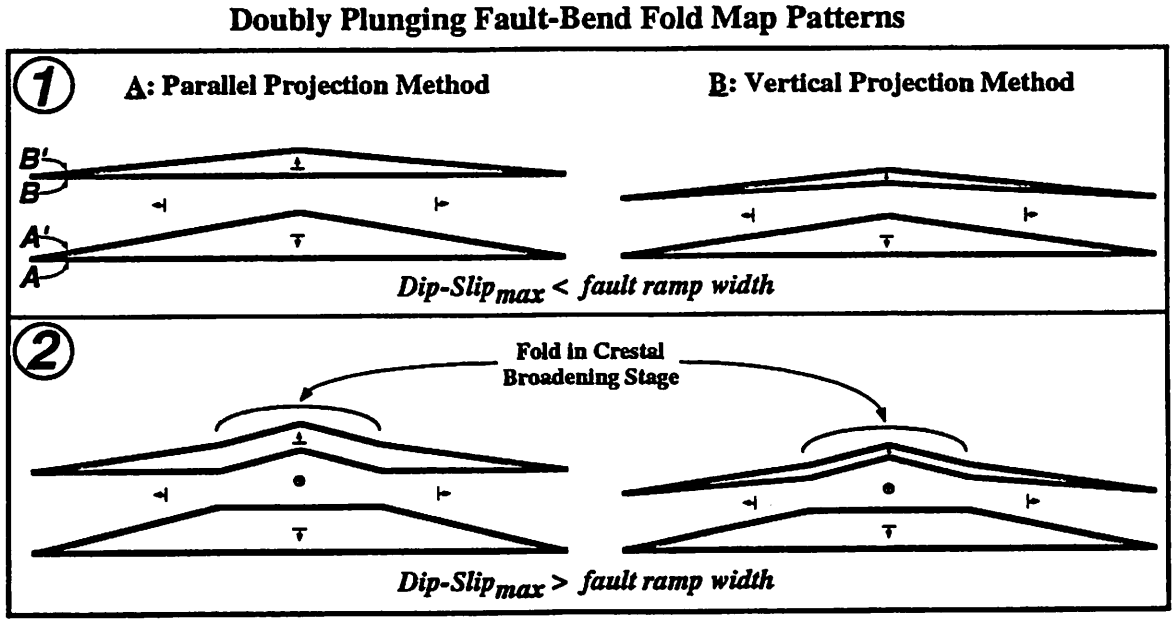

Figure 15: Axial surface map patterns of doubly plunging fault-bend fold models in which fault geometry is constant and slip decreases linearly in both directions from the center along strike. Map view kink-bands A-A' and B-B' reflect slip on the underlying fault segments and narrow along strike in both directions. 1: Maximum dip-slip is less than fault ramp width; therefore, the fold is everywhere in the *crestal uplift stage*; 2: Maximum dip-slip is greater than fault ramp width; therefore, the fold enters the *crestal broadening stage* near the center of the trend (see Figure 3).

folds in which maximum slip is less than the width of the fault ramp in cross section (Figure 15-1), axial surface A' does not reach the higher fault bend (Figure 11-model 1). Therefore, axial surface A' is nowhere parallel to axial surface A in map view (Figure 15). In plunging fault-bend folds in which slip is greater than the width of the fault ramp in cross section (Figure 15-2), axial surface A' is parallel to A and the front limb axial surfaces (B and B') are translated above the upper decollement (see Figure 11). In the Tunic fold the axial surfaces of the southeastern limb (A and A', Figure 14) are nowhere parallel in map view, similar to the former case (Figure 15-1). This suggests that the Tunic fold lies everywhere in the crestal uplift stage of growth (Figure 11A).

Lateral Variations in Fault Geometry: Fault Ramp Location

Lateral terminations or disruptions of fold trends can be caused by changes in underlying causative fault geometry as well as variations in slip (Wilkerson et al., 1991). Changes in subsurface fault geometry, which include tear faults, oblique ramps, and variations in decollement level, are often highlighted by terminations, bends, or offsets of axial surfaces in map view. In the simple case of a fault ramp with constant slip and step up-angle, axial surfaces are offset in map view above a subsurface tear fault (Figure 16). The trend of the line of offset in map view often approximates the direction of slip on the underlying detachment (Shaw et al., 1992; Shaw and Suppe, 1993).

Changes in the positions of decollements along strike are also reflected in the shape of the overlying fold (Wilkerson et al., 1991), although the effects can be subtle. This point is illustrated in Figure 17, in which the positions of both the upper and lower decollements change to shallower levels between models 1 and 2. The upper and lower decollements lie at the same higher structural levels in both models 2 and 3. In this case, even with constant slip on the underlying detachment, the

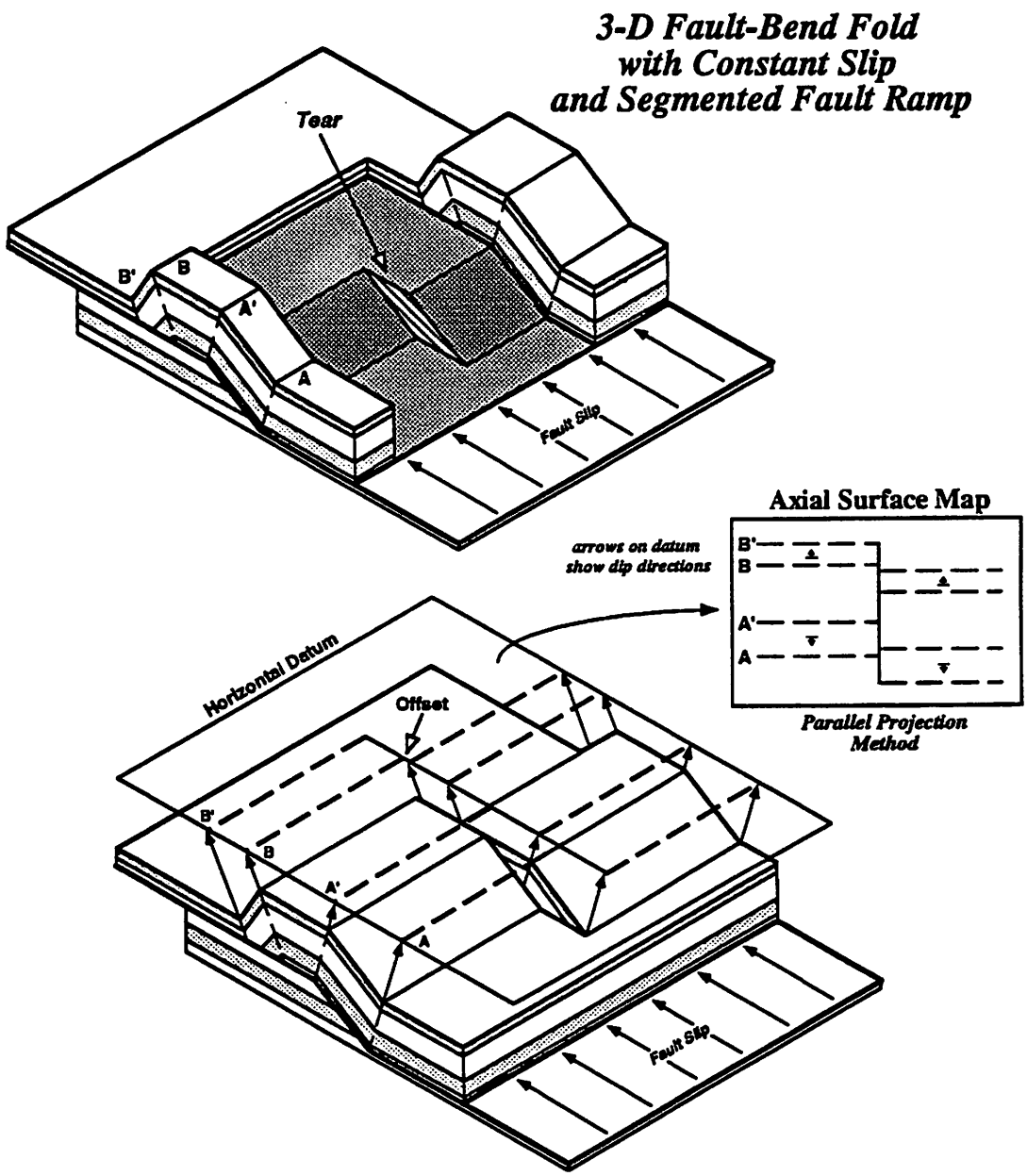

Figure 16: Perspective and map views of a fault-bend fold with constant slip and a fault ramp offset by a subsurface tear. This change in fault geometry is reflected by the axial surface map pattern. Axial surfaces mapped by the parallel projection method (shown in map-view at right) are straight and parallel to one another reflecting constant slip and constant geometry of the underlying thrust along strike. However, axial surfaces are offset in map view above the tear fault. In this model, the orientation of the line that offsets axial surfaces in map view is also the slip direction.

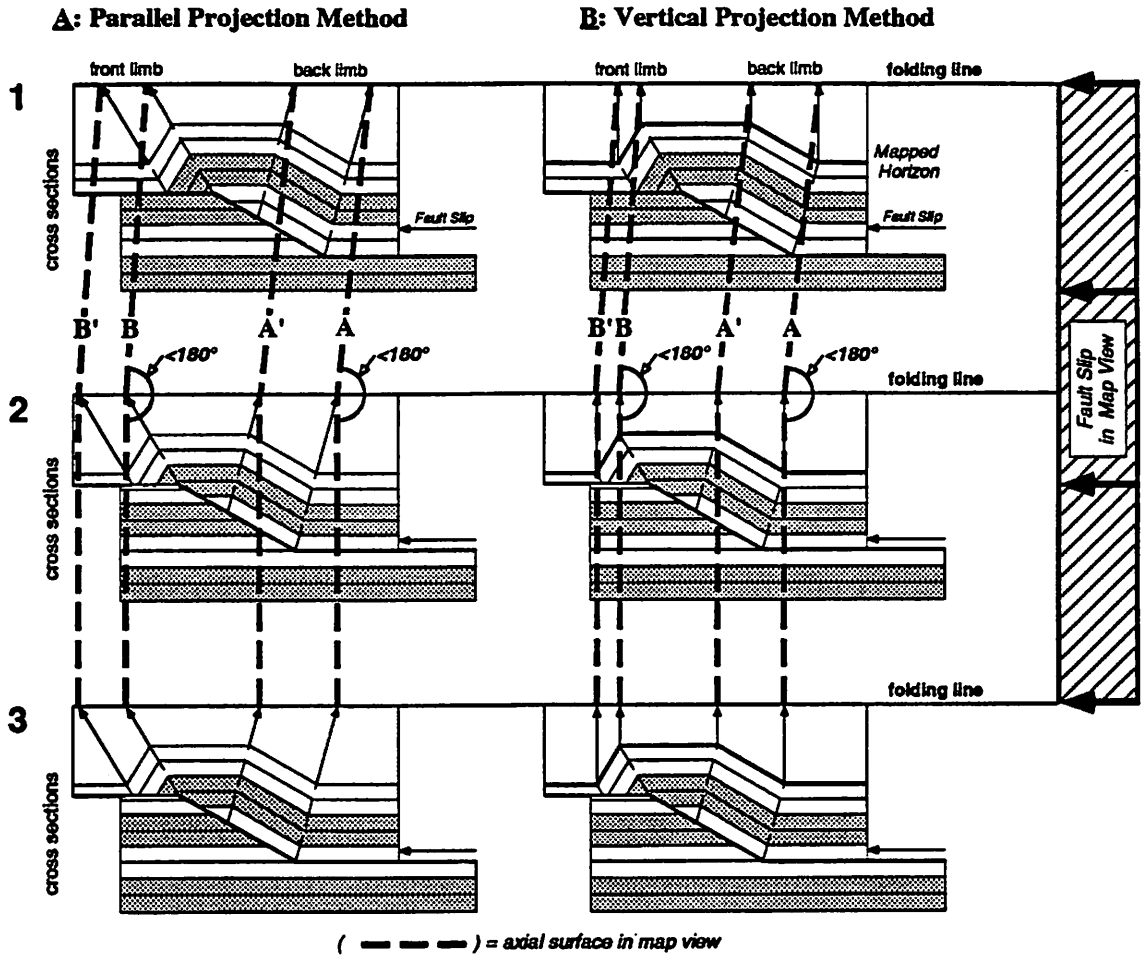

Figure 17: Axial surface maps of a fault-bend fold with constant slip and changing fault geometry along strike. The maps are generated from model cross-sections that lie vertically beneath folding lines over a balanced three-dimensional fault-bend fold. Back limb axial surfaces A-A' bend in map view across model 2 as the lower fault bend and decollement cut up section from models *1* to 2. Front limb axial surfaces B-B' bend in map view across model 2 as the upper fault bend and decollement cut up section from models *1* to 2.

different positions of the fault bends produce subtle variations in overlying fold shape. The map-view orientations of the axial surfaces in Figure 17 change at model 2, creating slight inflections in all of the axial surfaces. The inactive axial surfaces A' and B' are everywhere parallel to the active axial surfaces A and B because slip does not vary along strike.

In general, axial surface map patterns reflect fold kinematics, fault geometry, and slip along trend. In some cases, map patterns cannot be uniquely interpreted because several, combined changes in fold kinematics, fault geometry, and slip can produce similar map patterns. As we demonstrate in the following example, interpretation of seismic reflection data and construction of balanced geologic cross sections are usually required to choose among possible structural solutions to an axial surface map pattern.

Example 3: Santa Barbara Channel, CA, revisited;

The Pitas Point trend, described in Example 1 and imaged on the seismic reflection profile in Figure 8, dies out gradually to the west; this fold termination is reflected by convergent axial surface pairs in map view (Figure 18). The synclinal axial surface A of the northern fold limb bends slightly northward from the trace mapped to the east of line 2. This change suggests that the map-view location of the lower fault bend moves slightly northward. The southern anticlinal axial surface B (Figure 18) runs west-northwest; slightly oblique to the axial surface A. This map pattern suggests that the upper decollement cuts down section to the west (similar to the map pattern between models 1 and 2, Figure 17). In addition, narrowing of both the northern and southern kink-bands in map view (Figure 18) without a significant change in fold limb dips suggests that slip also decreases to the west along strike. Therefore, changes in both fault geometry and slip, which are reflected in the axial surface map pattern, can generate the western termination of the fold trend.

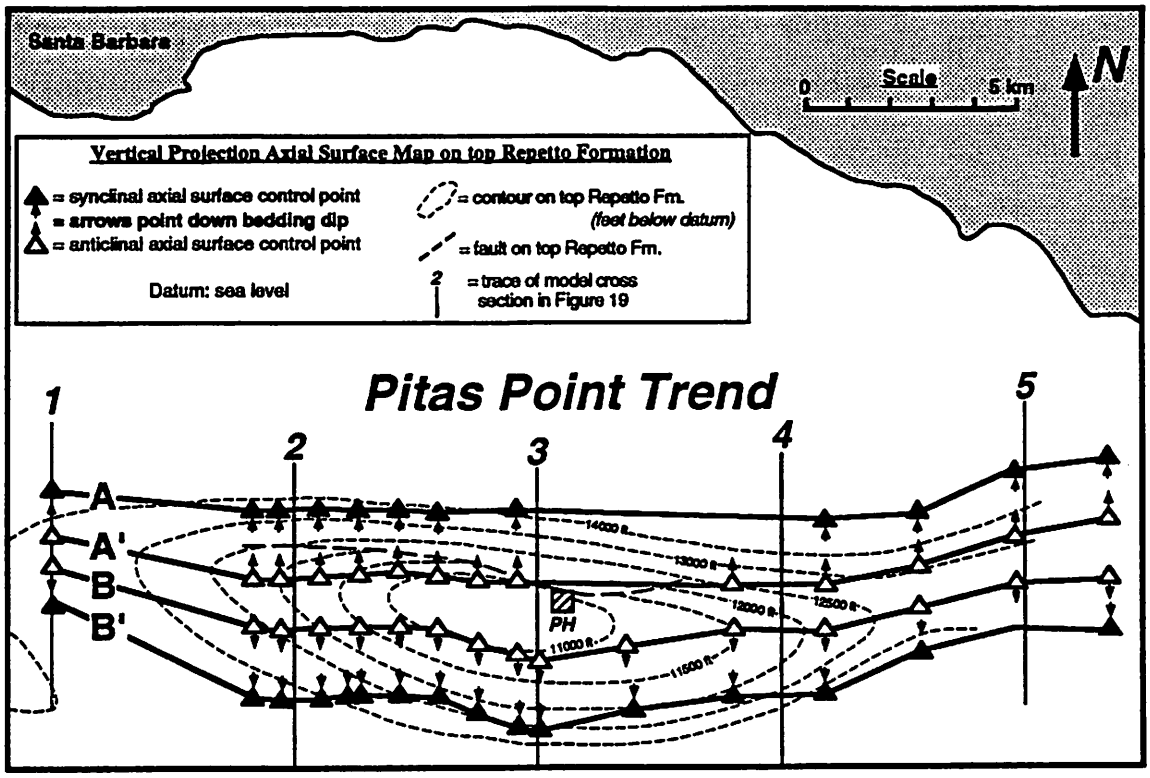

Figure 18: A vertical projection axial surface map on the top Pliocene Repetto Fm. of the Pitas Point trend, a producing gas field in the Santa Barbara Channel of southern California. The axial surface map pattern defines the trend, closure, and area of maximum structural elevation of this fault-bend fold. Lateral closure is suggested by narrowing kink-band widths to both the east and west along strike. The increased separation of the anticlinal axial surfaces A' and B near cross section *3* suggests that the fold has reached maximum structural elevation and entered the crestal broadening stage along the center of the trend. These inferences, derived from the axial surface map pattern alone, are confirmed by a structure contour map of the top Repetto Formation generated previously from well data (contour map provided by Texaco, Inc.). Model cross-sections *1-5* are shown in Figure 19; (PH) marks the platform Habitat.

confirms the lateral plunge and area of maximum structural elevation of the fold predicted from the axial surface map pattern. We suggest that *VPM* axial surface maps should be used in other cases of limited subsurface data to constrain contour maps (Figure 12).

The more complete axial surface map of the Pitas Point trend (Figure 18) provides direct information on fold kinematics, fault geometry, and slip. The axial surface map pattern compared with forward model solutions helps to define: 1) the extent of the structural trend, including the location and geometry of fold closure; 2) lateral slip distribution on the underlying fault and regions of high structural relief; and 3) changes in subsurface fault geometry along strike. These inferences combined with the axial surface map were used to construct a three-dimensional structural interpretation of Pitas Point trend (Figure 19).

Multiple Fold Trend Analysis

In many sedimentary basins, analyses of multiple fold trends are required to assess exploration potential and develop accurate subsurface interpretations. In the eastern Santa Barbara Channel, Pitas Point is only one of a number of fold trends that have attracted exploration interest. Two of these structures, the Offshore Oak Ridge and Blue Bottle folds, also trend approximately east-west and lie south of the Pitas Point field (Figure 20). The parallel projection axial surface map across these three folds in Figure 20 provides insight into a structural interpretation of the eastern Santa Barbara Channel. Prior to detailed contouring or structural analysis of the individual fold trends, the axial surface map patterns could be used to define the approximate locations and geometries of the folds and constrain slip magnitudes on the underlying causative fault(s).

In previous sections, we contended that the axial surface map pattern of the Pitas Point trend was consistent with a fault-bend fold interpretation in which the thrust

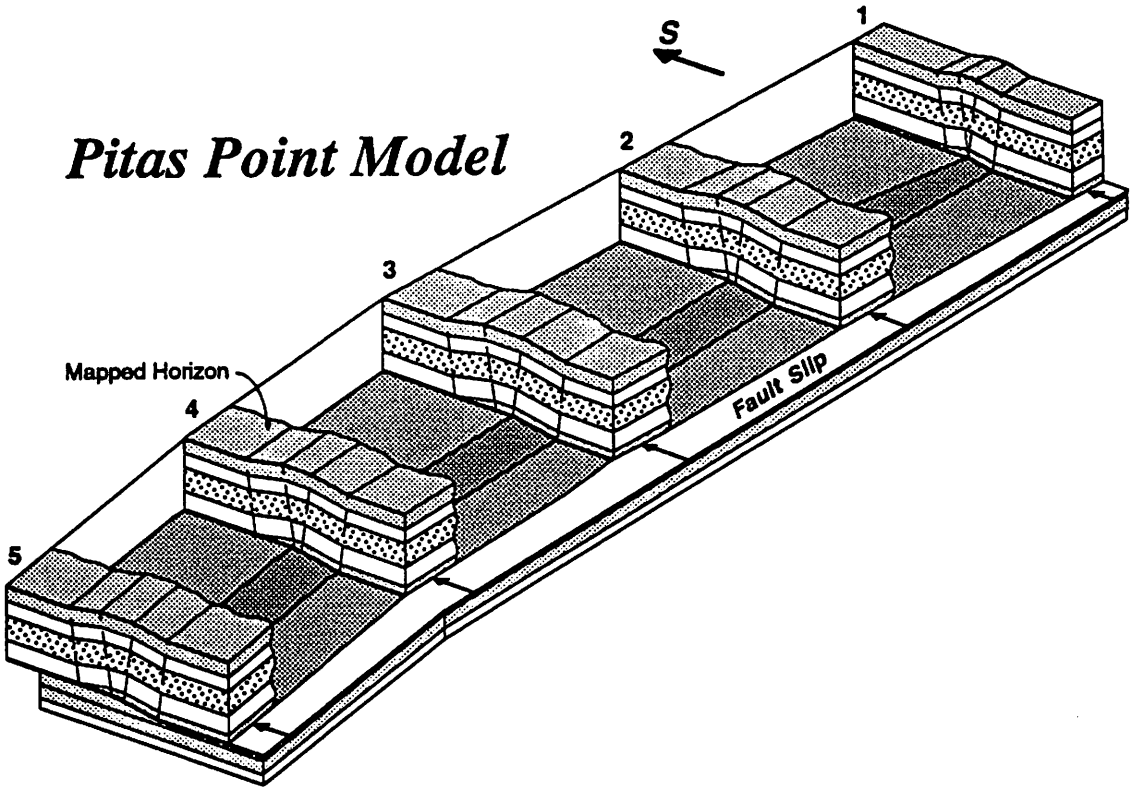

Figure 19: A perspective view of a three-dimensional Pitas Point model generated from the map pattern of axial surfaces in Figure 18. Slip on the Pitas Point thrust decreases in both directions along strike from model *3*. Maximum structural elevation of the mapped horizon at the fold crest occurs at model *3* where the fold is in the crestal broadening stage; the upper and lower detachments cut down in section from models *2* to 1; and the strike of the fault ramp changes from models *4* to *5*.

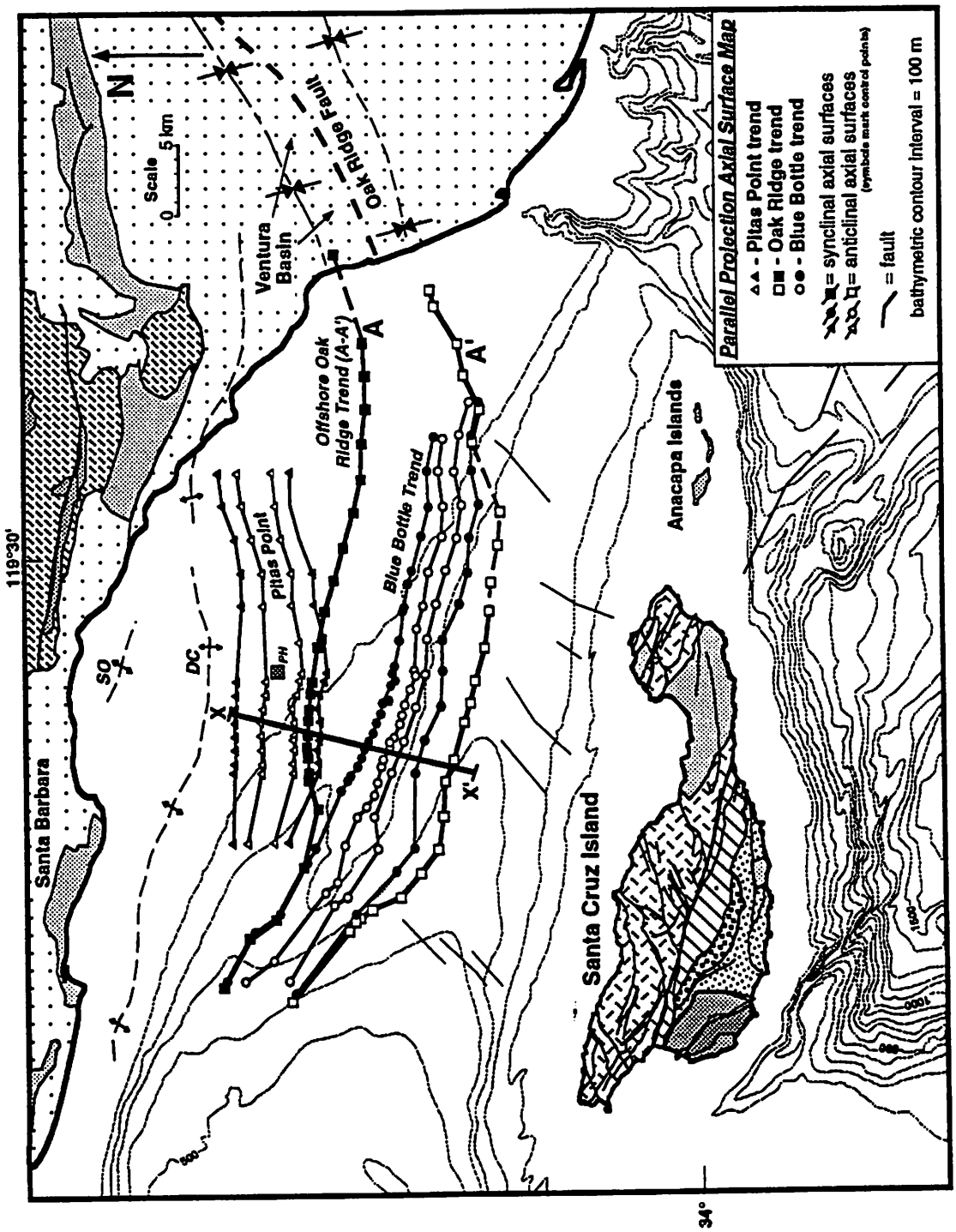

Figure 20: A parallel projection axial surface map of the Pitas Point, Offshore Oak Ridge, and Blue Bottle trends in the eastern Santa Barbara Channel, California. Kink-band widths between pairs of anticlinal and synclinal axial surfaces generally reflect slip on the causative thrust beneath each trend. The similar kink-band widths of the Pitas Point and Blue Bottle trends suggest that slip to the south on the Pitas Point detachment generates the Blue Bottle anticline (Figure 21). Slip on the Channel Island thrust fault beneath the Offshore Oak Ridge fold, reflected by kink-band width A-A', is an order of magnitude greater. The Channel Island thrust ramp uplifts the Santa Cruz and Anacapa Island shelf; the shape of the uplifted island shelf reflects slip distribution along the thrust recorded by the kink-band width A-A' (Shaw and Suppe, 1993).

fault steps up to the south (Figure 19). Dip-slip on the causative fault beneath Pitas Point is equal to the kink-band widths of the fold limbs in map view (except where the fold is in the crestal broadening stage). Along strike, fault dip-slip varies from 1 to 2 km. A critical next step in developing a regional cross section is to determine if slip leaving the Pitas Point structure generates the Offshore Oak Ridge or Blue Bottle trends. The three fault-bend folds could lie in series above a single causative fault, or alternatively, be generated above independent faults. If the folds are in series, then they would develop simultaneously and fault slip and kinematic information from one fold trend could be used to interpret other folds in the series.

The proximity of the Offshore Oak Ridge and Pitas Point trends suggests that the two fault-bend folds could be inter-related by sharing a common thrust. However, the 10 km kink-band width of the Offshore Oak Ridge fold (A-A') is considerably greater than the 1 to 2 km range of fault slip beneath Pitas Point (Figure 19). This difference strongly suggests that any workable structural interpretation must include at least two faults. In contrast, the kink-band width of the Blue Bottle fold is approximately equal to slip beneath Pitas Point. Therefore, a structural interpretation that involves a single causative fault beneath Pitas Point and Blue Bottle and a second fault beneath the Offshore Oak Ridge trend is plausible.

Finally, no additional fold trends or kink-bands are recognized in the Oxnard shelf or Channel Islands (Figure 20) that are similar in width to dip-slip beneath the Blue Bottle trend. Therefore, it is likely that slip on the Pitas Point fault is either consumed in Blue Bottle folding or locally reaches the seafloor. In contrast, slip on the causative fault beneath the Offshore Oak Ridge trend, recorded by the kink-band width (A-A'), is reflected farther to the south in the regional geology and bathymetry of the Channel Islands. The Oak Ridge kink-band and, therefore, slip on the underlying fault, decrease laterally in both directions along strike. In addition, the kink-band A-A' bends sharply due south of Santa Barbara to trend northwest-

southeast. To the southwest of the Offshore Oak Ridge trend, this fold shape and slip distribution pattern is reflected in the length and width of the Santa Cruz and Anacapa Island shelf (Figure 19). The islands generally trend east-west, parallel to Oak Ridge fold trend. The change in trend of the fold to northwest, due south of Santa Barbara, is also parallel to the change in trend of Santa Cruz Island reflected by its western promontory. To the east, both the kink-band width of the Offshore Oak Ridge trend and the size of the island shelf decrease. These similarities suggest that the shelf and fold trend may somehow be related, possibly by slip distribution along a connecting fault system (Shaw and Suppe, 1993).

We infer from the axial surface map pattern of the eastern Santa Barbara Channel that: 1) the Pitas Point trend is a fault-bend fold in which the thrust fault steps up to the south and has 1 - 2 km of total slip; 2) the Blue Bottle trend may have been generated above the same thrust fault as the Pitas Point fold; 3) the Offshore Oak Ridge fold is generated by a second, independent thrust fault with about 10 km of slip; and 4) the causative fault beneath Oak Ridge may extend to the south beneath the Channel Island Shelf. These inferences, which were derived from axial surface map analysis prior to detailed contouring or structural analysis of individual trends, provide important constraints in developing a reasonable subsurface interpretation that includes cross sections (Figure 21) and forward models.

SUMMARY AND CONCLUSIONS

Many folds in the upper crust form by slip through bends in underlying faults (Rich, 1934; Suppe, 1983). Axial surfaces (fold hinges) define the fold geometry and are related to fault bends. Therefore, maps of axial surfaces derived from balanced models, seismic reflection profiles, and/or cross sections constrain fold trends and underlying fault geometry and slip. Axial surfaces can be mapped by projecting their locations in vertical sections to a horizontal datum using either the Parallel Projection

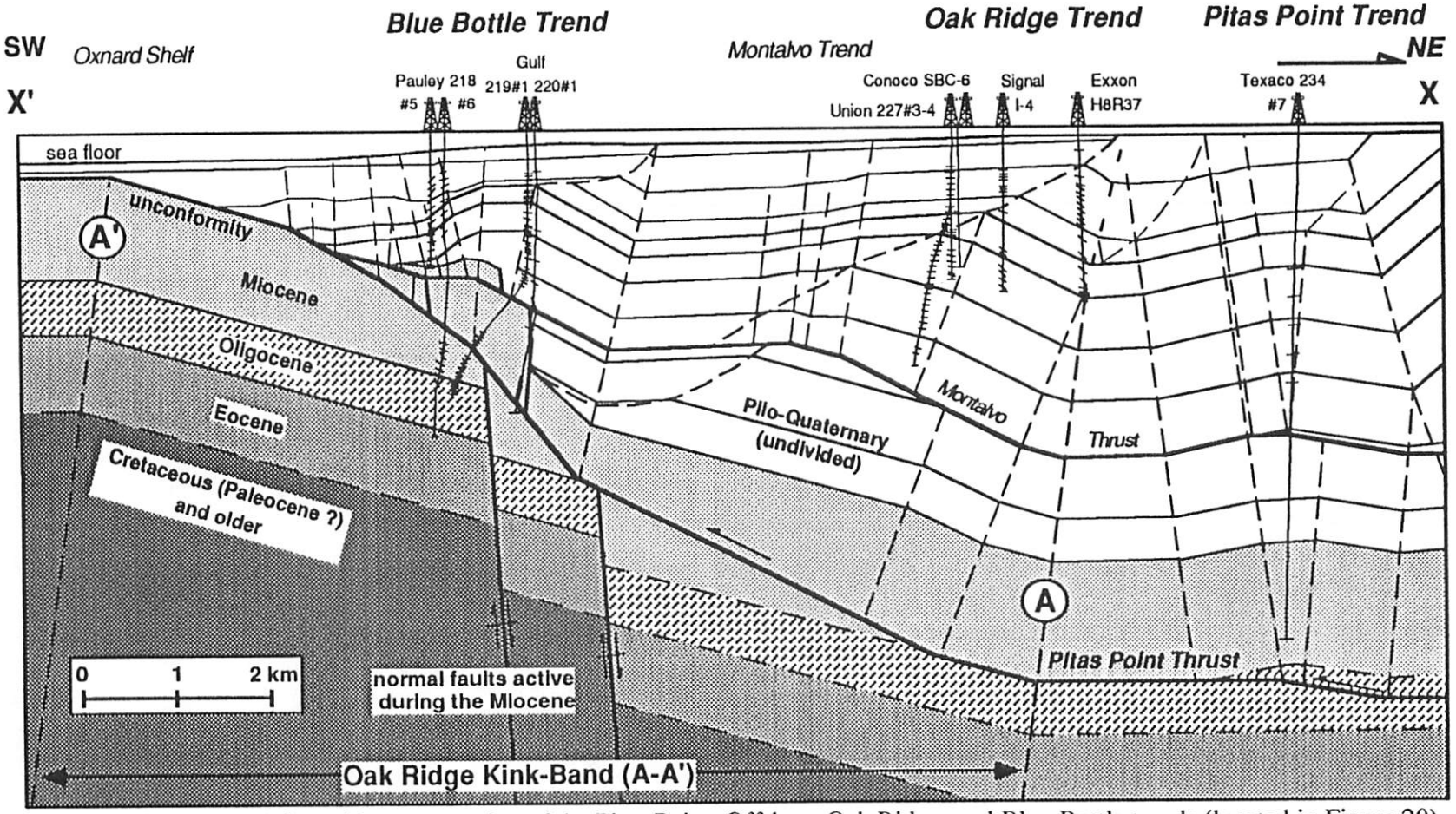

Figure 21: A retrodeformable cross section of the Pitas Point, Offshore Oak Ridge, and Blue Bottle trends (located in Figure 20) that integrates seismic reflection, well log, and axial surface map data. The Pitas Point thrust generates the overlying Pitas Point and Blue Bottle trends, whereas a fault below the depth of section (Channel Island thrust) generates kink-band A-A' of the Offshore Oak Ridge trend. Kink-bands narrow upward into Pliocene and Quaternary syntectonic (growth) section (Suppe et al., 1992; Shaw and Suppe, 1993). The Texaco #7 well lies in the plane of the cross section; additional wells are projected into the cross section plane along tie lines.

(*PPM*) or Vertical Projection (*VPM*) Methods. Axial surface maps are constructed by connecting points of individual axial surfaces through the grid of profiles or cross sections. Parallel projection maps are easy to construct and provide direct information on underlying fault slip. Parallel projection maps can be constructed in areas of limited control to define trends, estimate fault geometry and slip, and relate structures to their causative faults. Vertical projection maps define the locations of folded structural horizons and can be used to obtain detailed subsurface structural geometries of a single horizon.

Axial surface maps constructed from balanced forward models highlight specific relationships between map patterns and structural geometries and fault slip. Parallel axial surfaces in map view often reflect constant slip and constant fault geometry along strike. Alternatively, a narrowing kink-band width generally reflects decreases in fault slip magnitude along strike. Terminations, sharp bends, or offsets of axial surfaces may occur above distinct changes in fault geometry (including fault tears and changes in fault ramp dip and location).

Axial surface mapping through seismic reflection grids is an efficient method of defining fold trends and highlighting regions of high structural relief, fold closure, and structural complexity. For example, the axial surface map of the Tunic Fold (Example 2; Figures 13 and 14), here constructed from only three seismic reflection dip lines, defines this doubly plunging fold trend and constrains underlying fault slip. Combined, map-view analysis and cross sections let us approach a better understanding of natural three-dimensional structural geometries. However, axial surface maps and cross sections neither address all of the geometric and kinematic properties of natural folds, nor are they a substitute for more encompassing three-dimensional structural modeling. Axial surface maps and cross sections from data can be incorporated into forward modeling strategies to ensure that model results approximate natural fold shapes. Axial surface mapping in areas of limited control can also help the interpreter

derive reasonable structural solutions that are consistent with the geology along trend.

Acknowledgments

This research was partially funded by Texaco, Inc., NEHRP Grant # 14-08-0001-G1699, the Southern California Earthquake Center, and Princeton University. Seismic reflection and well log data, essential to this work, were provided by Texaco USA, Chevron, Nippon Western US Co., Ltd., BP Exploration, Inc., Sun Operating LP, Halliburton Geophysical Services, Inc., Occidental Petroleum, and Western Geophysical.

REFERENCES

Dahlstrom, C. D. A., 1969, Balanced cross sections, Canadian Journal of Earth Sciences, v. 6, p. 743-757.

Medwedeff, D. A., 1985, Lateral terminations of fault-related folds, Geological Society of America Abstracts with Programs 17, p. 661.

Medwedeff, D. A., 1992, Geometry and kinematics of an active, laterally propagating wedge thrust, Wheeler Ridge, California, in *Structural Geology of Fold and Thrust Belts*, eds. Shankar Mitra and George Fisher, John Hopkins University Press. p. 3-28.

Mount, V. S., Suppe, J., and Hook, S. C., 1990, A forward modeling strategy for balanced cross sections, American Association of Petroleum Geologists Bulletin, v. 74, no. 5, p. 521-531.

Rich, J. L., 1934, Mechanics of low-angle overthrust faulting as illustrated by Cumberland Thrust Block, Virginia, Kentucky and Tennessee, American Association of Petroleum Geologists Bulletin, v. 18, p. 1684-1696.

Shaw, J. H., Bischke, R. E., and Suppe, J., 1992, Evaluation of the use of compressive growth structure in earthquake hazard assessment, U.S.G.S. Open-File Rept. 92-258.

Shaw, J. H., and Suppe, J., 1993, Active faulting and growth folding in the eastern Santa Barbara Channel, CA., submitted to the Geological Society of America Bulletin.

Suppe, J., 1983, Geometry and kinematics of fault-bend folding, American Journal of Science, v. 283, p. 684-721.

Suppe, J., Chou, G. T., and Hook, S. C., 1992, Rates of folding and faulting determined from growth strata, in *Thrust Tectonics*, ed. K. R. McKlay, Chapman and Hall, Publisher, p. 105-121.

Wilkerson, M. S., Medwedeff, D. A., and Marshak, S., 1991, Geometrical modeling of fault-related folds: a psuedo-three-dimensional approach, Journal of Structural Geology, vol. 13, no. 7, p. 801-812.

Woodward, N. B., Boyer, S. E., and Suppe, J., 1985, An outline of balanced cross-sections, University of Tennessee, Department of Geological Sciences, Studies in Geology, v. 11, 2nd ed., 170 pp.

CHAPTER 5

RELATIONSHIPS BETWEEN FOLDING AND FAULTING IN THE LOMA PRIETA EPICENTRAL ZONE: STRIKE-SLIP FAULT-BEND FOLDING

JOHN H. SHAW, RICHARD E. BISCHKE, & JOHN SUPPE
Department of Geological and Geophysical Sciences, Guyot Hall,
Princeton University, Princeton, New Jersey USA 08544-1003

to be published in
The Loma Prieta, California, Earthquake of October 17, 1989,
U. S. Geological Survey Professional Paper

ABSTRACT

We present balanced, kinematic models of strike-slip fault-bend folding that demonstrate how synclines in the 1989 Loma Prieta epicentral zone grow in transpression. Right-lateral motion along the San Andreas and Zayante faults in left-stepping restraining bends results in transpression and uplift of rocks adjacent to the fault bends. Uplift is produced by thrusting over non-planar fault surfaces which causes folding of the hanging-wall block. We model fold growth by kink-band migration with deformation of the over-riding block localized along active axial surfaces, which are pinned to subsurface fault bends. Applied to the epicentral zone, these balanced models yield predictions of the subsurface fault geometry. The orientation of the Glenwood syncline, which emanates in map view from the restraining bend in the San Andreas fault, suggests a steepening-upward subsurface bend in the underlying fault at a depth of about 8 km. The Scotts Valley syncline, which emanates in map view from a bend in the nearby Zayante fault, suggests a similar steepening-upward bend in the underlying fault at a depth of about 15 km.

We test our predictions of the subsurface fault geometry in the epicentral zone by examining hypocenters of the 1989 earthquake and its aftershocks. A contour map and series of cross sections of the fault surface, based on the aftershock locations, confirm that a steepening-upward subsurface bend in the San Andreas fault exists at 8 km depth. Furthermore, the geometry of the fault bend is in agreement with the fold orientation. This consistency between the fault geometry predicted by our models applied to surface data and the shape of the subsurface fault rupture outlined by the hypocenters confirms the relationship between fold and fault shape. These results suggest that fault-bend fold theory is a viable explanation for the origin of folds that lie adjacent to strike-slip faults.

We further test our models by comparing their predicted slip directions with slip vectors inferred from seismology and regional stress. Our predicted slip directions

are found to be consistent with both the slip vector of the main-shock and shear-stress directions resolved onto the various fault segments from regional stresses. Assuming that these favorable slip directions approximate long-term slip directions, the 12 mm/year slip rate on the San Andreas fault southeast of the rupture must increase to 15.2 mm/year onto the rupture surface. This increase in slip rate within restraining bends may explain why the Loma Prieta, and possibly other strike-slip earthquakes, originate at fault bends. This 15.2 mm/year slip rate resolves to a 11.6 mm/year strike-slip, 9.8 mm/year dip-slip, and 9.2 mm/year uplift rate above the inclined fault rupture. This uplift rate, once corrected for isostatic compensation, falls within the predicted range of uplift rates in the epicentral zone derived from dated marine terraces along the nearby Santa Cruz coastline. This suggests that the majority of slip on the adjacent San Andreas fault does transfer onto the inclined rupture surface, and if it is released in 1989 type events (2 ± 0.4 meters of slip), major earthquakes should recur every 132 ± 26 years. In addition, a study of syntectonic sediments deposited along the adjacent Zayante fault indicates large motions prior to the deposition of the Pliocene section. More recent strike-slip motion began during the middle Pliocene and appears to continue into the present.

INTRODUCTION

The Oct. 17, 1989 (Ms = 7.1) Loma Prieta earthquake occurred along a left-stepping bend of the San Andreas fault in the Santa Cruz Mountains of central California (fig. 1A). In analogy with the Transverse Ranges located to the north of the Los Angles Basin (Crowell, 1974a; 1974b), right-lateral motion on the San Andreas into a left-stepping restraining bend has resulted in transpression, uplift, and deformation in the hanging-wall rocks adjacent to the fault. In support of these conclusions, 1) earthquake focal-mechanism solutions of the Loma Prieta main-shock suggest a combination of reverse and strike-slip motion on a 70°±10° southwest-

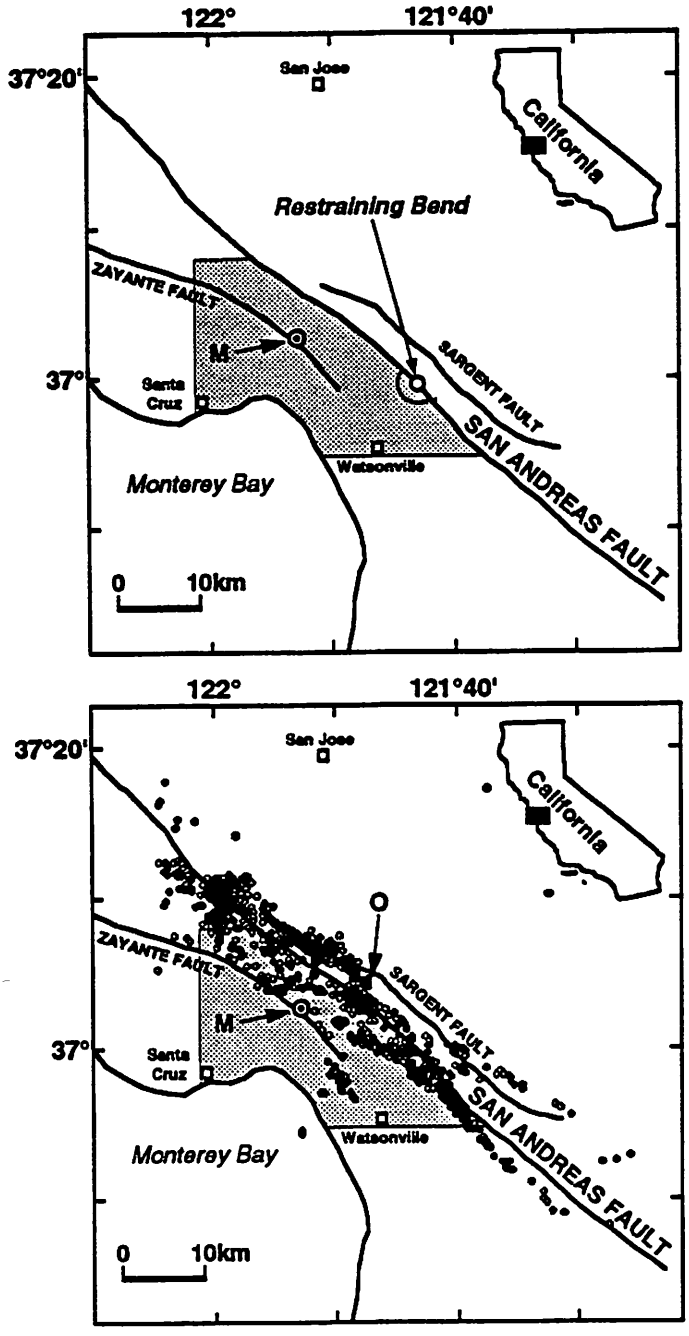

Figure 1A: (*Top*) Map of the San Andreas fault near the epicenter of the 1989 Ms=7.1 Loma Prieta earthquake (M). (*Bottom*) Epicenters of the main shock and selected aftershocks, with locations from Dietz and Ellsworth (1990). (O) highlights an offset in the seismicity between events along the San Andreas fault to the southeast and shallow events east of the fault to the northwest. Note that the epicenters lie along a left-stepping restraining bend in the San Andreas fault. The shaded pattern marks the area of figure 1B.

dipping fault (Oppenheimer, 1990), and 2) modeling of geodetic data by Lisowski et al. (1990) indicates that 1.6 m of right-lateral slip and 1.2 m of reverse-slip occurred during the earthquake.

In this paper we examine young geologic structure in the Loma Prieta epicentral zone which includes deformed Pliocene to Holocene syntectonic (growth) sediments adjacent to bends in the San Andreas and nearby Zayante faults (fig. 1B). Right-lateral motion along the faults into left-stepping bends in the epicentral zone generates synclines within recently deposited sediments. Material entering the restraining bends is thrust upward causing monoclinal folding of the hanging-wall block. Quaternary sediments and the upper Miocene and Pliocene Purisima Formation have been deformed into the Glenwood syncline as material has moved past a restraining bend in the San Andreas fault (fig. 1B). Another syncline which folds the Purisima Formation runs through Scotts Valley, formed as material passed through a similar restraining bend in the nearby Zayante fault.

We present balanced models of strike-slip fault-bend folding which show how these folds grow in transpression. Fold growth is modeled by kink-band migration with deformation of the over-riding block localized along axial surfaces pinned to subsurface fault bends. Application of these models to the folds in the Loma Prieta epicentral zone predicts subsurface fault geometry, including the orientation of fault surfaces and depth to subsurface fault bends. In order to test our predictions of subsurface fault geometry, we examine hypocenters of the 1989 Loma Prieta aftershock sequence. A contour map of the fault-surface rupture, a series of cross sections, and fault models confirm that a subsurface bend in the San Andreas fault system exists consistent with that predicted by the location and orientation of the Glenwood syncline. Subsurface geometry of the Zayante fault is also inferred from the location and orientation of the Scotts Valley syncline and other available data.

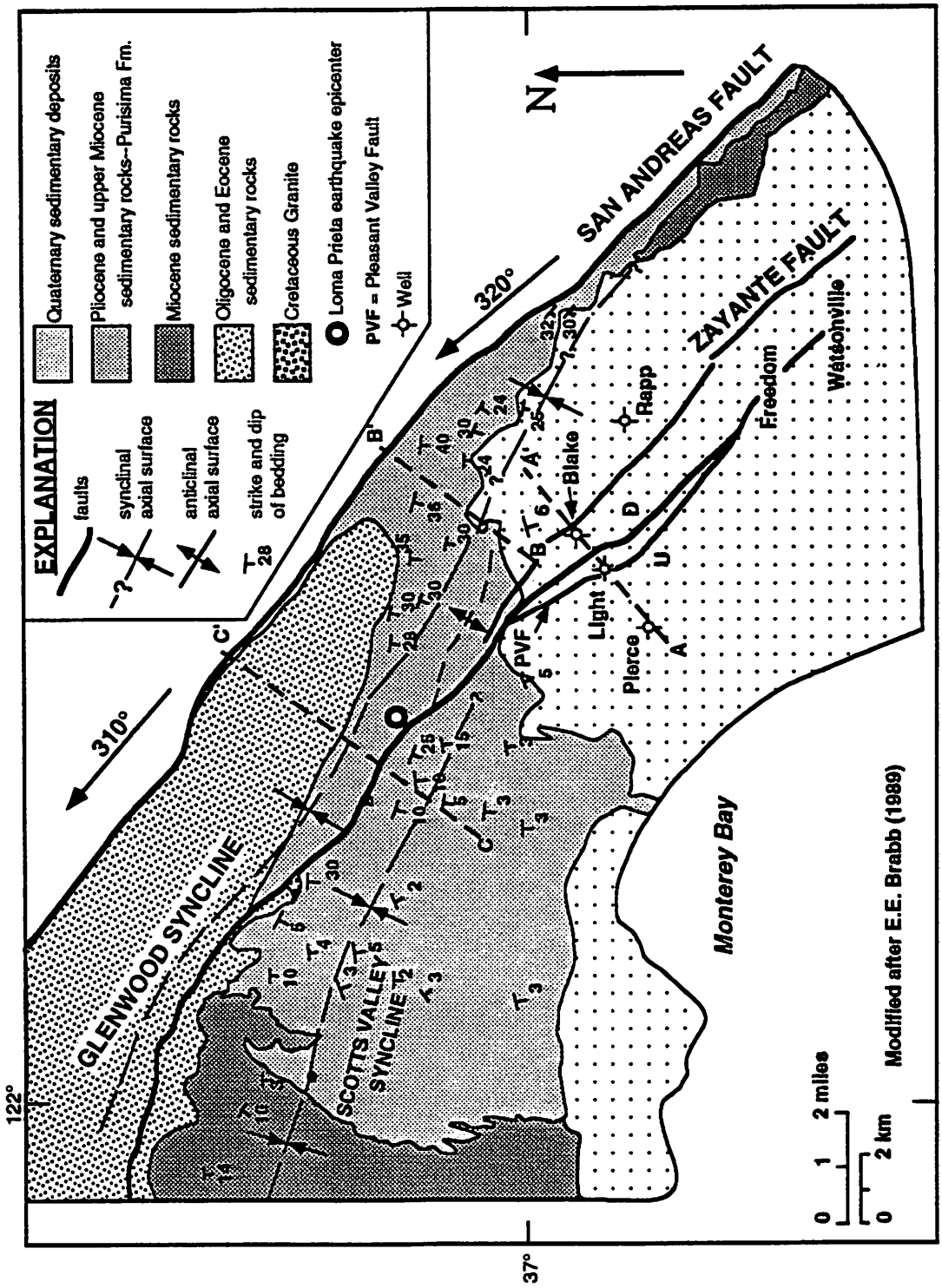

Figure 1B: A geologic map of the 1989 Loma Prieta epicentral zone modified from E.E. Brabb (1985) showing synclinal axial surfaces that fold Pliocene and younger strata emanating from restraining bends in the San Andreas and Zayante faults. A minor right-stepping bend marks the left-stepping change in trend of the San Andreas from 320° in the southeast to 310° in the northwest. Axial surfaces are queried (?) where inferred or less certain.

Surface geology and aftershocks of the Loma Prieta earthquake suggest that the epicentral zone is characterized not by a single active throughgoing fault, but by active segments of the San Andreas, Zayante, and Sargent(?) faults which compose the San Andreas fault system. In order to test our model of the subsurface fault system, the slip direction of the Ms = 7.1 main-shock (Oppenheimer, 1990) and slip directions inferred from our models are compared with shear-stress directions resolved onto the various fault segments from components of the regional stress tensors of Michael et al. (1990). In addition, these slip directions, the subsurface fault geometry, and long-term slip rates on the San Andreas fault southeast of the rupture are used to calculate Pliocene and Quaternary uplift rates above the San Andreas and Loma Prieta faults. The results are compared with predicted uplift rates in the epicentral zone derived by several authors from marine terrace elevations along the Santa Cruz coastline.

In order to constrain past movements on the Zayante fault, which did not rupture in the Loma Prieta earthquake, we examine electric well-log data across the fault. We apply a new subsurface mapping technique to examine syntectonic (growth) strata, and demonstrate that more recent motions initiated on the Zayante fault during the late Pliocene, have continued into the Quaternary and perhaps into the present day.

FOLDING AND FAULTING IN THE EPICENTRAL ZONE

Surface Relationships Between Folds and Faults

Both the San Andreas and Zayante faults have major left-stepping, or restraining bends in the vicinity of the Loma Prieta epicentral zone. The surface trace of the San Andreas fault changes trend from 320° to 310°, from southeast to northwest in the study area (figs. 1A and 1B; a minor right-stepping bend marks this transition). The Glenwood syncline emanates in map view from this left-stepping restraining bend in the right-lateral San Andreas fault. The surface trace of the axial surface of the

Glenwood syncline diverges from the fault trace reaching a maximum distance of roughly 4 km and maintains this distance as it runs parallel to the San Andreas fault to the northwest for over 17 km. The axial surface separates a gently southwest-dipping panel to the south from a more steeply southwest-dipping panel to the north, as shown by bedding dips at the surface (Brabb, 1989) and well-log correlation data (Muir, 1972). At the surface, the Glenwood syncline folds semi-consolidated Quaternary sediments and parts of the upper Miocene and Pliocene Purisima Formation.

The Zayante fault also contains a restraining bend in the epicentral zone due west of the similar bend in the San Andreas fault (fig. 1B). Southeast of the bend, the most active branch of the Zayante fault trends 320° through Pleasant Valley and the Freedom-Watsonville areas, as determined by offsets of strata recorded between the Pierce, Light, and Blake wells, (presented in a later section). Northwest of the bend the surface trace of the Zayante fault trends at approximately 310° for about 13.5 km, sub-parallel to the adjacent San Andreas fault. Clark and Rietman (1973) have interpreted the Zayante fault to be a large, near-vertical fault active during the Oligocene. More recent Pliocene and Quaternary motion on the Zayante fault offsets the upper Miocene and Pliocene Purisima Formation (Clark, 1981). In addition, recent motion is indicated by deformed Quaternary horizons and a fault scarp of probable Holocene age (Hall et al., 1974; Clark et al., 1984). We suggest that Pliocene and Quaternary motions are strike-slip in the epicentral zone, causing thrusting and uplift in a restraining bend of the Zayante fault (fig. 1B). Consistent with this interpretation, 1) Clark et al. (1984) report oblique-reverse, right-lateral offsets across the fault; and 2) the surface trace of the near-vertical Zayante fault south of the bend is parallel to, and merges with, the San Andreas fault along the Vergeles fault (Clark, 1981).

The Scotts Valley syncline emanates in map view from the left-stepping bend in the Zayante fault, similar to the relationship between the nearby Glenwood syncline and the San Andreas fault (fig. 1B). The axial surface trace of the Scotts Valley syncline runs 2 - 4 km southwest of and sub-parallel to the Zayante fault for 8 km northwest of the fault bend. Farther to the northwest the distance between the axial surface and fault trace decreases as the Zayante fault trace curves sharply to trend roughly due west (Clark, 1981). The synclinal axial surface separates a near-horizontal southern limb from a gently south-dipping limb to the north.

Eocene and Oligocene rocks adjacent to the San Andreas and Zayante faults are more strongly folded. The age and intense folding of these rocks suggests that they may have been deformed prior to the development of the modern San Andreas fault system that formed in the late Miocene, associated with the opening of the Gulf of California (Curry and Moore, 1984). These rocks also may have been folded while passing through other restraining bends in the modern San Andreas and Zayante faults southeast of the study region. In order to model deformation solely associated with the restraining bends in the Loma Prieta epicentral zone, we concentrate on the more recent Pliocene and Quaternary growth sediments deposited while the faults were active. These younger strata are less likely to have been intensely deformed prior to entering the restraining bends, which is consistent with areas of near-horizontal strata south of the axial surfaces. Locally steeper dips very close to the fault traces (Brabb, 1989) are attributed to minor restraining bends or to other local fault zone processes.

Three-Dimensional Balanced Models of Strike-Slip Folding

In figure 2 we present balanced models of strike-slip deformation that show how folds grow in transpression. Development of the models has been governed by the two basic assumptions of Suppe's (1983) fault-bend fold theory; 1) at depth, rocks are

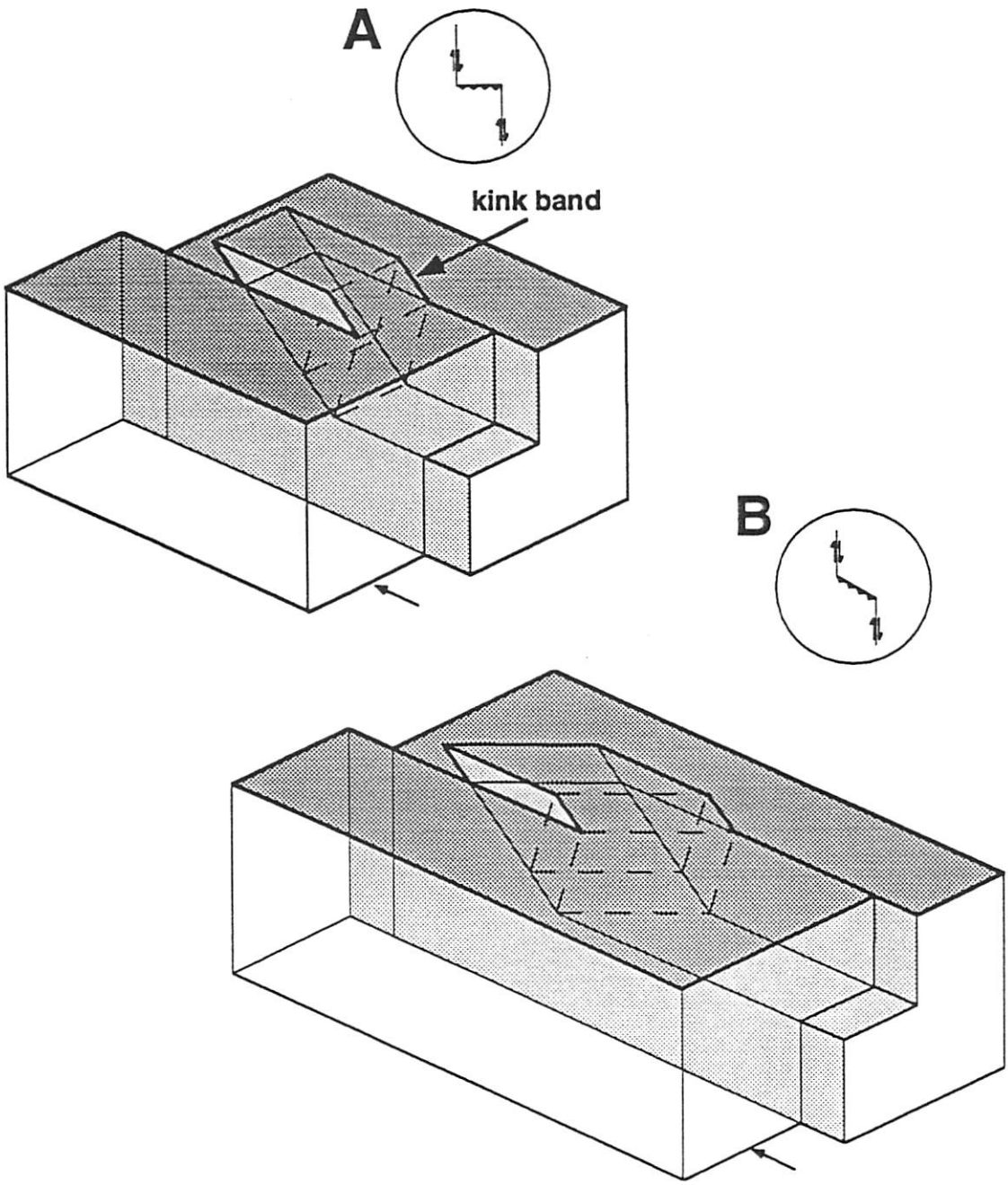

Figure 2 A,B: Balanced 3-dimensional models of fold growth adjacent to restraining bends in right-lateral strike-slip fault systems. All of the models **A-D** show uplift and fold growth by kink-band migration above a thrust or oblique-slip fault that connects vertical strike-slip faults. Mechanical bedding is represented by the darkened surface layer. Model **A** contains a horizontal detachment which ramps upward and strikes normal to the adjacent vertical faults. The width of the kink band equals fault slip. Model **B** contains an oblique-slip right-lateral thrust ramp which strikes oblique to the trend of the strike-slip faults. The kink-band width represents only the dip-slip on the underlying ramp. (*continued on page next page*)

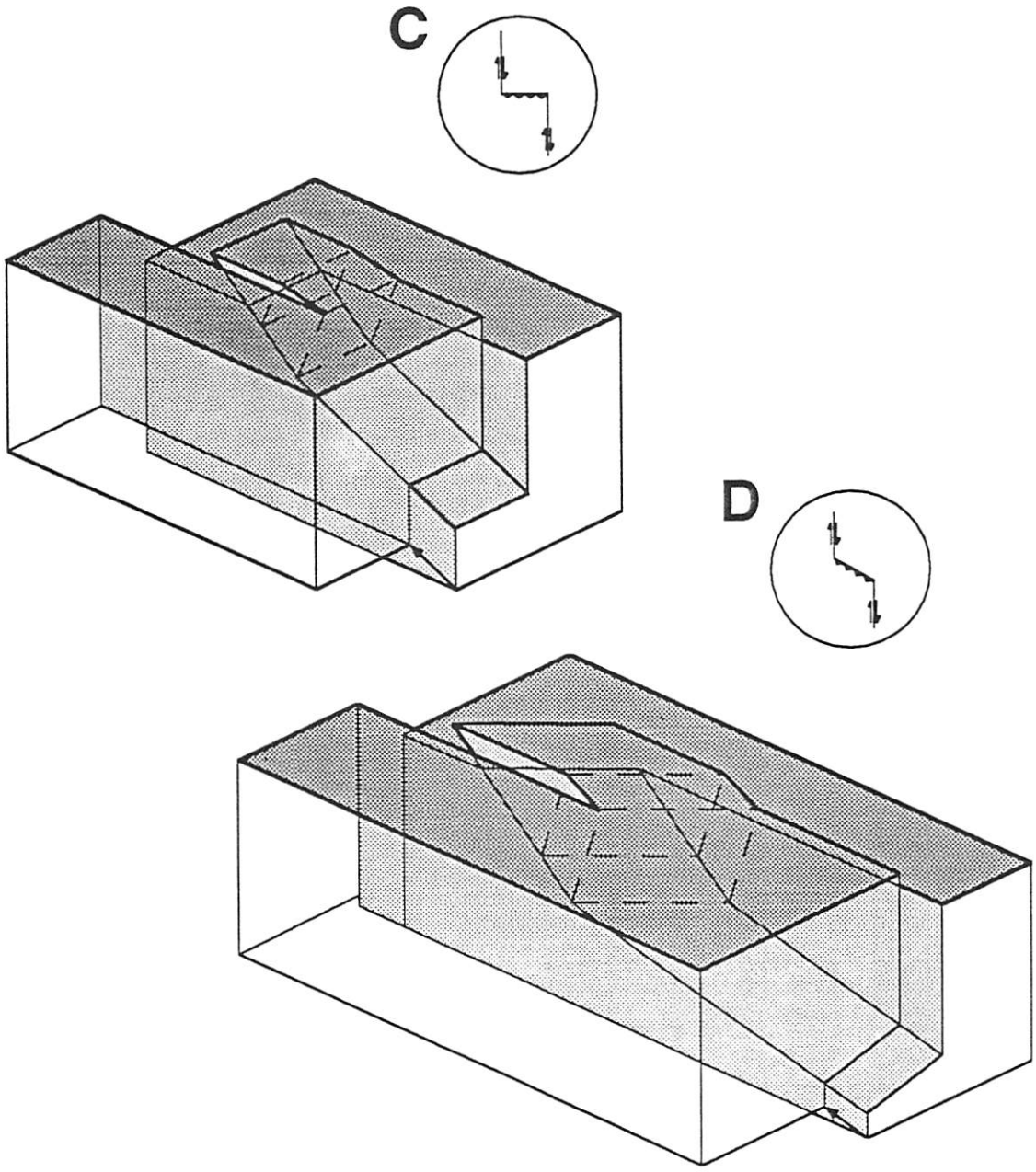

Figure 2 C,D: Model **C** contains a dipping thrust with a steepening-upward ramp that strikes normal to the adjacent vertical faults. The dip of the thrust produces relative uplift of the hanging-wall block with respect to the foot-wall, and the kink-band width above the ramp is less than slip on the underlying fault. Model **D** contains a dipping oblique-slip, right-lateral thrust with a steepening-upward ramp that strikes oblique to the adjacent vertical fault. Only the dip-slip component of motion on the connecting faults produces uplift and kink-band growth.

too weak to support large voids opened by movement of rigid blocks over non-planar fault surfaces, and 2) rock volume is conserved during deformation. As focal-mechanism and ground-motion studies of the 1989 Loma Prieta earthquake have demonstrated, movement of material into a left-stepping bend in the San Andreas fault system has resulted in thrusting. This thrust component of motion results in folding of the hanging-wall block as it moves over bends in the underlying fault. Rich (1934) and Suppe (1983) demonstrated that rigid-block translation over non-planar fault surfaces generates unreasonable "overlap" or subsurface voids in the underlying rock between fault surfaces (fig. 3). At depth, these voids cannot be supported assuming reasonable rock strengths. As detailed in the theories of fault-bend folding (Suppe, 1983), collapse of these voids and removal of "overlap" may be accommodated by deformation of the over-riding block localized along active axial surfaces pinned to subsurface fault bends (fig. 3). Folds develop as material shears through active axial surfaces and grow by kink-band migration during progressive fault slip. Quantitative relationships between fold shape and fault shape are those of fault-bend folding derived by Suppe (1983). In cases of oblique-slip, which may arise in transpression, the limb lengths or kink-band widths of the folds, measured normal to the active and inactive axial surface pairs, are minimum estimates of the dip-slip on the underlying faults. Additional constraints on the direction of slip and on subsurface fault geometry are required to determine the total slip vector.

The four models (A, B, C, D) presented in figure 2 all represent folds developed within restraining bends along left-stepping, right-lateral fault systems. The progression of models, presented in order of increasing complexity, is used to show how specific changes in fault geometry affect fold growth and fault slip. In this and following sections, aspects of these simplified models will be tested and applied to the San Andreas and Zayante fault systems. All models consist of vertical, dominantly strike-slip faults connected by dipping thrust or oblique-slip faults.

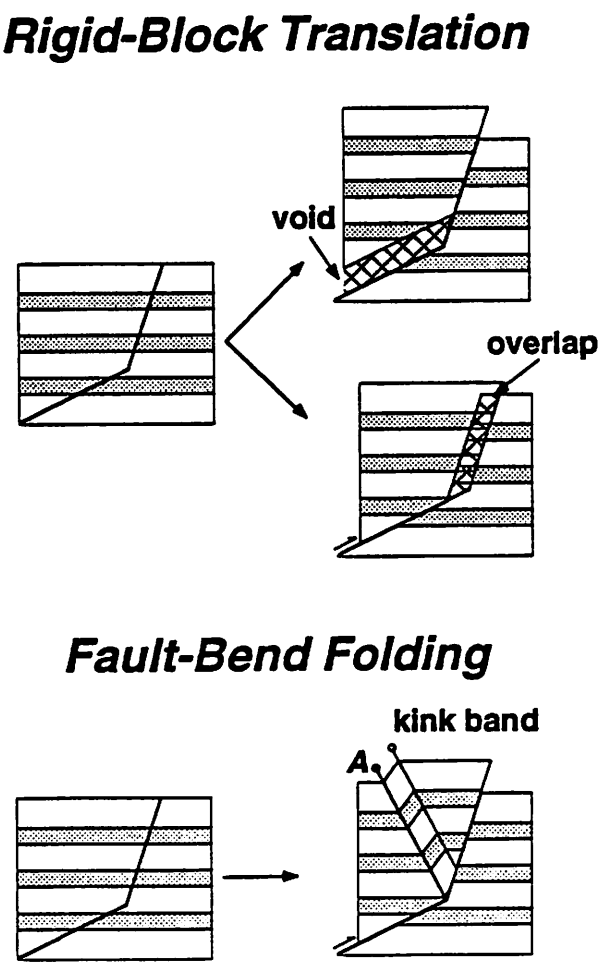

Figure 3: Balanced models which demonstrate that rigid-block translation over non-planar fault surfaces produces unreasonable "overlap" or subsurface voids between fault surfaces (crossed pattern). Folding of the hanging-wall block, localized along active axial surfaces (*A*) pinned to fault bends, accommodates fault slip without producing "overlap" or voids.

Thrusting results in uplift of material above the connecting fault plane between the vertical faults. Uplift is accomplished with fold growth by kink-band migration, with active axial surfaces pinned to subsurface bends in the underlying thrust or oblique-slip faults. In these models, and in application to the Loma Prieta epicentral zone, axial surfaces bisect mechanical bedding units and bed thickness and volume are conserved. These balanced models therefore represent geometrically and kinematically reasonable solutions to fold growth in transpression.

In model A (fig. 2) the connecting thrust ramps to the surface from a horizontal detachment at depth. The ramp strikes normal to the strike of the adjoining vertical faults. The orientation of mechanical bedding is represented in all of the models by the dark surface layer. The horizontal detachment fault at depth is bedding parallel and contains a slip vector parallel and equal in magnitude and direction to that on the adjoining strike-slip faults. During progressive fault slip, a dipping kink-band forms above the ramp with its inclined surface parallel to the underlying thrust ramp. As the surface (bedding) is parallel to the underlying fault plane, the kink-band width, measured normal to the axial surfaces along bedding, is equal to fault slip. Model B in figure 2 differs from model A in that the strike of the connecting fault ramp is not perpendicular to the strike of the adjoining vertical faults. The bedding and inclined surface of the fold is again parallel to the underlying fault ramp, although the kink-band width represents only the dip-slip component of motion on the oblique-slip fault ramp. Thus, for a given amount of slip entering a restraining bend, fold-limb width and uplift decrease as the strike of the connecting ramp approaches the strike of the adjacent vertical faults. In cases where the subsurface fault geometry is known and slip direction can be inferred, the magnitude of fault slip can be calculated from kink-band width by resolving the vector triangle on the fault surface.

In model C (fig. 2) the horizontal detachment of models A and B is replaced by an inclined connecting thrust that has a steepening-upward bend as it approaches the

surface. The slip vector on the deeper segment of the thrust is again equal to the slip on the oblique-slip vertical faults. However, unlike the previous models, this inclined slip vector produces uplift of the hanging-wall block relative to the foot-wall above the deeper thrust fault segment. Mechanical bedding, represented by the darkened surface in the model, is not parallel to the lower thrust fault segment, therefore fault slip must increase slightly onto the steepening-upward thrust ramp (Suppe, 1983). Moreover, bedding is not parallel to the shallower thrust segment as the inclined surface of the fold limb dips less than the underlying thrust ramp. As only the dip-slip component of motion generates the folds in these models, the relationships between fold and fault shape are those derived for fault-bend folding by Suppe (1983). In cases where the dip of the fold limb is less than the dip of the underlying fault, the kink-band or fold-limb width represents a minimum estimate of dip-slip on the underlying fault. In cases where subsurface fault geometry is known, fault slip can be calculated. However, in cases where fault geometry is poorly constrained, fold-limb width provides a reasonable estimate often within 20% of fault dip-slip (Suppe et al., 1992).

Model D (fig. 2) combines aspects of models B and C and is presented as a simplified representation of fold growth in the epicentral zone along the San Andreas and Zayante faults. As in model C, the dipping lower segment of the thrust fault ramps upward toward the surface. The strikes of the connecting thrusts however are not perpendicular to the adjacent vertical faults, similar to model B. The dip-slip component of motion on the lower segment of the oblique thrust produces uplift of the hanging-wall block relative to the foot-wall. Since bedding is not parallel to the lower connecting fault segment, slip slightly increases in magnitude onto the thrust ramp. Also, the inclined surface of the kink-band and bedding, which develops as material shears through the active axial surface, has a shallower dip than the underlying ramp. Consequently, the kink-band width in this model represents only a minimum estimate

of the dip-slip component of motion on the underlying oblique-thrust ramp. As in the previous models, in cases where the subsurface fault geometry is known and the slip direction can be inferred, fault-slip magnitude can be calculated.

Predicting Subsurface Fault Geometry

Application of the relationships between folds and faults observed in the models (fig. 2) to natural transpressive environments allows detailed predictions of subsurface fault geometry along strike-slip fault systems. Axial surfaces that emanate from bends in strike-slip faults can be projected to depth if their orientations are known or are assumed to bisect adjacent fold limbs. The intersections at depth of faults and active axial surfaces predict the positions of subsurface fault bends. In addition, the acute angle between 1) bedding and the axial surface (γ), and 2) bedding and the upper fault segment (β), can be used to predict the change in dip of the fault across the bend (ϕ) and the lower hanging-wall cutoff (θ) using the fault-bend fold equations (fig. 4; see Suppe, 1983).

Applying these models to the epicentral zone, the location of the Glenwood synclinal axial surface, which emanates in map view from the restraining bend in the San Andreas fault (fig. 1B), predicts a steepening-upward subsurface bend in the underlying fault. The 72°E dip of the axial surface, estimated from the dip of adjacent strata mapped by Brabb (1989) and others, predicts an intersection of the fold hinge and the near-vertical San Andreas fault (dip > 75° from surface geology) between 7 to 12 km depth (fig. 5). This depth estimate will be refined and the change in dip across the fault bend will be determined in the following section when the dip of the San Andreas fault is more accurately determined. The Scotts Valley synclinal axial surface, which in map view emanates from the restraining bend in the Zayante fault (fig. 1B), suggests a similar steepening-upward subsurface bend in the underlying fault. The intersection of the 83°E-dipping axial surface and the vertical Zayante fault

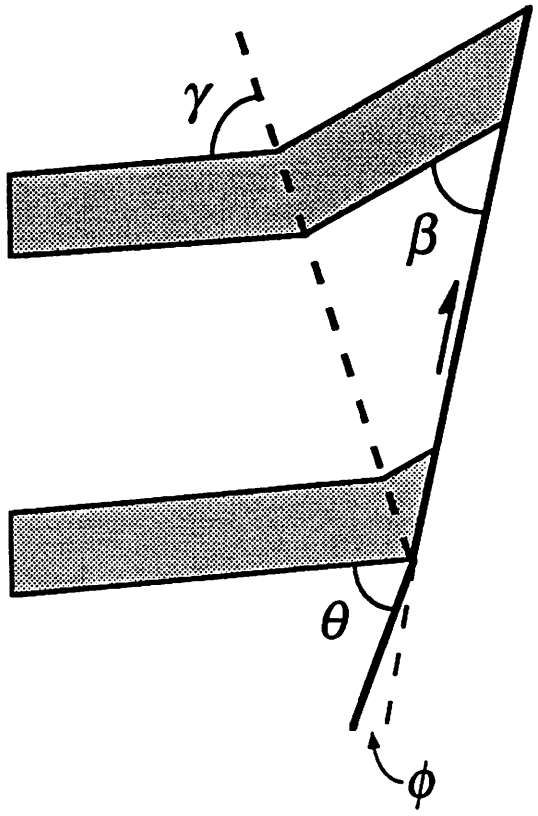

$$\phi = \tan^{-1}\left\{\frac{-\sin(\gamma-\theta)\,[\sin(2\gamma-\theta)-\sin\theta]}{\cos(\gamma-\theta)\,[\sin(2\gamma-\theta)-\sin\theta]-\sin\gamma}\right\}$$

$$\beta = \theta - \phi + (180 - 2\gamma)$$

Suppe (1983)

Figure 4: A synclinal axial surface emanates from a steepening-upward bend in the underlying fault. Fold shape is related to fault shape by the fault-bend fold equations of Suppe (1983). Note that the axial surface bisects fold limbs, conserving layer thickness.

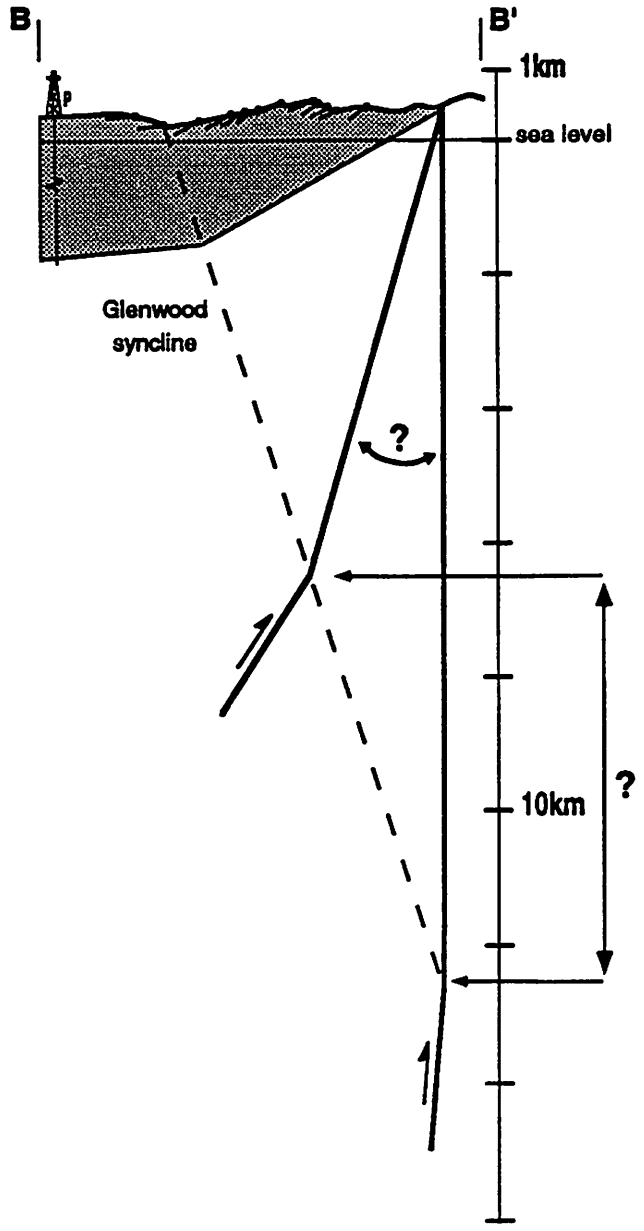

Figure 5: The preliminary cross section (*B-B'*) across the Glenwood syncline and San Andreas fault (located in figure 1B). The orientation of the synclinal axial surface, which bisects bedding, predicts a steepening-upward subsurface bend beneath the steeply dipping San Andreas fault between a depth of 7 and 12 km. The true dip of the upper segment of the San Andreas fault, to be determined from hypocentral locations of the Loma Prieta earthquake, will further constrain the depth to the fault bend. (*P*) denotes projected well Blake.

should occur at roughly 15 km depth. Alternative subsurface geometries for the Zayante fault are discussed in a later section.

Subsurface Fault Geometry Inferred from Loma Prieta Seismicity

As seismicity can provide important constraints on fault geometry, hypocenters of the aftershocks of the 1989 Ms = 7.1 Loma Prieta earthquake (fig. 1A) described by Dietz and Ellsworth (1990) and provided by the U. S. Geological Survey, were examined in order to test our predictions of the subsurface fault geometry in the epicentral zone. The hypocenter sequence that we use consists of the 1173 best constrained aftershocks (from a total of 3750) processed by October 1989. The hypocenters were located by Dietz and Ellsworth using two one-dimensional velocity models separated by the San Andreas fault. Horizontal standard errors <0.5 km and vertical standard errors <1.0 km are assigned to the selected hypocenters, although relative locations are thought to be more accurate, (average relative epicentral error of $\pm$0.3 km, average relative vertical error of $\pm$ 0.6 km).

Fault-surface contour maps generated from subsurface data have proven to be an effective first step toward developing reasonable structural interpretations of faulted terrains (Tearpock and Bischke, 1991). In order to create a contoured fault-surface map of the rupture area from the seismicity in the epicentral zone, hypocenters were divided into horizontal slices corresponding to 2-km-depth intervals. Contour lines through the fault-surface rupture outlined by the hypocenters were drawn free-hand for each horizontal section. Typically, this technique has proven to yield the most accurate representation of subsurface fault geometry (Tearpock and Bischke, 1991). Contour lines were assigned depth values equal to the depth of the center of their corresponding horizontal sections, and were projected vertically to the surface to form a contour map of the fault surface (fig. 6). Vertical cross sections were then

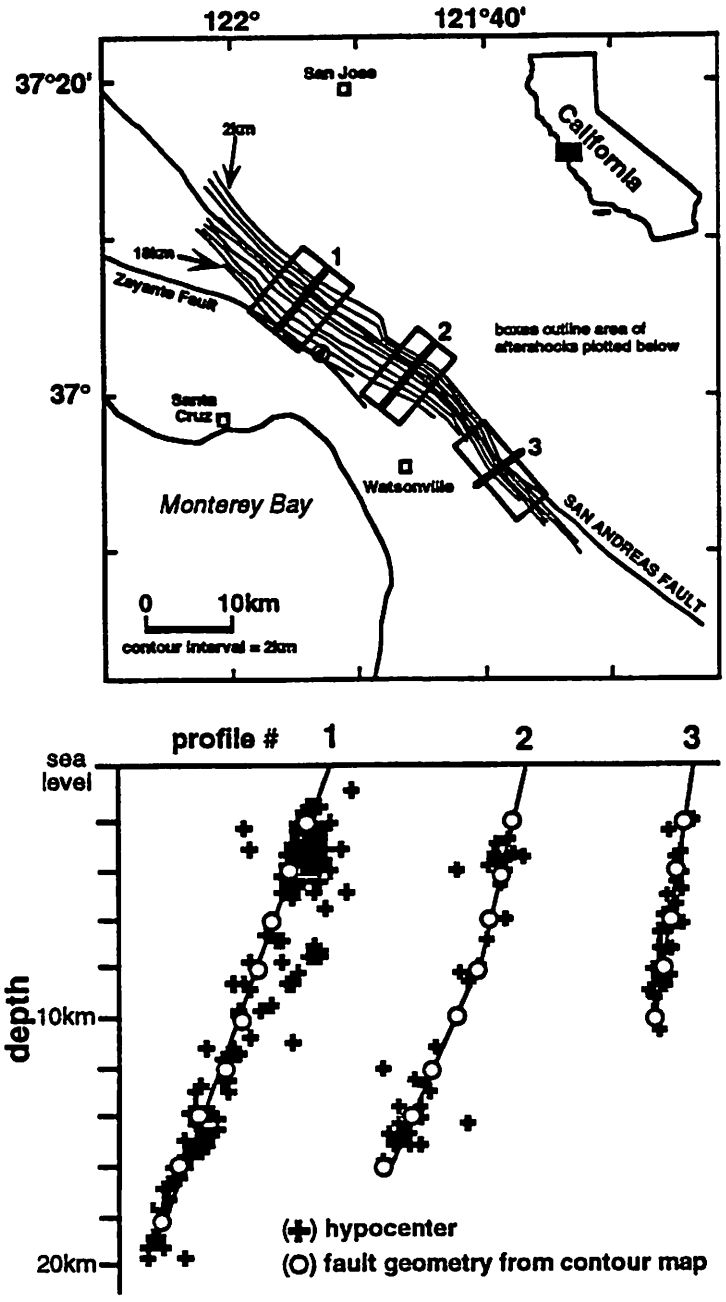

Figure 6: A contour map of the 1989 Loma Prieta rupture derived from hypocentral location reported by Dietz and Ellsworth (1990). The change in trend of the contours from southeast to northwest highlights the restraining bend in the fault system. A series of cross sections across the map (*1-3*), about which hypocenters are plotted, show dipping fault segments and locate a steepening-upward fault bend in the central part of the rupture, (section 2).

constructed through the contour map to highlight fault bends and to show changes in the subsurface fault geometry along strike.

Changes in the relative spacing and trends of contour lines in the fault-surface map indicate that the Loma Prieta rupture did not occur on a single planar fault, but on a complex system composed of multiple fault segments. The subsurface fault geometry outlined by the contour map and cross sections (fig. 6) is represented by the models in figures 7A and 7B. The contour map and fault section 3 of figure 6 suggest that the southeastern part of the hypocenters define a steeply dipping plane beneath the surface trace of the San Andreas fault, consistent with the observation of Dietz and Ellsworth (1990). This segment of the San Andreas strikes 320° and dips 82° to the west (fig. 7A, fault segment #1). Focal-mechanism solutions of selected events from this fault segment, which lies to the southeast of the restraining bend, show large components of right-lateral slip (Oppenheimer, 1990).

The main-shock and aftershocks in the deep central and northwestern parts of the rupture outline a different planar fault segment which strikes 310° and dips 70° to the southwest (fig. 7A, fault segment #2). The orientation of this fault is coincident with the preferred nodal plane of focal-mechanism solutions of the main-shock reported by Oppenheimer (1990). The change in strike between this northwestern fault segment and the fault rupture to the south forms the restraining bend that caused the transpression and thrusting in the Loma Prieta seismicity.

Shallow hypocenters from the northwestern edge of the aftershocks suggest that the Loma Prieta fault rupture in this area projects to the east of the surface trace of the San Andreas fault (figs. 1A and 6, cross section #1). It appears that the northwestern extension of the 78°W-dipping San Andreas fault (fig. 7A, segment #3) did not rupture during the Loma Prieta event. The 70°W-dipping fault rupture is therefore addressed in the following discussion as the Loma Prieta fault segment, a component of the San Andreas fault system. Schwartz et al. (1990) suggest that

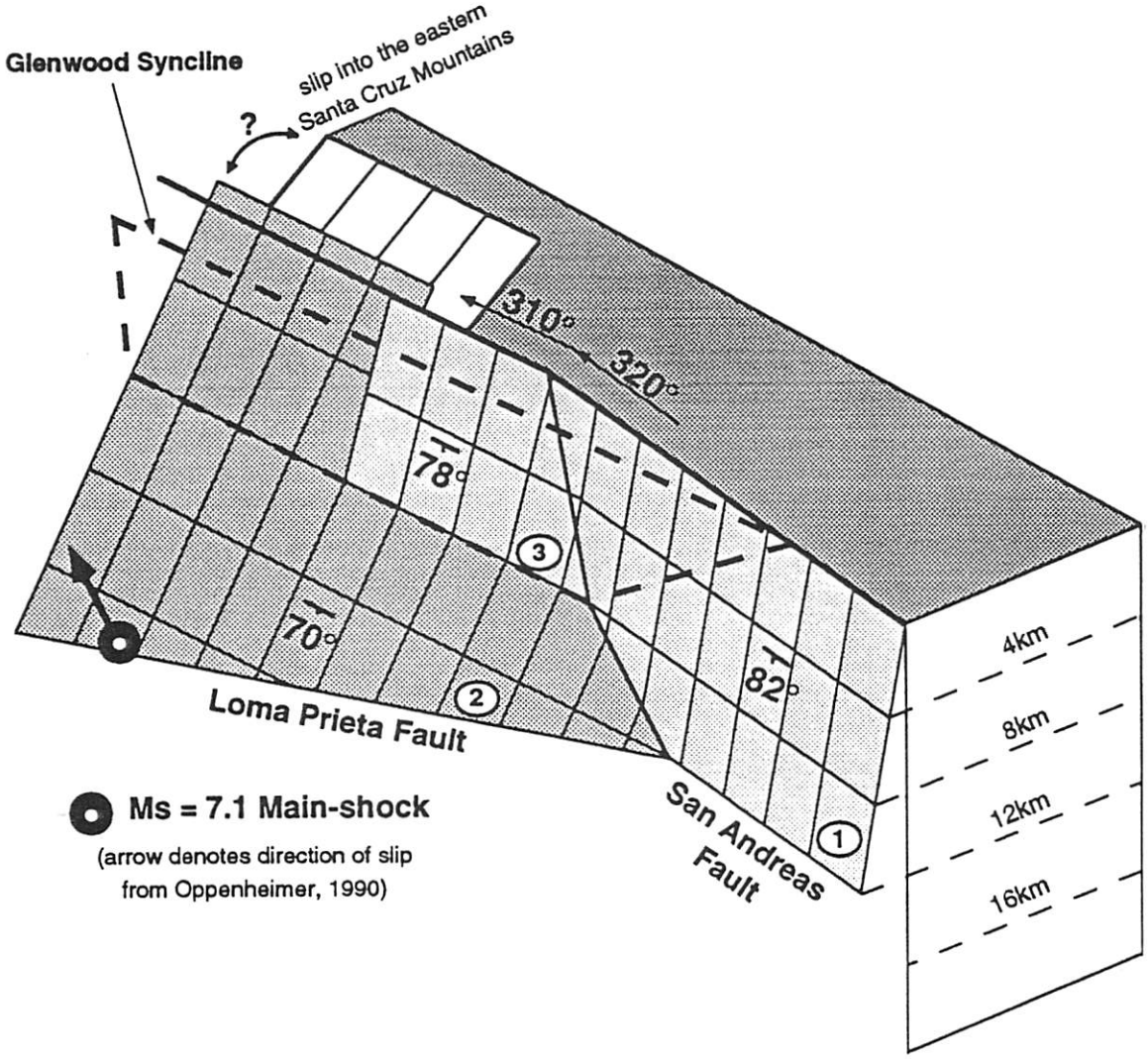

Figure 7A: A subsurface fault model of the epicentral zone derived from the contour map and cross sections of the fault surface rupture presented in figure 6. The fault system is composed of multiple fault segments that include: 1) the San Andreas fault southeast of the restraining bend, 2) the west-dipping Loma Prieta fault (completely buried) which corresponds to the main-shock preferred nodal plane of Oppenheimer (1990), and 3) a segment of the San Andreas fault northwest of the restraining bend which forms an active steepening-upward bend above the underlying Loma Prieta fault. The Glenwood syncline emanates at depth from this fault bend. To the northwest of the rupture, above the Loma Prieta fault segment, long-term slip may transfer onto shallower dipping thrusts in the eastern Santa Cruz Mountains.

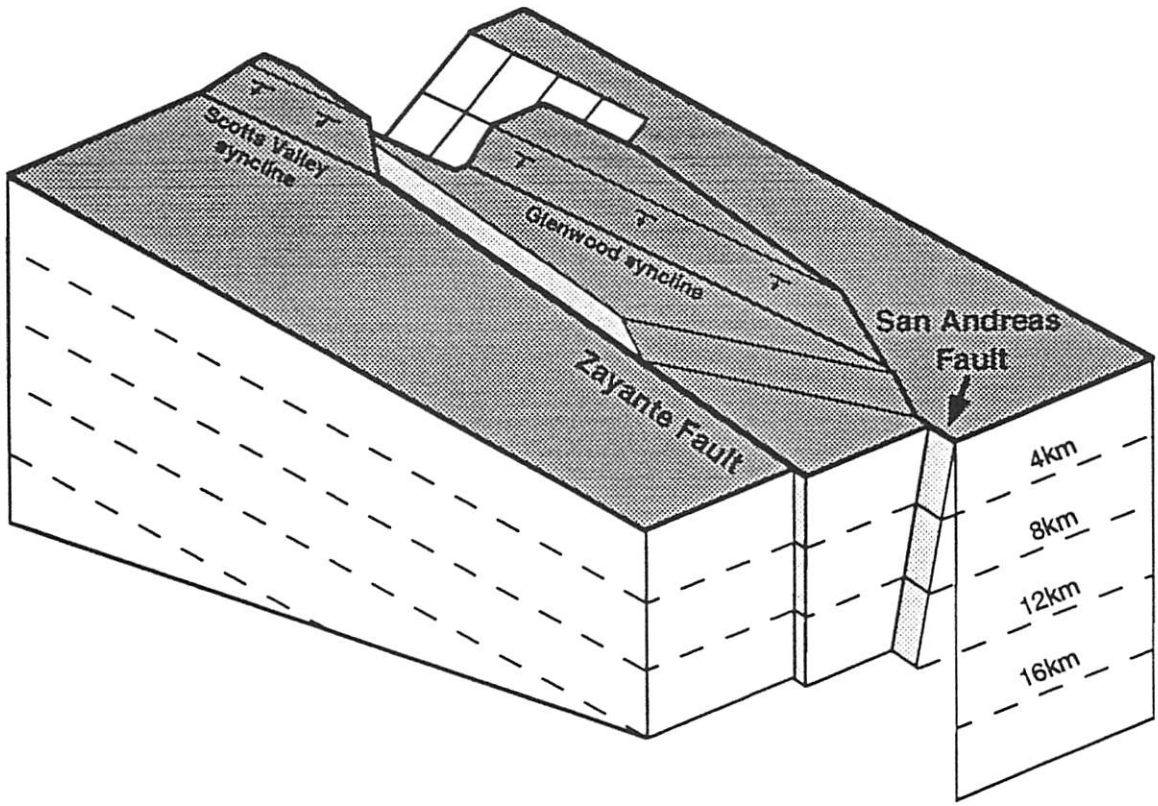

Figure 7B: A balanced 3-dimensional model of hangingwall deformation above the fault system presented in figure 7A. Thrusting produces growth of the Glenwood syncline by kink-band migration with shearing of materials through the axial surface pinned to an underlying subsurface fault bend. Formation of the Scotts Valley syncline is attributed to a similar steepening-upward bend beneath the Zayante fault.

shallow slip may have transferred from what we term the Loma Prieta fault segment to faults in the Sargent-Berrocal fault zone to the east of the San Andreas fault (fig. 1A). Seeber and Armbruster (1990) report that seismicity in the 20 years prior to the Loma Prieta rupture and faults mapped to the east of the San Andreas fault (McLaughlin et al., 1988), indicate that long-term slip on the Loma Prieta fault may in part be transferred onto a series of shallow-dipping thrusts beneath the eastern Santa Cruz Mountains (fig. 7A).

An abrupt change in the fault rupture outlined by the aftershocks occurs roughly due east of the main-shock epicenter (figs. 1A and 6, cross section #2). The break represents a transfer from shallow rupture to the northwest on the Loma Prieta fault (and associated shallow thrusts east of the San Andreas fault), to rupture in the southeast primarily beneath the surface trace of the San Andreas fault. Southeast of the break, in the central part of the hypocenters just to the north of the restraining bend, the fault rupture steepens upward from the Loma Prieta fault. The seismicity defines a 78° west-dipping fault segment (fig. 6, cross section #2, and fig. 7A, fault segment #3), beneath the surface trace of the San Andreas fault. This segment, thought to be part of the San Andreas fault, and the underlying Loma Prieta fault form an active flat to ramp system, or steepening-upward fault bend, which slipped during the Loma Prieta event. This inferred fault geometry is similar to that suggested by Lietz and Ellsworth (1990). These authors also report a concave-upward shape of the Loma Prieta rupture surface in the vicinity of the restraining bend.

As discussed in the previous section (fig. 3), dip-slip across this fault bend, formed by segments of the Loma Prieta (segment #2) and San Andreas (segment #3; fig. 7A) faults, must result in deformation of the over-riding block. As represented in the models in figure 2, deformation should be localized along active axial surfaces pinned to subsurface fault bends. Similar to the models of figure 2, movement of the

hanging-wall block over the fault geometry presented in figure 7A results in fold growth above the subsurface fault bends (fig. 7B).

Using the balanced models of figure 2 applied to the epicentral zone, the location and orientation of the Glenwood syncline predicts an underlying bend between 7 and 12 km in the San Andreas-Loma Prieta fault system (fig. 5). The seismicity, contour maps, and cross section 2 in figure 6 confirm that a steepening-upward bend exists at 8 km depth. The geologic cross section presented in figure 8 combines surface geology and subsurface fault data provided by the seismicity. The location of the steepening-upward fault bend occurs at the intersection of the projected Glenwood syncline and the steeply dipping San Andreas fault. Using fault-bend folding theory (Suppe, 1983) (fig. 4), the 47°-cutoff angle (β) between the fault and adjacent strata, and the 77° angle between strata and the Glenwood syncline (γ), predicts an 8° change in the fault dip across the bend (ϕ). This value corresponds with the 78° to 70° change in fault dip across the bend inferred from the seismicity (fig. 8).

It appears likely that during past slip on the fault system and growth of the Glenwood syncline, the inactive axial surface, or other end of the kink-band, has been uplifted and eroded. In addition, the rupture of the steepening-upward fault bend only in the central section of the aftershocks (fig. 6) suggests that the Glenwood syncline grew only in this region during the Loma Prieta event. Past ruptures that involved slip on the steeply dipping San Andreas fault northwest of the restraining bend, which did not rupture in the 1989 earthquake, as well as the Loma Prieta fault segment, are most likely responsible for the northwest extension of recent deformation along the syncline.

The consistent fault geometry inferred from the applied balanced models, surface geology, and the seismicity confirms the predicted relationships between subsurface fault bends and folds observed at the surface. This suggests that fault-bend folding is indeed a folding mechanism of transpressional environments. Furthermore, fault-

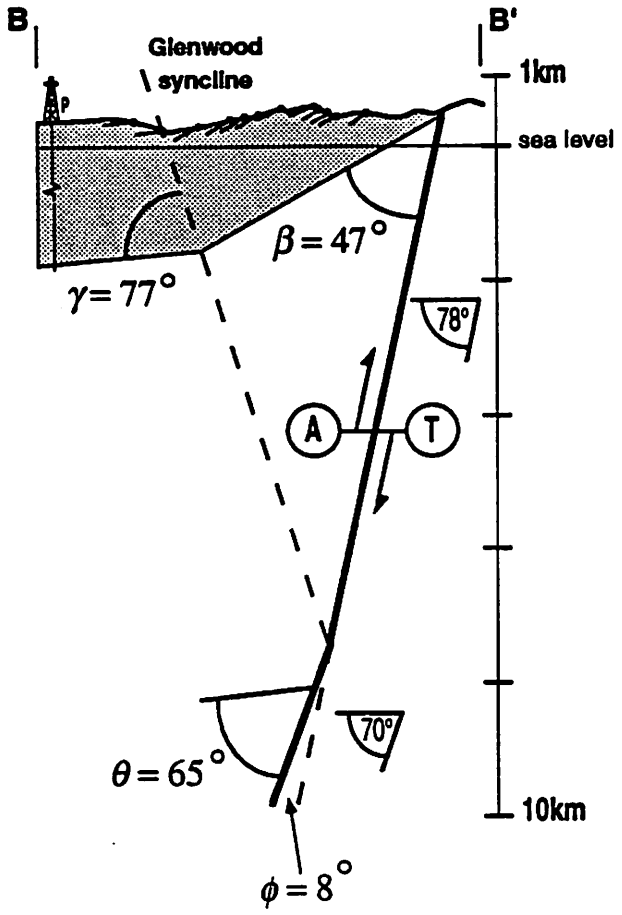

Figure 8: The geologic cross section (B-B') across the Glenwood syncline and San Andreas and Loma Prieta faults segments (located in figure 1B). The syncline emanates from the steepening-upward bend in the fault surfaces outlined by hypocentral locations (see fig. 6). Using the theory of fault-bend folding (Suppe 1983), the angle between bedding and the axial surface (γ) and the upper hanging-wall cutoff (β) are consistent with the 8° fault-dip change (ϕ) and the lower hanging-wall cutoff (θ) determined from the seismicity (see fig. 4). (P) denoted projected well Blake. Lateral motion (A) = away; (T) = toward.

bend fold theory may be used to predict subsurface fault geometry and slip directions in other transpressive structures without the aid of seismicity.

The similarities in the shape and location of the Scotts Valley and Glenwood synclines in restraining bends along strike-slip faults (fig. 1B) suggest that the theories and models that explained the development of the Glenwood syncline should be applicable to the Scotts Valley syncline and Zayante fault. If the Zayante fault is near-vertical within its restraining bend, as indicated by Clark and Rietman (1973), the fault should intersect the projected east-dipping Scotts Valley syncline at a depth of approximately 15 km (fig. 9). Alternatively, if the Zayante fault dips to the west, similar to the Loma Prieta fault, the fault and fold intersection would occur at a shallower depth. The 80°-cutoff angle between strata and the vertical fault, and the 83.5°-interlimb angle of the syncline suggests only a few-degree change in dip of the fault across the subsurface bend. Notably, this potential fault-bend and fold intersection occurs near to the main-shock hypocenter, which lies on the adjacent Loma Prieta fault (fig. 9). If this predicted subsurface fault geometry is correct, this geometrically complex region with multiple fault and fold intersections may have acted to concentrate stress, localizing the initial main-shock rupture on the Loma Prieta fault. We suggest that further development and application of this technique of modeling subsurface faults and folds holds promise in locating future hypocenters along other strike-slip fault systems.

FAULT SLIP

The transpressive fault-bend fold model for the Loma Prieta epicentral region may also be compared with fault-slip data. Focal-mechanism solutions from the Loma Prieta seismicity yield important constraints on slip within this complex, multiple fault system. The Ms = 7.1 main event was reported to have oblique-reverse, right-lateral slip directed 40° from SE (rake) on a fault plane striking 310° and dipping 70°SW

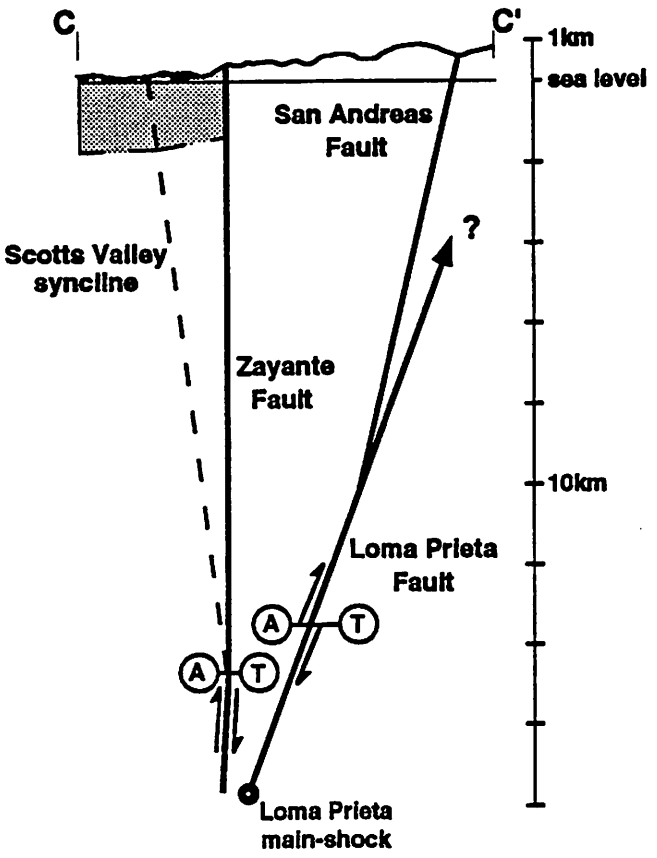

Figure 9: The geologic cross section (C-C') across the Scotts Valley syncline and the Zayante and San Andreas (Loma Prieta) faults (located in figure 1B). The orientation of the synclinal axial surface, (assumed to bisect bedding), predicts a few-degree steepening-upward bend in the underlying Zayante fault at 15 km depth. This potential subsurface fault geometry suggests that the Loma Prieta main-shock may have initiated in a complex region of multiple fault-fold intersections. Lateral motion (A) = away; (T) = toward.

(Oppenheimer, 1990). Focal-mechanism solutions of selected aftershocks, however, suggest that other fault segments with different orientations also slipped. The model of subsurface fault geometry and fold development discussed in the previous section (fig. 7) also provides insight into slip direction on the various fault segments. In order to conserve rock volume during long-term fault slip, both dip-slip and strike-slip components of motion must be resolved between adjacent fault segments represented in figure 7A. Slip directions are also constrained to avoid opening large subsurface voids. In the following sections, we combine fault-slip information provided by the seismicity with reasonable slip directions inferred from our balanced models to describe fault slip along the San Andreas fault system during the Loma Prieta rupture. In order to test the validity of inferred slip directions on different fault segments, we compare them with shear-stress directions resolved onto the fault planes from regional stresses. The regional stresses were described by Michael et al. (1990), derived by an inverse method from seismicity prior to and during the Loma Prieta rupture. In the following section, based on the assumption that these coseismic slip directions approximate long-term slip directions, we calculate long-term slip rates on the San Andreas fault and uplift rates above the Loma Prieta fault segment. The result is then compared with uplift rates calculated by Valensise and Ward (1991) and Anderson (1990) from dated marine terraces from the nearby Santa Cruz coastline. Finally, uplift rates are derived for the Zayante fault, which did not rupture in the Loma Prieta event, by analysis of syntectonic (growth) sediments. Electric logs from wells on opposite sides of the fault record different stratal thicknesses that have resulted from uplift of one side of the fault relative to the other.

Fault-Slip Directions and Regional Stresses

It has long been proposed that the direction of slip is equivalent to the direction of resolved shear-stress on a fault plane (Bott, 1959). Consequently, a straightforward

test of the validity of slip directions inferred from seismicity and fault models in the epicentral zone is to compare them with applied shear-stress directions derived from the regional stress field. Michael et al. (1990) examined earthquakes prior to, as well as during, the Loma Prieta rupture and used an inverse method (Michael, 1987a; 1987b) to estimate the relative magnitudes and directions of the three principal axes of stress. These authors derive tensor components for the southern, deep and shallow central, and northern parts of the Loma Prieta rupture. We test whether our inferred slip directions (determined from fault geometry and models, not first motions) agree with shear-stress directions resolved on the various fault segments by the regional stresses estimated by Michael et al. (1990). This analysis simply confirms that the slip directions derived from our model (fig. 7) are reasonable within the inferred stress field. We have used the FORTRAN program FMSI, provided by John W. Gephart (Gephart, 1990), to resolve shear-stress directions on the fault segments from regional stresses.

In the southern segment of the Loma Prieta rupture along the San Andreas fault (fig. 7A, segment #1), focal-mechanism solutions of selected aftershocks (Oppenheimer, 1990) and strong motions (Beroza, 1991) suggest predominantly right-lateral strike-slip motion. We find that components of the inferred regional stress tensor (fig. 10, σ^1 trends 000°, σ^2 is vertical, $\phi^* = 0.39$, R= 0.61; Michael et al., 1990) resolve into a shear-stress on the San Andreas fault segment (320°-82°W) directed essentially parallel to the inferred horizontal strike-slip vector. The angle between the resolved shear-stress and the fault-slip direction measured in the fault plane, which is an accepted measure of error between slip and a predicted stress state, is in this case less than 1°. Pure right-lateral strike-slip on the San Andreas

---

* where $\phi = (\sigma_2 - \sigma_3)/(\sigma_1 - \sigma_3)$, when σ_1, σ_2, and σ_3 are the three principal stresses from most compressional to most tensional (Angelier, 1979). $R = 1 - \phi = (\sigma_2 - \sigma_1)/(\sigma_3 - \sigma_1)$, (Etchecopar et al. 1981). Note: $\phi^* \neq \phi$ = change in fault dip of the fault-bend fold equations, fig. 4.

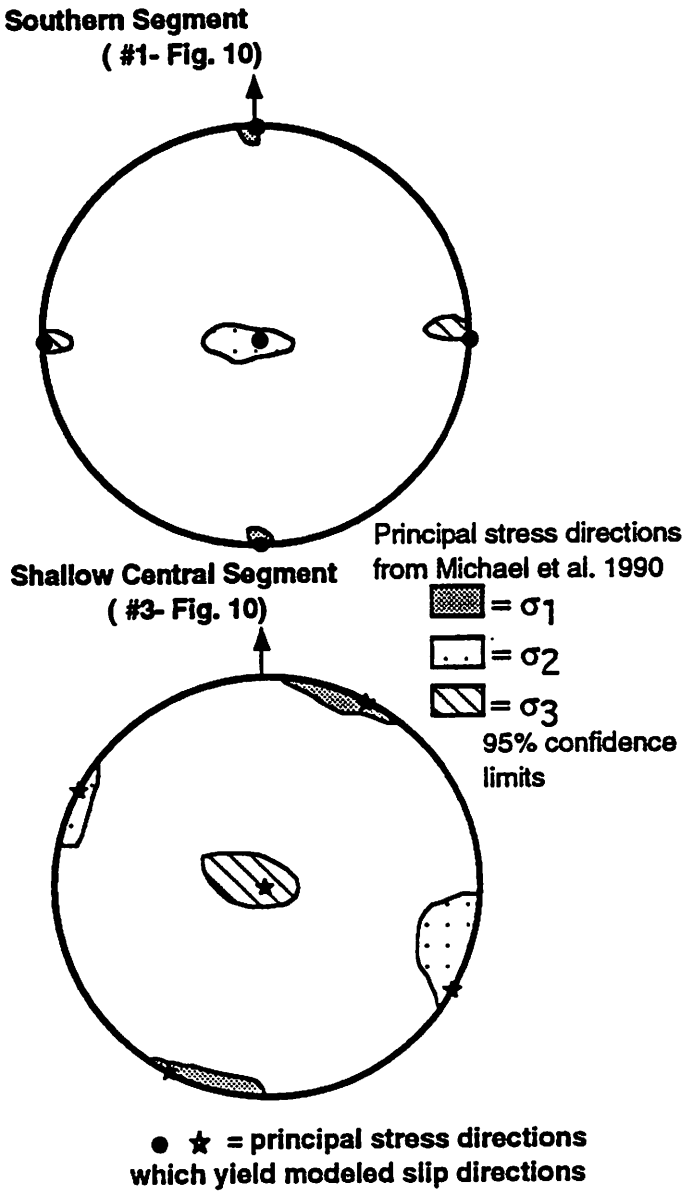

Figure 10: Equal area stereo-nets showing confidence limits of principal stress directions in the epicentral zone derived by Michael et al. (1990). Components of the stress tensors were inverted using seismicity prior to the Loma Prieta earthquake in the southern segment and from aftershocks of the earthquake in the shallow central segment. Principal stress directions are shown which yield shear-stress directions parallel to the slip directions we infer on the various fault segments in figure 7A.

fault southeast of the restraining bend at Loma Prieta, inferred from geologic evidence, is therefore consistent with regional seismicity and the inferred stress field.

Michael et al. (1990) report a stress tensor within the 95% confidence limits of their inversion which yields a 25° discrepancy between the applied shear-stress direction and the slip direction of the main-shock on the Loma Prieta fault (310°-70°W, rake = 40° from SE; Oppenheimer, 1990). They indicate that the 25° value is less than the average variance in the data used in the inversion, and that the main-shock slip direction is therefore not inconsistent with their predicted regional stresses. The main-shock slip direction inferred from the seismicity (Oppenheimer, 1990) is also consistent with the subsurface fault geometry that we derive by analysis of the hypocentral locations (fig. 7A). The slip vector very closely approximates the line of intersection between the Loma Prieta and the southeastern San Andreas faults (fig. 11). In fact, slip on two simultaneously active fault planes must be in the direction of the line of intersection of the two faults in order to avoid subsequent deformation of the fault blocks. Slip in any other direction on the Loma Prieta fault would require additional deformation along the faults in order to close subsurface voids or to alleviate "room" problems. Similarly, we suggest a slip direction on the shallow segment of the San Andreas fault (310° - 78°W; fig. 7A, fault segment #3) above the Loma Prieta fault, parallel to the intersection of this fault and the bounding segment of the San Andreas fault (fig. 7A, fault segment #1). We calculate that another stress tensor (σ^1 = 029°, σ^3 is vertical; ϕ^* = 0.6, R=0.4) within the 95% confidence limits of Michael et al. (1990) applies a shear-stress direction parallel to the inferred slip direction on this shallow fault segment (fig. 10).

These results suggest that slip directions in the Loma Prieta epicentral zone derived from our balanced models and the fault geometry defined by hypocentral locations are generally consistent with the inferred regional stresses. Slip directions on the San Andreas fault southeast and northwest of the restraining bend are parallel

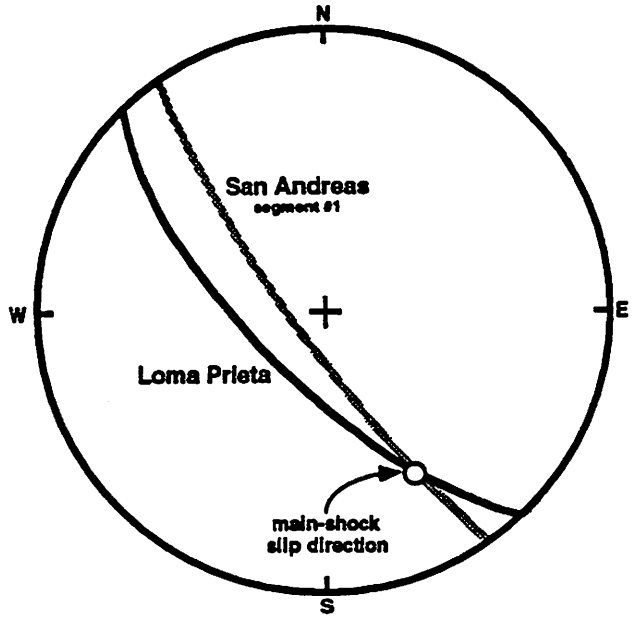

Figure 11: An equal-area stereonet showing the orientation of the Loma Prieta fault and the segment of the San Andreas fault southeast of the restraining bend (segments 2 and 1, fig. 7A). The line of intersection of these two fault planes closely corresponds with the orientation of the main-shock slip direction derived from first-motion studies by Oppenheimer (1990).

to shear-stress directions applied by stress tensors which lie within the confidence limits of inferred regional stresses (fig. 10). Slip during the main-shock on the Loma Prieta fault, though it does not agree as well with the applied shear-stress direction, is not inconsistent with inferred regional stresses (Michael et al., 1990). Moreover, the main-shock slip direction is consistent with the subsurface fault geometry in the epicentral zone (fig. 11). It appears that the line of intersection of the San Andreas and Loma Prieta faults may have placed a geometric boundary condition controlling the direction of slip during the 1989 event. The faults, acting as discontinuities, may have locally modified the regional stress field which resulted in the geometrically favorable slip direction of the main-shock.

The continuous lateral extent and roughly similar dips of the limbs of the Glenwood syncline (fig. 1B) suggest that the subsurface fault geometry in the epicentral zone has not changed significantly throughout the Quaternary. Significant changes in the fault geometry would produce irregularly shaped fold limbs and offsets in the synclinal axial surface. Therefore, we suggest that the geometrically favorable slip directions of the 1989 rupture may provide a reasonable estimate of the long-term slip direction on these fault segments. In the following section we explore this possibility by using these inferred slip directions and estimates of the long-term slip rates on the San Andreas fault to calculate slip and uplift rates in the epicentral zone.

Recurrence Intervals, Long-Term Slip, and Uplift Rates

Long-term motion inferred by geologic and seismic (Hall, 1984) and geodetic (Prescott et al., 1981) data is consistent with the predominantly right-lateral strike-slip motion that was derived from focal-mechanism solutions of aftershocks located on the San Andreas fault in the southeastern part of the Loma Prieta rupture (Oppenheimer, 1990). Geologic and geodetic estimates of the long-term slip rate on the San Andreas fault in this area are reported at 12 mm/year (Hall, 1984) and 12.2

mm/year (Prescott, 1981). Slip on the Loma Prieta fault inferred from first-motion studies however was oblique-reverse, right-lateral motion (Oppenheimer, 1990). Geodetic data suggests that 1.6 ± 0.3 meters of strike-slip and 1.2 ± 0.3 meters of reverse-slip (total slip = 2 ± 0.4 m) took place during the earthquake (Lisowski et al., 1990), resulting in a ratio of strike-slip to dip-slip of 1.3. Similarly, Marshall et al. (1991) report a best-fit model to vertical deformation with 2.1 ± 0.1 meters of total slip. As discussed in the previous section, the slip direction of the Loma Prieta main-shock is parallel to the intersection of the San Andreas and Loma Prieta fault segments (fig. 11). Therefore, as modeled in figure 2, rigid-block translation over these faults would produce parallel slip on the Loma Prieta fault segment (vector ***C***; fig. 12) and on the adjacent segment of the San Andreas fault (vector ***B***). If long-term slip on this small segment of the San Andreas fault were not equivalent to slip on the Loma Prieta fault, then a large amount of as yet unrecognized hanging-wall deformation would have to occur in order to conserve volume during deformation and to collapse large subsurface voids. Similarly, the long-term slip vector on the small segment of the San Andreas fault (vector ***B***) must contain a strike-slip component equivalent to the long-term rates on the San Andreas fault farther to the southeast of the restraining bend (vector ***A***; fig. 12). Using the 12 mm/year value (vector ***A***) and simply solving the slip-vector triangle yields a 15.2 mm/year long-term slip rate on the small segment of the San Andreas (vector ***B***) and adjacent Loma Prieta fault (vector ***C***; fig. 12). This change in the long-term slip vectors from predominantly strike-slip in the southeast to oblique-reverse, right-lateral slip in the northwest is consistent with the slip directions of the Loma Prieta earthquake inferred from strong motions (Beroza, 1991; Steidl et al., 1991) and vertical deformation (Marshall et al., 1991). The 15.2 mm/year long-term slip rate on the Loma Prieta fault (310°- 70°W) resolves to a dip-slip rate of 9.8 mm/year and a strike-slip rate of 11.6 mm/year that corresponds to the estimated 1.3 slip ratio of the Loma Prieta main-shock (Lisowski

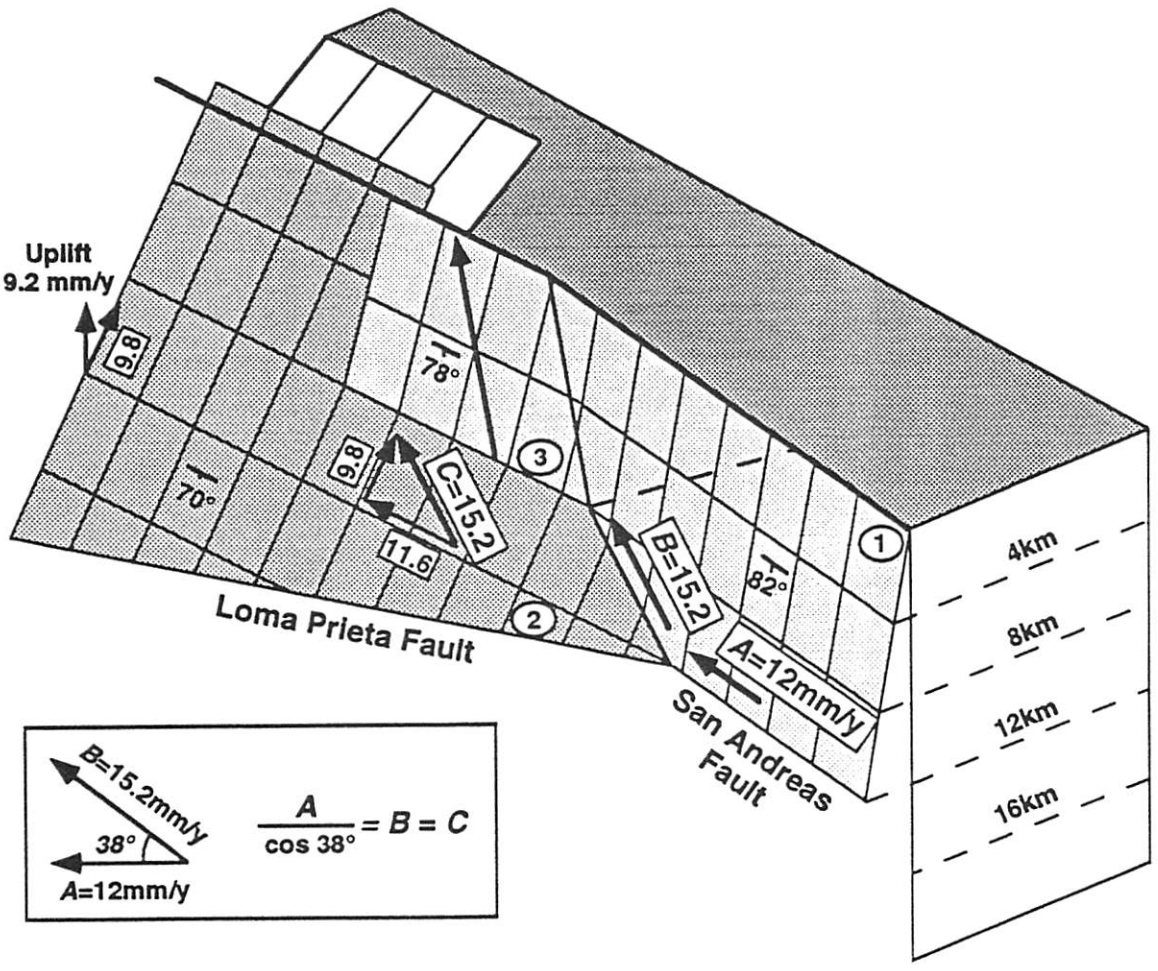

Figure 12: A subsurface fault model of the epicentral zone presented in figure 7A with long-term slip vectors calculated using inferred slip directions and a 12 mm/year (vector A) estimate of the long-term slip on the San Andreas fault southeast of the rupture (Hall, 1984). The slip rates on the Loma Prieta (vector *C*) and adjacent San Andreas (vector *B*) fault segments are equal (both 15.2 mm/year) and in the direction of the 1989 main-shock. The 15.2 mm/year value was calculated assuming that slip on the small segment of the San Andreas fault (vector B) must account for the 12 mm/year of right-lateral strike-slip southeast of the rupture (vector *A*). The 15.2 mm/year slip-rate on the Loma Prieta fault segment (vector *C*) resolves to a 9.8 mm/year dip-slip and 11.6 mm/year strike-slip component, and a 9.2 mm/year uplift-rate above the fault (not corrected for isostatic compensation).

et al., 1990). In addition, this increase in slip rate onto the Loma Prieta fault segment in the restraining bend may explain why the Loma Prieta, and possibly other strike-slip earthquakes, initiate at fault bends.

Resolution of the slip vector triangle which includes the 9.8 mm/year dip-slip rate on the 70° southwest-dipping Loma Prieta fault segment yields an uplift rate above the fault of 9.2 mm/year (fig. 12). However, using dated, uplifted marine terraces along the Santa Cruz coastline, several authors calculate much smaller average uplift rates of .77 mm/year (Valensise and Ward, 1991) and .8 mm/year (Anderson, 1990) adjacent to the fault in the epicentral zone. These authors suggest that repeated 1989 Loma Prieta-like events, which encompass all of the slip from the adjacent San Andreas fault, would produce higher uplift rates than they calculate. They suggest that ruptures similar to the 1989 event alternate with events on the fault that contain larger amounts of strike-slip relative to reverse motion. They contend that this would allow all of the long-term slip on the San Andreas fault to transfer to the Loma Prieta fault, yet produce lower uplift rates consistent with their results. Alternatively, we suggest that slip in the 1989 earthquake parallel to the line of intersection of the two fault segments that form the restraining bend (fig. 11) was not fortuitous. Slip in any other direction on the Loma Prieta fault segment would necessitate additional deformation, which has not yet been recognized, to conserve volume and close subsurface voids caused by slip over this fault segment intersection. Furthermore, as Crowell (1974a, 1974b) recognized, strike-slip motion in this restraining bend necessitates uplift or lateral motion of material away from the fault bend to conserve rock volume. Pure strike-slip motion on the Loma Prieta fault segment cannot cause uplift. Lateral motion of material away from the restraining bend would require additional reverse or thrust faulting in the western block in the vicinity of the fault bend that is not observed (fig. 1B). Strike-slip motion on a near-vertical San Andreas fault that bends and passes below the Loma Prieta fault segment does not avoid

these conservation of volume restrictions. Therefore, we suggest that when motion occurs on the Loma Prieta and San Andreas fault segments, slip likely occurs parallel to the line of intersection between the two faults.

A number of effects may explain the discrepancy between the uplift values calculated by Valensise and Ward (1991) and Anderson (1990) and the higher uplift rates that we calculated assuming repeated 1989-like events. Foremost, the geometrically constrained values that we calculate are uncorrected for isostatic compensation. Presumably, repeated thrusting in Loma Prieta-type events would produce crustal thickening that would lead to downward vertical displacements of the lithosphere in order to achieve stable density distributions within the crust and upper mantle (Bott, 1971; Suppe, 1985). Therefore, uplift rates measured at the surface would be only a fraction of those summed from slip in repeated Loma Prieta events. Using the equations of pointwise isostasy** :

$$\Delta E = \Delta h_c + \Delta h_m + \Delta h_a$$

and

$$\Delta(\rho_c h_c) + \Delta(\rho r_m h_m) + \Delta(\rho_a h_a) = 0$$

and using reasonable average densities from Bott (1971) and Suppe (1985), and assuming no change in the thickness of mantle lithosphere;

$$(3000\text{kg/m}^3)\ (\Delta h_c) + (3300\text{kg/m}^3)\ (\Delta h_a) = 0$$

and

$$\Delta h_c + \Delta h_a = \Delta E$$

** where ΔE is the total change in elevation, h_c is the thickness of the crust, h_m is the thickness of the mantle lithosphere, h_a is the thickness of the mantle asthenosphere, ρ_c is the density of the crust, ρ_m is the density of the mantle lithosphere, and ρ_a is the density of the mantle asthenosphere.

Therefore, for each 9.2 mm/year of uplift and thickening of the crust, only 0.8 mm/year of total elevation change occurs above the fault after isostatic compensation.

$$(3000\text{kg/m}^3)\ (9.2 \times 10^{-3}\text{m}) + (3300\text{kg/m}^3)\ (\Delta h_a) = 0$$

and

$$9.2 \times 10^{-3}\text{m} + \Delta h_a = \Delta E$$

solving for Δh_a and ΔE,

$$\Delta h_a = -8.4 \times 10^{-3}\text{ m (-8.4 mm), and } \Delta E \approx 0.8 \times 10^{-3}\text{m (0.8 mm)}$$

This corrected uplift value (0.8 mm/year) falls within the range of uplift rates (0.77 - 0.8 mm/year) reported by Valensise and Ward (1991) and Anderson (1990), which also account for elasticity and isostatic compensation of the crust. Although we cannot exclude the possibility of other types of slip events in the 1989 epicentral zone, we suggest that uplift rates calculated in these other studies are generally consistent with the values we derive assuming that all long-term slip on the San Andreas is released in repeated earthquakes similar to the 1989 Loma Prieta rupture. It is therefore plausible that the 1989 Loma Prieta earthquake was a typical rupture along this part of the San Andreas fault system, and that long-term slip rates on the San Andreas fault can therefore be used to estimate earthquake-recurrence intervals.

In order to consume slip on the San Andreas fault at a rate of 12 mm/year, oblique-slip must occur on the Loma Prieta fault at an average rate of 15.2 mm/year (fig. 12). Assuming that this slip rate is correct, if all of this slip occurs during earthquakes similar to the 1989 Loma Prieta main-shock, which released 2 ± 0.4 meters of slip (Lisowski et al., 1990), then the earthquakes should recur every 132 ± 26 years. The 1865 Santa Cruz Mountains earthquake may therefore be a viable candidate for the last break on this fault segment (Toppozada et al., 1981). In accordance, McNutt and

Toppozada (1989) report that the 1865 earthquake had an estimated magnitude (M=6.6) and epicentral location similar to the 1989 rupture.

Motion on the ZayanteFault

We have presented evidence that the Glenwood syncline has formed by slip over a subsurface fault bend between the San Andreas and Loma Prieta fault segments. Similarly, we suggest that the deformed Purisima Formation along the Scotts Valley syncline indicates that motion has occurred through the restraining bend along the Zayante fault in the epicentral zone since the early Pliocene. Deformed Pliocene and Quaternary horizons (Hall et al., 1974; Clark et al., 1984) and several fault surface breaks through Quaternary sediments to the south of the bend (fig. 1B) suggest recent activity on the Zayante fault. In order to constrain fault-motion history and to identify active fault segments without the aid of recorded seismicity, we apply the technique of Bischke and Suppe (1990) and Bischke (in review) to analyze growth sediments coevally deposited with fault motion. Thickness changes in growth sedimentary sequences measured in electric logs that straddle the faults record rates of uplift across splays of the Zayante fault. Only the differential dip-slip component of motion between the two wells is recorded. A brief description of the method follows.

The Vertical Displacement Method ($\Delta D/d$) identifies expanded or syntectonic sedimentary sections that record the local tectonic history. An assumption of the method is that the sedimentation rate is greater than or about equal to the uplift rate (Bischke, in review). For example, the method may consider two wells located on opposite sides of a fault (fig. 13). If sedimentary sequences can be correlated between the two wells, then the vertical distance that the sequences have been displaced relative to one another (ΔD) can be determined. A convenient graphical method of determining growth section in the two wells is to plot the relative vertical displacement between the sequence boundaries (ΔD) versus the depth to the same

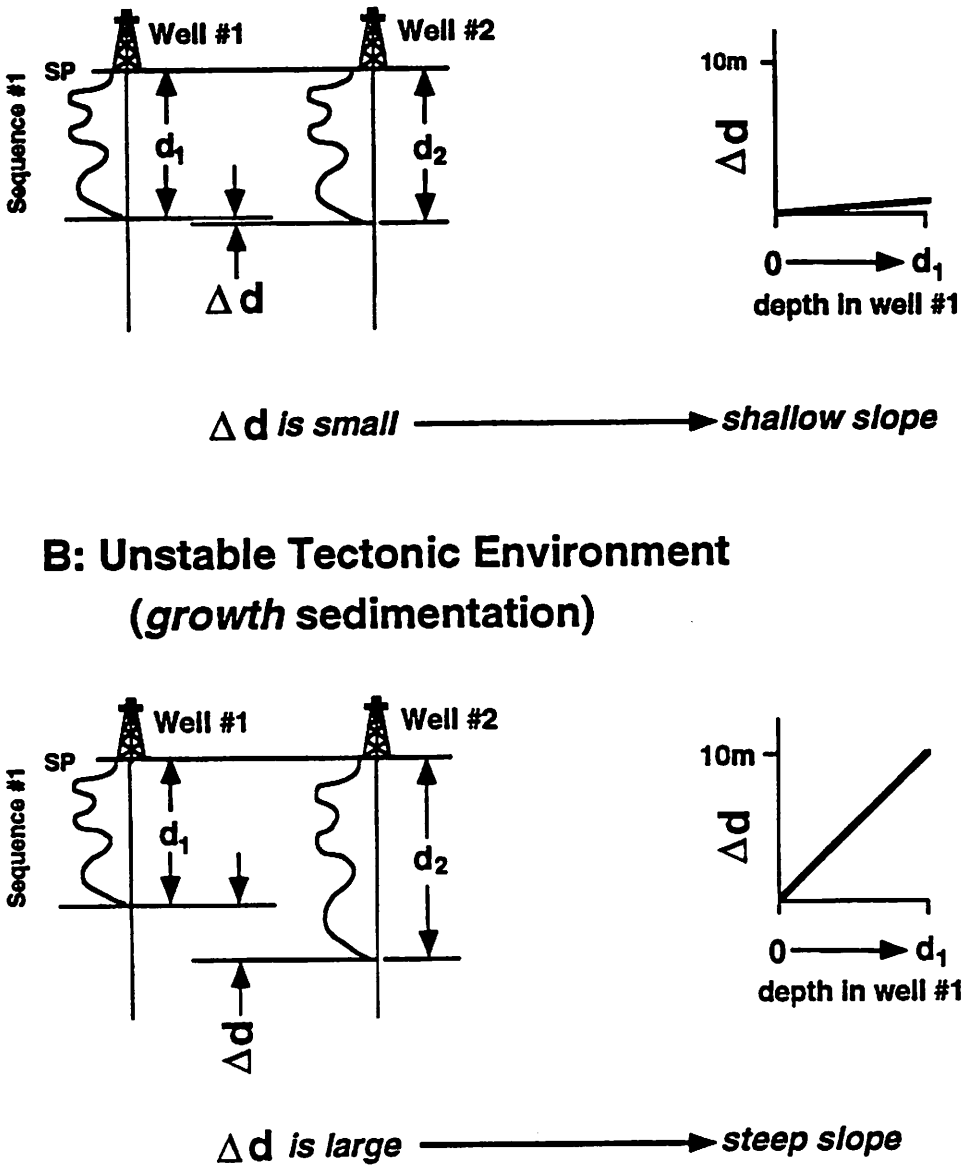

Figure 13: (A) A schematic diagram of a stable tectonic (pre-growth) environment where stratigraphic sequences can be correlated between wells. A plot of the vertical displacement of pre-growth horizons (ΔD) vs. the depth to the correlated horizons in the structurally higher well (d) lies along a shallow-sloping line. Thus a shallow slope establishes a pre-growth section. (B) A (ΔD)/(d) plot of correlated horizons deposited in an unstable tectonic (growth) environment lies along a steeply sloping line. Section expansion, or growth, is attributed to differential tectonic motion between the wells, with thicker sediments accumulating on the down-thrown fault block.

horizons in the structurally higher well (d). In a plot of strata deposited prior to fault motion, data points that correspond to correlated horizons of pre-growth strata lie along a near-horizontal line (fig. 13A). However, in a similar plot of strata deposited coeval with fault motion, growth horizons lie along sloping lines or curves (fig. 13B). The steep slope of the line results from thickness changes in strata on opposite sides of the fault brought on by thicker sediments accumulating on the down-thrown side of the fault. Using this plotting convention, large positive slopes on these diagrams represent expanded growth sections, while large negative slopes represent reduced or condensed sections. This technique, when applied to strata on opposite sides of a fault, therefore provides an easy method of distinguishing between growth and pre-growth strata which identify periods of fault motion and quiescence. An expanded description and rigorous definition of this technique applied to transpressive as well as deltaic, salt dome, compressional, and extensional environments is presented in Bischke (in review).

In wells across splays of the Zayante fault (fig. 1B) we are able to correlate 17 stratal sequences within the Pliocene and Pleistocene section (fig. 14). Motion along splays of the Zayante fault between Pierce, Light, and Blake wells are recorded in growth sedimentary sections. Lacking significant onlap, the well section (fig. 14) indicates that no substantial bathymetry/topography existed across these fault splays during deposition of the Pliocene and Pleistocene sediments. Therefore, the sedimentation rate exceeded the rate of tectonic uplift during this period. A vertical-displacement/depth ($\Delta D/d$) diagram generated from Pierce and Light well-log data, shows that growth, (in the form of an expanded section), initiated in the late Pliocene between the deposition of horizons 5 and 6 (fig. 15). The sloping, linear growth above horizon 5 shows that section expansion has continued into the Quaternary. This expansion rate, continuing into the Holocene, also appears to account for the

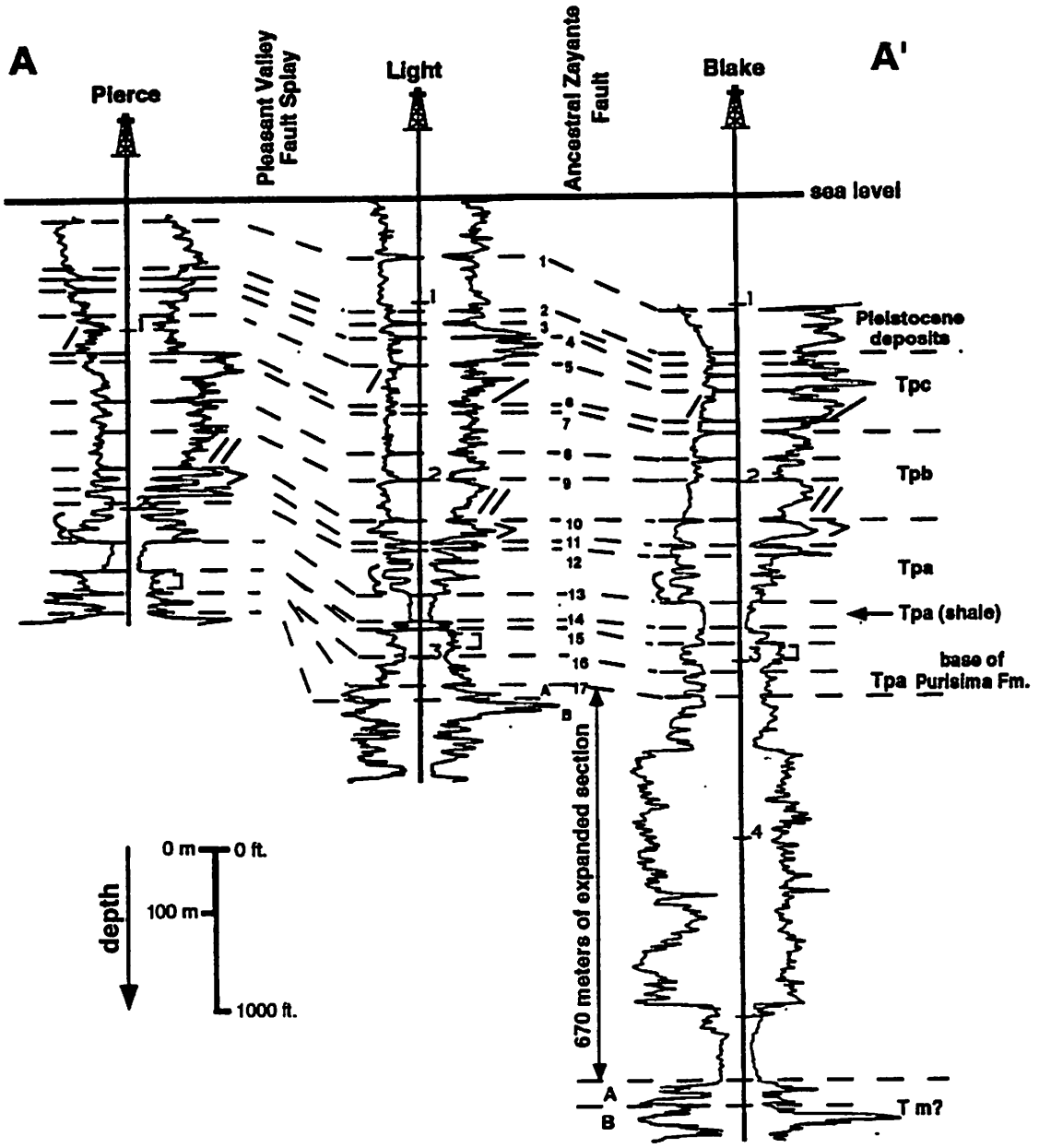

Figure 14: A correlation section (A-A') of electric resistivity and spontaneous potential logs from wells across strands of the Zayante fault (located in figure 1B). Seventeen Pliocene and Pleistocene stratigraphic sequences are correlated between wells, with expanded or growth section defining periods of fault motion. Unit symbols used in this figure: Purisima Formation (upper Miocene and Pliocene)--Tpa, unit a; Tpb, unit b; Tpc, unit c; Monterey(?) Formation (middle Miocene), Tm?

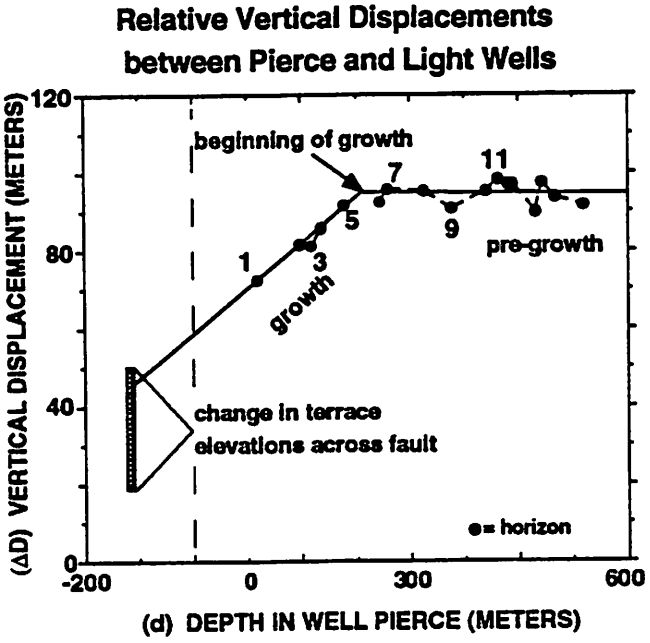

Figure 15: A vertical-displacement (ΔD) vs. depth (d) plot of stratigraphic horizons correlated between wells Pierce and Light across the Pleasant Valley fault splay (fig. 1B). A horizontal least squares best-fit line through the data marks an early period of non-growth, below 300 meters, followed by expanded section (growth) above 300 meters. The Pliocene and Quaternary expanded section is attributed to coeval motion on the splay of the Zayante fault between the wells (fig. 1B). Fault motion continuing into the present may account for the change in terrace elevations across the fault.

present terrace relief across the fault (fig. 15). This suggests that the Pleasant Valley splay of the Zayante fault may still remain active.

A ($\Delta D/d$) plot of horizons recorded in wells Light and Blake (fig. 16) shows a slightly different growth history across the central splay of the Zayante fault (fig. 1B). The negative slope of the growth phase between horizons 1 to 9 indicates a condensed section that is contemporaneous with the expanded section between the Pierce and Light wells (fig. 15). This west to east transition from expanded section across the western Zayante splay to condensed section across the central Zayante splay suggests that a delta may have prograded away from the western uplifted block of the Pleasant Valley fault splay (fig. 17). The condensed section above horizon 9, and the slightly expanded section between horizons 9 and 17 between wells Light and Blake (fig. 16), suggests that motion on the central Zayante fault splay initiated prior to motion on the western splay. The 670-meter (≈ 2200 ft) expanded section below 950 meters in well Blake (figs. 14 and 16) records early (pre-Pliocene) motion on the central splay of the Zayante fault. Motion on this ancestral Zayante fault produced the basin present between the Zayante and San Andreas fault (Clark and Rietman, 1973) (fig. 14).

The surface breaks and expanded and condensed sections across these two splays of the Zayante fault, which merge both to the north and south (fig. 1B), suggest that these faults have moved during the Quaternary. Although there has been no confirmed historic seismicity on the fault, the available evidence is consistent with an active Zayante fault. Therefore, the Zayante fault may pose an earthquake hazard to the adjacent populated regions. Fortunately, if the faults are active, our estimated average uplift rate of the western side relative to the eastern side of the fault splays has been small (≈ 0.07 mm/year) since the beginning of the Pleistocene (≈ 1.8 Ma). This 0.07 mm/year uplift rate falls within the range of preferred uplift rates (0.06 - 0.1 mm/year) along the Zayante fault reported by Clark et al. (1984). However, the

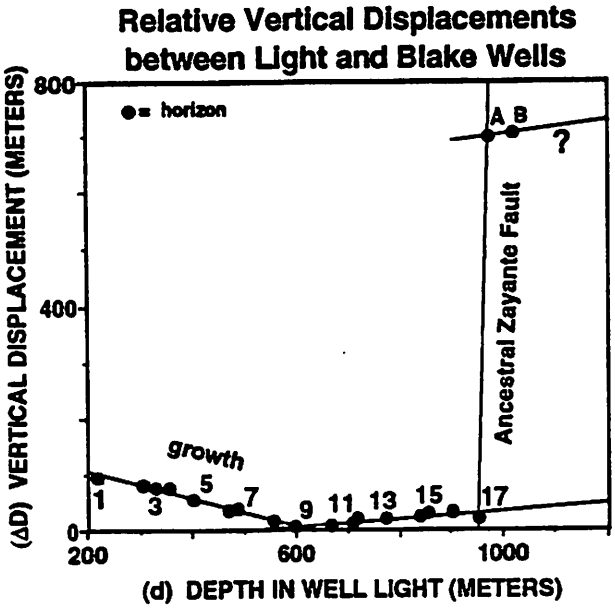

Figure 16: A vertical-displacement (ΔD) vs. depth (d) plot of stratigraphic horizons correlated between wells Light and Blake (fig. 1B). Inclined least-squares best-fit lines through the data mark an early (below 960 meters), and more recent (above 600 meters), periods of growth. The early Miocene growth is attributed to motion on the ancestral Zayante fault.

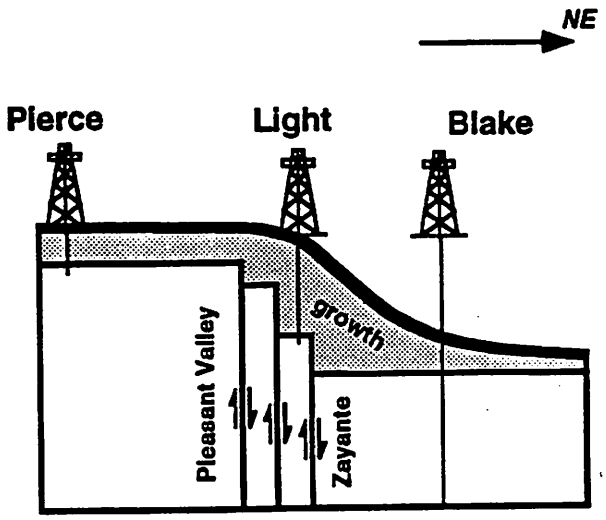

Figure 17: A schematic diagram showing thicker accumulation of deltaic sediments on the down thrown side of the Zayante fault system, (wells are located in fig. 1B).

location of the Scotts Valley syncline in the restraining bend and the orientation of this near-vertical fault (fig. 1B) with respect to the regional stress field (Michael et al, 1990) and the San Andreas fault suggest that the majority of recent fault motion is strike-slip. Further analysis of geologic data, or future seismicity, is required to constrain more precisely the slip rate and earthquake hazard posed by the Zayante fault.

SUMMARY AND CONCLUSIONS

Right-lateral motion along the San Andreas and Zayante faults into left-stepping restraining bends has resulted in thrusting and uplift of the hanging-wall rocks. Thrusting over non-planar fault surfaces within these restraining bends has folded the hanging-wall strata into synclines. Fold growth is represented in geometrically and kinematically reasonable balanced models developed using fault-bend fold theory (Suppe, 1983). Application of these models to the epicentral zone of the 1989 Loma Prieta earthquake yields predictions of the dip and location of subsurface bends in the fault segments. These predictions have been confirmed for the San Andreas and Loma Prieta faults by using hypocenters of the 1989 rupture to determine subsurface fault geometry. The consistent subsurface fault geometry inferred by these two independent methods suggests that fault-bend folding is a viable theory for the origin of folds that lie adjacent to strike-slip faults.

The Loma Prieta seismicity, the surface geology, and the subsurface models indicate that the epicentral zone consists of several active fault segments that comprise the San Andreas fault system. Slip on the various fault segments, inferred from seismicity, geodesy, and the subsurface fault geometry, is found to be consistent with regional stresses assuming that the slip directions on the faults are parallel to the applied shear-stress directions. Furthermore, the subsurface fault geometry of the epicentral zone suggests that long-term slip must increase into this restraining

bend. The 12 mm/year long-term slip rate on the San Andreas fault southeast of the rupture must increase to a 15.2 mm/year slip rate on the Loma Prieta fault segment. This increase in slip rate into the restraining bend may explain why the Loma Prieta, and possibly other strike-slip earthquakes, initiate at fault bends. In addition, long-term uplift rates calculated using our observed fault geometry and reported long-term slip rates on the San Andreas fault in this region, agree with rates derived by Valensise and Ward (1990) and Anderson (1990) from marine terrace elevations along the Santa Cruz coastline once they are corrected for isostatic compensation. Moreover, this suggests that the 1989 Loma Prieta earthquake may have been a typical rupture for this part of the San Andreas fault system. Further, if slip on the San Andreas fault is released in repeated Loma Prieta-like events, this suggests that the earthquakes should recur every 132 ± 26 years. Expanded sedimentary sections deposited across splays of the Zayante fault suggest that this fault is presently active. Consequently, faults in the Santa Cruz Mountains continue to pose a significant earthquake hazard to adjacent populated regions.

Acknowledgments

This research was funded by National Earthquake Hazards Reduction Program (NEHRP) Grant #14-08-0001-G1827, Princeton University, and Texaco U.S.A. The authors thank Chris Connors, Paul Genovese, Stephen Hook, Craig Nicholson, David Pollard, and Leonardo Seeber for helpful discussions and comments during this research. Thanks also to Daniel Tearpock for reviewing well-log correlations and to John Gephart for providing his FORTRAN program FMSI, which we used to resolve shear-stress directions on the fault segments from regional stresses. In addition, we are grateful for beneficial reviews by Joseph Clark, Oona Scotti, and Robert Simpson.

REFERENCES

Anderson, R. S., 1990, Evolution of the Santa Cruz Mountains by advection of crust past a San Andreas fault bend: Science, v. 249, p. 397-401.

Angelier, J., 1979, Determination of the mean principal directions of stresses for a given fault population: Tectonophysics, v. 56, T17 - T26.

Beroza, G. C., 1991, Near-source modeling of the Loma Prieta earthquake: Evidence for heterogeneous slip and implications for earthquake hazard: Bulletin of the Seismological Society of America, v. 81, no. 5, p. 1603-1621.

Bischke R., E., in review, Interpreting growth structure from well-log and seismic data: American Association of Petroleum Geologists Bulletin.

Bischke, R. E. and Suppe, J., 1990, Calculations of uplift rates on the Zayante fault utilizing well-log correlations: EOS, v. 71, p. 555.

Bott, M. P. H.., 1959, The mechanics of oblique slip faulting: Geology Magazine, v. 96, p. 109 - 117.

----------, 1971, *The interior of the earth*: Edward Arnold Publishers Ltd., London, England, 315 p.

Brabb, E. E., 1989, Geologic map of Santa Cruz County, California: USGS Miscellaneous Investigations Series, Map I-1905, scale 1:62500.

Clark, J. C., 1981, Stratigraphy, paleontology, and geology of the central Santa Cruz Mountains, California Coast Ranges: USGS Professional Paper 1168, p. 1 - 51.

Clark, J. C., and Rietman, J. D., 1973, Oligocene stratigraphy, tectonics, and paleogeography southwest of the San Andreas Fault, Santa Cruz Mountains and Gabilan Range, California Coast Ranges: USGS Professional Paper 783, p. 1 - 18.

Clark, M. M., Harms, K. K., Lienkaemper, J. J., Harwood, D. S., Lajoie, K.R., Matti, J. C., Perkins, J. A., Rymer, M. J., Sarna-Wojcicki, A.M., Sharp, R. V., Sims, J. D., Tinsely, J. C., III, and Ziony, J. I., 1984, Preliminary slip-rate table and map of late-Quaternary faults of California: USGS Open-File Report 84-106, 12 p., 5 plates.

Crowell, J. C., 1974a, Origin of late Cenozoic basins in southern California; in *Tectonics and Sedimentation*: Society of Economic Paleontologists and Mineralogists, Special Publication no. 22, p. 190-204.

----------, 1974b, Sedimentation along the San Andreas Fault; in Modern and Ancient Geosynclinal Sedimentation: Society of Economic Paleontologists and Mineralogists, Special Publication no. 19, p. 292-303.

Dietz, L. D., and Ellsworth, W. L., 1990, The October 17, 1989, Loma Prieta, California, earthquake and its aftershocks: Geometry of the sequence from high-resolution locations: Geophysical Research Letters, v. 17, no. 9, p. 1417 - 1420.

Etchecopar, A., Vasseur, G., and Daignieres, M., 1981, An inverse problem in microtectonics for the determination of stress tensors from fault striation analysis: Journal of Structural Geology, v. 3, p. 51 - 65.

Gephart, J. W., 1990, FMSI: A FORTRAN program for inverting fault/slickenside and earthquake focal mechanism data to obtain the regional stress tensor: Computers and Geosciences, v. 16, no. 7, p. 953-989.

Hall, N. T., 1984, Holocene history of the San Andreas fault between Crystal Springs Reservoir and San Andreas Dam, San Mateo Co., California: Bulletin of the Seismological Society of America, v. 79, p. 281 - 299.

Hall, N. T., Sarna-Wojcicki, A.M., and Dupre, W. R., 1974, Faults and their potential hazards in Santa Cruz County, California: USGS Misc. Field Study Map MF-626, 3 sheets, scale 1:62,500.

Lisowski, M., Prescott, W. H., Savage, J. C., and Johnston, M. J., 1990, Geodetic estimate of coseismic slip during the 1989 Loma Prieta, California, earthquake: Geophysical Research Letters, v. 17, no. 9, p. 1437 - 1440.

Marshall, G. A., Stein, R. S., and Thatcher, W., 1991, Faulting geometry and slip from co-seismic elevation changes: The 18 October 1989, Loma Prieta, California, earthquake: Bulletin of the Seismological Society of America, v. 81, no. 5, p. 1660-1693.

McLaughlin, R. J., Clark, J. C., and Brabb, E. E., 1988, Geologic map and structure sections of the Loma Prieta 7.5' quadrangle, Santa Clara and Santa Cruz counties, California: USGS Open-file Report 88-0752.

McNutt, S. R., and Toppozada, T. R., 1990, Seismological Aspects of the 17 October 1989 Earthquake: California Department of Conservation, Division of Mines and Geology, 27 p.

Michael, A. J., Ellsworth, W. L., and Oppenheimer, D. H., 1990, Coseismic stress changes induced by the Loma Prieta, California earthquake: Geophysical Research Letters, v. 17, no. 9, p. 1441 - 1444.

Michael, A. J., 1987a, The use of focal mechanisms to determine stress: A control study: Journal of Geophysical Research, 92, p. 357 - 368.

----------, 1987b, Stress rotation during the Coalinga aftershock sequence: Journal of Geophysical Research, v. 92, p. 7963 - 7979.

Muir, K. S., 1972, Geology and ground water of the Pajaro Valley area, Santa Cruz and Monterey Counties, California: USGS Open-File Report 73-999, p. 1-33.

Oppenheimer, D. H., 1990, Aftershock slip behavior of the 1989 Loma Prieta earthquake: Geophysical Research Letters, v. 17, no. 8, p. 1199 - 1202.

Prescott, W. H., Lisowski, M., and Savage, J. C, 1981, Geodetic measurement of crustal deformation on the San Andreas, Hayward, and Calaveras faults near San Francisco, California: Journal of Geophysical Research, v. 86, p. 10853 - 10869.

Rich, J. L., 1934, Mechanics of low-angle overthrust faulting as illustrated by Cumberland Thrust Block, Virginia, Kentucky and Tennessee: American Association of Petroleum Geologists Bulletin, v. 18, p. 1584-1596.

Schwartz, S. Y., Orange, D. L., and Anderson, R. S., 1990, Complex fault interactions in a restraining bend on the San Andreas fault, southern Santa Cruz Mountains, California: Geophysical Research Letters, v. 17, no. 8, p. 1207 - 1210.

Seeber, L., and Armbruster, J. G., 1990, Fault kinematics in the 1989 Loma Prieta rupture area during 20 years before that event: Geophysical Research Letters, v. 17, no. 9, p. 1425 - 1428.

Steidl, J. H., Archuleta, R. J., and Hartzell, S. H., 1991, Rupture history of the 1989 Loma Prieta, California, earthquake: Bulletin of the Seismological Society of America, v. 81, no. 5, p. 1573-1602.

Suppe, J., 1983, Geometry and kinematics of fault-bend folding: American Journal of Science, v. 283, p. 684-721.

--------, 1985, *Principals of Structural Geology*: Prentice-Hall, Englewood Cliffs, NJ, 537 p.

Suppe, J., Chou, G. T. and Hook, S. C., 1992. Rates of folding and faulting determined from growth strata, in *Thrust Tectonics*, K.R. McKlay ed., Chapman Hall publisher, p. 105-121.

Tearpock, D. and Bischke, R. E., 1991, *Applied Subsurface Geological Mapping*: Prentice-Hall, NJ, 648 p.

Toppozada, T. R., Real, C. R.., and Parke, D. L., 1981, Preparation of isoseismal maps and summaries of reported effects for pre-1900 California earthquakes: California Division of Mines and Geology Open-file Report 81-11 SAC, 182 p.

Valensise, G., and Ward, S. N., 1991, Long-term uplift of the Santa Cruz Coastline in response to repeated earthquakes along the San Andreas fault: Bulletin of the Seismological Society of America, v. 81, no. 5, p. 1694-1704.